Czech Technical University in Prague

Faculty of Nuclear Sciences and Physical Engineering

Department of Solid State Engineering

Master's Thesis

Application of quantum simulations for characterizing the stability of organic extraction ligands

Author: Bc. Jakub Luštinec

Supervisor: doc. Ing. Ladislav Kalvoda, CSc.

Academic year: 2019/2020

ČESKÉ VYSOKÉ UČENÍ TECHNICKÉ V PRAZE
FAKULTA JADERNÁ A FYZIKÁLNĚ INŽENÝRSKÁ
Katedra inženýrství pevných látek

ZADÁNÍ DIPLOMOVÉ PRÁCE

Student:	**Bc. Jakub Luštinec**
Studijní program:	**Aplikace přírodních věd**
Obor:	**Inženýrství pevných látek**
Akademický rok:	**2019/2020**
Název práce: (česky)	**Využití kvantových simulací pro charakterizaci stability organických exktrakčních ligandů**
Název práce: (anglicky)	**Application of quantum simulations for characterizing stability of organic extraction ligands**

Pokyny pro vypracování:

Diplomová práce je zaměřena na charakterizaci stability a reaktivity organických ligandů vyvíjených pro použití v postupech hydrometalurgického přepracování vyhořelého jaderného paliva pomocí kvantově-mechanických DFT simulací zaměřených na optimalizaci geometrie a elektronové struktury ligandů a dále analýzu jejich možných reakčních mechanismů a rozpadové kinetiky v prostředí extrakčních roztoků. Simulace budou realizovány v Laboratoři materiálového modelování Katedry inženýrství pevných látek FJFI ČVUT v Praze s pomocí zde dostupných SW nástrojů (především Gaussian a Materials Studio).

Při řešení postupujte podle následujících bodů.

I. Rešeršní/teoretická část
   1) Přehled teoretických základů metody DFT vztahujících se ke studované problematice
   2) Popis teorie přechodových stavů a jejího využití při zkoumání reakční kinetiky
   3) Výběr a popis metodického postupu realizace výpočtů a vlivu jednotlivých parametrů

II. Experimentální část
   1) Simulace základního kvantového stavu molekul typu DGA a deskriptorů jejich chemické stability
   2) Simulace navržených reakčních cest ligandů typu DGA
   3) Optimalizace navržených komplexů ligandu a molekul representujících kyselinu a porovnání se simulacemi v nekyselém prostředí
   4) Analýza dosažených výsledků s ohledem na volbu parametrů použitých modelů
   5) Diskuze výsledků ve vztahu k publikovaným experimentálním datům.

Doporučená literatura:

[1] P.I. Matveev, A.A. Mitrofanov, V.G. Petrov, S.S. Zhokhov, a.A. Smirnova, Yu.A. Ustynyuk, S.N. Kalmykov: RSC Adv. **7** (2017) 55441-55449.

[2] M.B. Singh, S.R. Patil, A.A. Lohi, V.G. Gaikar: Sep. Sci. Technol. **53** (2018) 1361-1371.

[3] W. Koch, M.C. Holthausen: A Chemist's Guide to Density Functional Theory, Wiley-VCH, Weinheim 2001.

[4] J.B. Foresman, A.E. Frisch: Exploring Chemistry with Electronic Structure Methods, Gaussian Inc., Pittsburgh 1996.

[5] T. Koubský, J. Fojtíková, L. Kalvoda: Prog. Nucl. Energy **94** (2017) 208-215.

[6] H. Galán, C.A. Zarzana, A. Wilden, A. Núñez, H. Schmidt, R.J.M. Egbering, A. Leoncini, A. Cobos, W. Verboom, G. Modolo, G.S. Groenewold, B.J. Mincher: Dalton Trans. **44** (2015) 18049-18056.

[7] H. Galán, A. Núñez, A. Espartero, R. Sedano, A. Durana, J. de Mendoza: Proc. Chem. **7** (2012) 195-201.

Jméno a pracoviště vedoucího práce:

doc. Ing. Ladislav Kalvoda, CSc., Katedra inženýrství pevných látek, Fakulta jaderná a fyzikálně inženýrská, ČVUT v Praze.

Jméno a pracoviště konzultanta:

Ing. Tomáš Koubský, Ph.D., Katedra inženýrství pevných látek, Fakulta jaderná a fyzikálně inženýrská, ČVUT v Praze.

Datum zadání diplomové práce: 21. 10. 2019

Termín odevzdání diplomové práce: 4. 5. 2020

Doba platnosti zadání je dva roky od data zadání.

.....
garant

.....
vedoucí katedry

.....
děkan

V Praze dne 21. 10. 2019

Declaration

I hereby declare that I completed this work on my own and I used only the sources cited in the reference list.

Prohlášení

Prohlašuji, že jsem svoji diplomovou práci vypracoval samostatně a použil jsem pouze podklady uvedené v přiloženém seznamu.

V Praze 2. 5. 2020

.....
Bc. Jakub Luštinec

Acknowledgement

I would like to thank doc. Ing. Ladislav Kalvoda, CSc for leading my thesis, helpful advice and comments. I would also like to extend my deepest gratitude to Ing. Tomáš Koubský, Ph.D. and Ing. Martin Krupička, Ph.D. for expert consultations.

This work was supported by the GENIORS Project (H2020 Euratom Research and Innovation Programme, No.755171); and the Grant Agency of the Czech Technical University in Prague, grant No. SGS19/190/OHK4/3T/14.

Bc. Jakub Luštinec

Title: **Application of quantum simulations for characterizing the stability of organic extraction ligands**

Author: Bc. Jakub Luštinec

Field of study: Solid State Engineering

Type of thesis: Master's Thesis

Supervisor: doc. Ing. Ladislav Kalvoda, CSc., FJFI ČVUT v Praze

Consultant: Ing. Tomáš Koubský, Ph.D., FJFI ČVUT v Praze

Abstract: Diglycolamides (DGA) is one of the most promising group of extractants used for reprocessing of the radioactive waste. During the reprocessing, the extractants are exposed to harsh conditions that cause their degradation. That results in the decrease of the efficiency of the reprocessing. This work follows up on the previously published bachelor thesis and the theoretical study of the selected representatives of the DGA family. These representatives are tetramethyl DGA (TMDGA), tetraethyl DGA (TEDGA), methyl–TEDGA (Me–TEDGA), and dimethyl–TEDGA (Me_2–TEDGA). Their potential application is, for example, in the EXAm process that is focused on the extraction of americium. This theoretical study is based on the quantum mechanical Density functional theory and Coupled cluster theory. Contents of the work is particularly focused on the analysis of the acid influence on the degradation processes; three different ways of representation of the acid are proposed. Also, one of the possible specific degradation reaction mechanism is proposed and investigated. Orca, CREST utility from xTB, Gaussian09 and $DMol^3$ codes are used. The results of the calculations are compared with the published experimental data, the similar study of TODGA and its derivatives and the previous study without the acid representation. The stability trend (TMDGA $<$ TEDGA $<$ Me–TEDGA $<$ Me_2–TEDGA) described in previous works is supported, mainly by the radical Fukui function, where the trend remains unchanged also with the acid involves. The acid influence is most pronounced for the Fukui charges, where the Fukui charges values decrease for all acid models in comparison to results of previous works.

Key words: DFT, diglycolamide, radiolytic stability, Fukui function

Název práce: **Využití kvantových simulací pro charakterizaci stability organických extrakčních ligandů**

Autor: Bc. Jakub Luštinec

Obor: Inženýrství pevných látek

Druh práce: Diplomová práce

Vedoucí práce: doc. Ing. Ladislav Kalvoda, CSc., FJFI ČVUT v Praze

Konzultant: Ing. Tomáš Koubský, Ph.D., FJFI ČVUT v Praze

Abstrakt:

Diglykolamidy (DGA) jsou extrakční molekuly, které mají vysoký potenciál využití pro přepracování aktivního odpadu pomocí separačních procesů. Během těchto procesů jsou vystaveny tvrdým podmínkám, které způsobují jejich rozpad. Následně dochází ke snížení efektivity celého procesu přepracování. Tato diplomová práce navazuje na mou bakalářskou práci a výzkumný úkol, které se zabývaly teoretickou studií stability vybraných zástupců DGA skupiny molekul. Těmi jsou TMDGA, TEDGA, Me–TEDGA, a Me_2–TEDGA. Jejich potenciální aplikace je v procesu zaměřeném na separaci americia – EXAm proces. Teoretické simulace jsou založeny na využití Density functional theory a Cloupled cluster theory. Práce se jednak zabývá zahrnutím vlivu kyseliny na stabilitu ligandů, dále je navržen a studován jeden možný reakční mechanismus. Použit je Orca, CREST utility z xTB, Gaussian09 a $DMol^3$ software. Výsledky jsou porovnány s experimentálně pozorovanou stabilitou, výsledky z Bakalářské práce a z podobné studie molekuly TODGA a jejich derivátů. Výsledky jsou ve shodě se stejným trendem stability jako v Bakalářské práci (TMDGA < TEDGA < Me–TEDGA < Me_2–TEDGA). Především Radikálová Fukuiho funkce je v souladu s dřívějšími výsledky, kde trend zůstal neměnný po zahrnutí vlivu kyseliny. Její vliv se projevil především u Fukuiho nábojů, kde došlo k jejich celkovému poklesu ve srovnání s dřívějšími výsledky.

Klíčová slova: DFT, diglykolamidy, radiolytická stabilita, Fukuiho funkce

Contents

Introduction

Nuclear power plants have produced a large amount of active waste, i.e. spent nuclear fuel, during decades of their operation. This active waste contains numerous elements, including lanthanides and actinides. The main problem is that minor actinides and Pu are the major contributors to the long lifetime and radiotoxicity of the nuclear waste. One of the possible options of the nuclear waste management is partitioning and transmutation [1].

The partitioning is in many cases done by the solvent extraction processes. The principle of such process is that an organic solvent containing an extracting ligand is in contact with the aqueous solution of the spent nuclear fuel, usually dissolved in nitric acid. The organic extractant is chosen or designed to have the chemical ability to selectively partition the desired elements from the aqueous phase into the organic solvent. An extractant should be efficient, selective, hydrolytically and radiolytically stable, soluble, give fast reaction kinetics and be easily synthesised [1].

The diglycolamide (DGA) family of ligands is one of the considered groups of prospective organic extractants for the separation processes. The DGAs are especially suitable for the extraction of trivalent actinide and lanthanide ions from the active waste, for example Americium, Europium and Curium. The most commonly used DGA ligand is *N,N,N',N'-tetraoctyl-diglycolamide* (TODGA) [2]. The members of the DGA family differ from each other in the speed and efficiency of the separation of elements. Different molecules can be applied during the process to separate the different fractions [1].

Unfortunately, organic extractants are exposed to extreme conditions in the nuclear fuel solution. The solution is acidic due to the application of a strong acid. In addition, the active waste contains unstable isotopes of elements. These isotopes undergo a radioactive decay and emit ionizing radiation. This leads to the degradation of extractant molecules.

The stability study of these molecules is essential for the development of any separation process. This work is based on the widely used concept that the radiolysis is done predominantly indirectly. This assumption is based on the fact, that the concentrations of the extractants in the solution is low. The majority of the ionizing radiation is considered to be absorbed by the solvent (water). The reaction of the solvent and the radiation produces further species, such as free radicals. The radical is a neutral particle that has an unpaired valence electron. This implies that the radical is very reactive and can cause the chemical breakdown of surrounding molecules. The radiolytic stability of the extractants themselves is then considered mainly as a result of chemical interaction of such radical species with the extrac-

tants. The stability study also consists in an investigation of the stability against acidic degradation. This degradation is caused by the acidic environment that acts on the extractants. This stability is referred to as the hydrolytic stability, but the origin of the hydrolytic stability itself is not investigated in this work.

The aim of this work is to theoretically explain the trends that were observed in the experiments with the studied ligands [3, 4]. The theoretical part summarizes the *Density functional theory*, which provides a theoretical background for the used simulations. Also, the basics of the *Coupled cluster theory* are included. In addition, physico–chemical properties of molecules that describe their stability are summarized. In this diploma thesis, the acid influence is also investigated. For this reason, three possible acid models are proposed. Furthermore, the reaction degradation mechanism is proposed and investigated.

This work is mainly focused on the study of the radiolytic stability of the following extractants:

- TMDGA (N,N,N',N'-tetramethyl-diglycolamide; 2,2'-oxybis(N,N-dimethylacetamide))
- TEDGA (N,N,N',N'-tetraethyl-diglycolamide; 2,2'-oxybis(N,N-diethylacetamide))
- Me–TEDGA (2-(2-(diethylamino)-2-oxoethoxy)-N,N-diethylpropanamide)
- Me_2–TEDGA (2,2'-oxybis(N,N-diethylpropanamide)).

The calculations are performed using the following software: $DMol^3$ module of Materials Studio 8.0, Gaussian09 code, CREST utility from xTB code and Orca 4.0.1.2 Release. The results of simulations for the studied molecules are compared with their experimentally observed stability trend that can be written as TMDGA $<$ TEDGA $<$ Me–TEDGA $<$ Me_2–TEDGA [3, 4]. Furthermore, the results are compared with the results of previous study where the acid influence was neglected [5, 6]. Also, the acid representations are compared to each other to investigate the impact of the specific acid model. The results are further compared to similar study for TODGA and its methylated derivatives [7].

Chapter 1

Theoretical part

This chapter is focused on the basic quantum description of the condensed matter and the Density functional theory, which is one of the possible approximations providing theoretical background for sufficiently accurate simulations of the basic properties of organic ligands. Further, basics of the Coupled cluster theory are included. In addition to describing the physical–chemical attributes of molecules, these simulations also allow to study the mechanisms of chemical processes of the system. Furthermore, properties of a molecule describing its reactivity and stability and several methods of their calculation are discussed.

1.1 General description of condensed matter

The study of the electronic structure requires the use of the quantum theory. The investigated system, here the organic molecule, is a set of electrons and nuclei that the system is composed of. This system of particles can be described by the Hamiltonian (1.1) [8, 9], which expresses their mutual interaction. The general form of this Hamiltonian can be written as follows

$$\hat{H} = -\frac{\hbar^2}{2m_e}\sum_i \nabla_i^2 - \sum_I \frac{\hbar^2}{2M_I}\nabla_I^2 + \hat{V}(\mathbf{r}, \mathbf{R}), \tag{1.1}$$

where m_e is the electron mass, $\mathbf{r}$ is a set of all electron positional vectors, i.e., $\mathbf{r} = \{\mathbf{r}_i\}$, $\hbar$ is the reduced Planck constant, M_I is mass of the I–th nucleus and $\mathbf{R}$ is a set of position vectors of all nuclei, i.e., $\mathbf{R} = \{\mathbf{R}_I\}$. The first and the second term expresses respectively the kinetic energy of electrons and nuclei. The third term is the potential operator describing mutual interactions of particles [8]

$$\hat{V} = \frac{1}{2}\sum_{i\neq j}\frac{e^2}{4\pi\epsilon_0|\mathbf{r}_i - \mathbf{r}_j|} + \sum_{i,I}\frac{Z_I e^2}{4\pi\epsilon_0|\mathbf{r}_i - \mathbf{R}_I|} + \sum_{I\neq J}\frac{Z_I Z_J e^2}{4\pi\epsilon_0|\mathbf{R}_I - \mathbf{R}_J|}, \tag{1.2}$$

where $\mathbf{r}_i$ is the position of the i–th electron, e is the elementary charge, ϵ_0 is the vacuum permittivity, $\mathbf{R}_I$ is the position of the I-th nucleus and Z_I is its charge.

The individual terms in equation 1.2 correspond to Coulomb's interactions between particles, i.e., the first term expresses the interaction among electrons, the second one between electrons and nuclei and the third one among the nuclei.

The quantum theory implies that the wavefunction $\Psi(\mathbf{r}, \mathbf{R}, t)$, which is the solution to the Schrödinger equation with Hamiltonian (1.1), completely describes this system. However, this Hamiltonian (1.1) does not depend explicitly on time, so for determination of the wavefunction it is enough to solve the time–independent Schrödinger equation (1.3) [10]. The eigenstates of the time–dependent Schrödinger equation can be written as $\Psi(\mathbf{r}, \mathbf{R}; t) = \Psi(\mathbf{r}, \mathbf{R})\mathrm{e}^{-i\frac{E}{\hbar}t}$ [8, 10, 11]

$$\hat{H}\Psi(\mathbf{r}, \mathbf{R}) = E\Psi(\mathbf{r}, \mathbf{R}). \tag{1.3}$$

The electron density $n(\mathbf{r})$ is an essential property of the electronic structure and the determination of the electron density $n(\mathbf{r})$ is the basic idea in the Density functional theory. The electron density $n(\mathbf{r})$ is the square of the norm of the wavefunction, i.e., the probability of an electron occurrence at the point $\mathbf{r}$ multiplied by the elementary charge. This can be also written by the density operator $\hat{n}(\mathbf{r})$ [8]

$$n(\mathbf{r}) = \frac{\langle\Psi|\hat{n}(\mathbf{r})|\Psi\rangle}{\langle\Psi|\Psi\rangle} = N\frac{\int|\Psi(\mathbf{r}_1, \mathbf{r}_2, \ldots, \mathbf{r}_N)|^2\mathrm{d}^3\mathbf{r}_2 \cdots \mathrm{d}^3\mathbf{r}_N}{\int|\Psi(\mathbf{r}_1, \mathbf{r}_2, \ldots, \mathbf{r}_N)|^2\mathrm{d}^3\mathbf{r}_1 \cdots \mathrm{d}^3\mathbf{r}_N}, \tag{1.4}$$

where the definition of the density operator is

$$\hat{n}(\mathbf{r}) = \sum_{i=1}^{N}\delta(\mathbf{r} - \mathbf{r_i}). \tag{1.5}$$

In addition, it applies

$$N = \int n(\mathbf{r})\mathrm{d}\mathbf{r}, \tag{1.6}$$

i.e., the result of integrating the electron density across the entire space is the number of electrons of the system.

Unfortunately, such determination of the many–body wavefunction is generally insoluble, especially for large systems, and a simplification is required.

1.1.1 The Born–Oppenheimer approximation

One of the basic approximations is the Born-Oppenheimer approximation that is also referred as the adiabatic approximation. This simplification is based on the assumption that the masses of nuclei are much greater than the masses of electrons. This means that the electrons can adjust almost instantaneously to any changes in the positions of the nuclei. The electronic wavefunction thus depends only on the positions of the nuclei and not on their momenta. After several steps, it is then possible to show that the nuclear and electronic wavefunctions are separable [10, 12, 13]. The solution is assumed in form

$$\psi(\mathbf{r}, \mathbf{R}) = \psi_N(\mathbf{R}) \cdot \psi_e(\mathbf{r}; \mathbf{R}). \tag{1.7}$$

Where for the wavefunction of electrons $\psi_e(\mathbf{r};\mathbf{R})$, $\mathbf{R}$ is a parameter [8], and $\psi_N(\mathbf{R})$ is the wavefunction of nuclei. First, the motion of electrons in the field of stationary nuclei is solved and then the motion of the nuclei in the field generated by electrons is determined.

For our needs of investigating the electronic structure, it is sufficient to study the movement of electrons in the field of stationary nuclei. Then the Hamiltonian of the system has the simplified form [8]

$$\hat{H} = \hat{T} + \hat{V}_{\text{int}} + \hat{V}_{\text{ext}} + E_{\text{II}}, \tag{1.8}$$

where $\hat{T}$ is the kinetic energy operator of electrons, $\hat{V}_{\text{int}}$ expresses their mutual interaction, $\hat{V}_{\text{ext}}$ is the potential of nuclei acting on electrons and E_{II} is the interaction among nuclei.

Although this simplification is sufficient for some areas of condensed matter research, it is not sufficient for studying the electronic structure. However, the Born-Oppenheimer approximation is the first step that separates the problem of the electrons and the nuclei. Subsequently, more sophisticated approximation are used to solve the electronic structure [10].

1.2 Density functional theory

Density functional theory (DFT) is an approach to the electronic structure of atoms and molecules that takes in account only single–electron wavefunctions. The DFT stems from calculation of the total electronic energy and the overall electron density distribution. The central idea in DFT is that there is a unique relation between the total electronic energy and the overall electron density [8, 10].

In addition, other properties of the system can be derived from the electron density, for example: partial charges, bond orders, etc. It is also possible to investigate the electron density response to the addition or the removal of electron.

1.2.1 Hohenberg–Kohn theorems

The Hohenberg–Kohn formulation of the DFT applies to any system of interacting particles in an external potential, including problems of electrons with stationary nuclei, whose Hamiltonian can be written in the form (1.8). This approach is based on two theorems [14].

- Theorem I: For any system of interacting particles in an external potential $\hat{V}_{\text{ext}}$, the potential $\hat{V}_{\text{ext}}$ is determined uniquely, except for a constant, by the ground state particle density $n_0(\mathbf{r})$.
- Theorem II: A universal functional for the energy $E[n]$ in terms of the density $n(\mathbf{r})$ can be defined, valid for any external potential $\hat{V}_{\text{ext}}$. For any particular $\hat{V}_{\text{ext}}$, the exact ground state energy is equal to the global minimum value of this functional $E[n]$, and the density $n(\mathbf{r})$ that minimizes the functional is the exact ground state density $n_0(\mathbf{r})$.

It follows from these two theorems that the electronic system and its properties are exactly determined by the ground state electron density $n_0(\mathbf{r})$. This is due to the uniqueness of the Hamiltonian for a particular set of particles. Furthermore, theorem II implies that the ground state is unambiguously determined by the energy functional $E[n]$. Proofs of these claims and corollaries can be found in [8].

Although these statements explicitly link the density functional to the external potential and the wavefunction, the H.–K. approach does not give any guidance on how to identify this functional. Only further approaches, such as Kohn–Sham ansatz, provide this information [8].

1.2.2 Kohn–Sham approach

This approach, one of the most widely used for studying electronic structures, replaces the set of interacting particles with an auxiliary system of independent particles. Examining the electron density and other properties of such a system is simpler and the solution to that task can be found accurately. This procedure gives the identical electron density as the original system. In principle, the electron density of the original system and the properties that can be calculated from it do not differ from the density of the auxiliary system. All approximation is included in the term expressing the exchange and correlation phenomenon, which also determines the accuracy of the calculation [8]. More detailed information about the exchange and correlation effect is summarized in section 1.2.3.

Kohn–Sham formulation of the DFT is based on two assumptions [15]

- The exact ground state density can be represented by the ground state density of an auxiliary system of non–interacting particles.
- The auxiliary Hamiltonian $\hat{H}^{\sigma}_{\text{aux}}$ is chosen to have the usual kinetic operator and an effective local potential $V^{\sigma}_{\text{eff}}(\mathbf{r})$ acting on an electron of spin σ at point $\mathbf{r}$.

This Hamiltonian and the effective potential are defined (assuming the use of Hartree atomic units[1]) in the form [8]

$$\hat{H}^{\sigma}_{\text{aux}} = \frac{1}{2}\nabla^2 + V^{\sigma}_{\text{eff}}(\mathbf{r}) \tag{1.9}$$

$$V^{\sigma}_{\text{eff}}(\mathbf{r}) = V_{\text{ext}}(\mathbf{r}) + V_{\text{Hartree}}[n] + V^{\sigma}_{\text{XC}}[n^{\uparrow}, n^{\downarrow}], \tag{1.10}$$

where $V_{\text{ext}}(\mathbf{r})$ expresses the effect of fixed nuclei on electrons and any other external potential acting on them, $V_{\text{Hartree}}[n]$ is the self interaction of the electron density and V_{XC} is the potential expressing the quantum effects of the many–body problem,

[1] System of units, where the physical quantities are expressed as multiples of the basic physical constants or their combinations. These basic constants are: the mass of an electron m_e, the magnitude of elementary charge e, the reduced Planck constant $\hbar$ and $4\pi\epsilon_0$, where ϵ_0 is the vacuum permittivity [12].

i.e., the exchange interaction and particle correlation. These phenomena are spin-dependent, more in section 1.2.3. The atomic units are used from now on.

The equation with this Hamiltonian (1.11) is called *Kohn–Sham equation*. This is another formulation of the Schrödinger equation (1.3).

$$\left(\frac{1}{2}\nabla^2 + V_{\text{eff}}^{\sigma}(\mathbf{r})\right)\psi_i^{\sigma}(\mathbf{r}) = \epsilon_i^{\sigma}\psi_i^{\sigma}(\mathbf{r}). \tag{1.11}$$

The wavefunction $\psi_i^{\sigma}(\mathbf{r})$ is a solution to the Kohn–Sham equation for the i–th electron with the spin σ. It should be noted that eigenvalues ϵ_i generally have no physical meaning. This is due to the fact that they are calculated not for the original system we are interested in, but for the auxiliary one, which consists of independent electrons. Therefore, eigenvalues of the original system are different [8].

Subsequently, the electron density of the auxiliary system with N electrons can be calculated as follows [8]

$$n(\mathbf{r}) = \sum_{\sigma}\sum_{i}^{N^{\sigma}} |\psi_i^{\sigma}(\mathbf{r})|^2, \tag{1.12}$$

where N^{σ} expresses the number of electrons with spin σ. This density can be further used to calculate system properties that depend on the electronic structure.

The ground state energy can be written in the form [8]

$$E_{\text{KS}} = T_{\text{S}}[n] + \int V_{\text{ext}}(\mathbf{r})n(\mathbf{r})d\mathbf{r} + E_{\text{Hartree}}[n] + E_{\text{XC}}[n] + E_{\text{II}}, \tag{1.13}$$

where $[n]$ expresses the functional depending on the density, the density $n(\mathbf{r}, \sigma)$ then depends on the position and the spin, the integral represents the effect of the external field on the density, E_{Hartree} is the interaction energy of the density with itself corresponding to the potential $V_{\text{Hartree}}[n]$ from equation (1.10), $E_{\text{XC}}[n]$ is the exchange and correlation energy and E_{II} is the interaction among nuclei.

The exchange and correlation energy can be expressed as follows [8]

$$E_{\text{XC}} = \langle\hat{T}\rangle - T_{\text{S}}[n] + \langle\hat{V}_{\text{int}}\rangle - E_{\text{Hartree}}[n]. \tag{1.14}$$

From the form (1.14), it is apparent that all the approximation done by replacing the original system of interacting particles by the auxiliary system of non-interacting particles is included in the E_{XC} term, i.e., the difference of the mean kinetic energy from the single particle kinetic energy T_{S} and the difference in the interaction of electrons with each other. If the general form E_{XC} was known for any system, it would be possible to determine the exact ground state electron density for the original many–body system by solving the Kohn-Sham equations for independent particles. From such an electron density it would be possible to calculate the exact ground state energy of such system. Unfortunately, this is not possible, so this term needs to be approximated. It follows that the accuracy of the whole calculation depends mainly on this approximation [8]. This can be done in several ways, some of which are mentioned in section 1.2.3.

Numerical calculation of the density functional

The Kohn–Sham equations (1.11) are a set of Schrödinger–like independent–particle equations which must be solved. This calculation must be carried out under the condition that the effective potential $V_{\text{eff}}^{\sigma}(\mathbf{r})$ and the density $n(\mathbf{r})$ are consistent. The actual calculation is a numerical procedure that successively changes $V_{\text{eff}}^{\sigma}(\mathbf{r})$ and $n(\mathbf{r})$ to approach the self–consistent solution (SCF). The flow chart of the numerical procedure is shown in figure 1.1.

The calculation proceeds as follows

1. initial estimation of the electron density $n_{\text{in}}(\mathbf{r})$
2. calculation of the effective potential $V_{\text{eff}}^{\sigma}(\mathbf{r})$
3. finding a solution to the Kohn–Sham equations (1.11)
4. computation of the new electron density $n_{\text{out}}(\mathbf{r})$ from the solution gained in step 3
5. comparison of the input density $n_{\text{in}}(\mathbf{r})$ and the output density $n_{\text{out}}(\mathbf{r})$; if it differs less than the convergence condition, then $n_{\text{out}}(\mathbf{r})$ is the final electron density, otherwise $n_{\text{in}}(\mathbf{r}) := n_{\text{out}}(\mathbf{r})$ and return to step 2.

1.2.3 Exchange and correlation functionals

Both the exchange and correlation effects are of a quantum nature, so the corresponding energies are difficult to interpret. They occur in the case of a many–body system of particles. The exchange effect is the interaction between electrons with the same spin. This effect is necessary to ensure the antisymmetry of the wavefunction and the Pauli exclusion principle. The correlation term expresses the interaction between electrons with opposite spin, i.e., their spatial separation. It is a reduction of the probability of a particle occurrence near another particle [8, 10, 12].

As already mentioned in section 1.2.2, if this functional could be calculated analytically, then the solution of the electronic structure of the auxiliary system would precisely determine the electron density of the studied system. However, this is not possible, so it is necessary to approximate this functional. The most widely used approaches are the *Local density approximation* (LDA), or the *Local spin density approximation* (LSDA), the *Generalized–gradient approximation* (GGA) and the *Hybrid functionals* that use some parts of Hartree–Fock theory together with the DFT [8, 10, 12].

The computational time and hardware demands of the calculation depend on the chosen method of the exchange and correlation functional approximation. In general, the better approximation means the higher accuracy, but the task requires more computational time and resources [8].

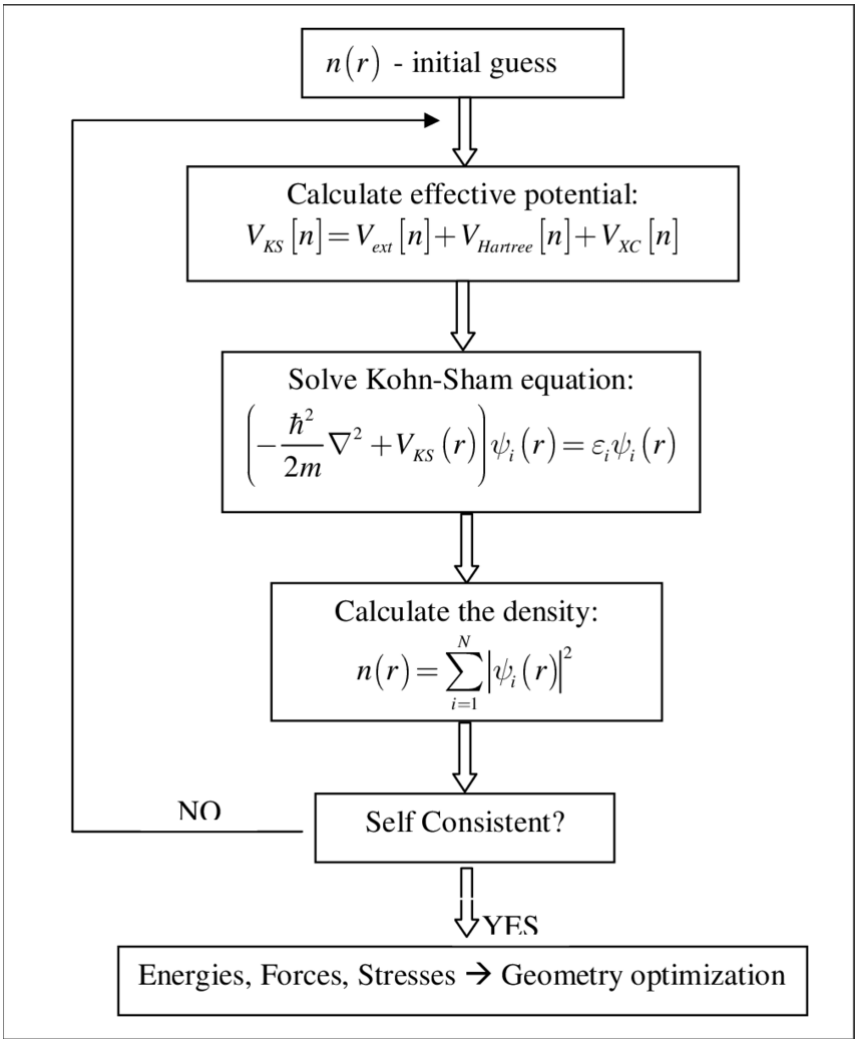

Figure 1.1 Flow chart of self-consistent Kohn-Sham calculation.[16]

The local spin density approximation

The local spin density approximation (LSDA) was proposed by Kohn and Sham [15]. It is based upon the uniform electron gas model, in which the electron density is a constant throughout space. The total exchange–correlation energy is an integral over all space with the exchange–correlation energy density at each point assumed to be the same as in a homogeneous gas with that density [8, 10].

In the case of spin polarized systems, the LSDA method is formulated in terms of densities $n^{\uparrow}(\mathbf{r})$ and $n^{\downarrow}(\mathbf{r})$ or the total density $n(\mathbf{r})$ and the fractional spin polarization ζ. For unpolarized systems the local density approximation (LDA) is found simply by setting $n^{\uparrow}(\mathbf{r}) = n^{\downarrow}(\mathbf{r}) = \frac{n(\mathbf{r})}{2}$ [8].

Unfortunately, the assumption that the studied system can be identified as the homogeneous gas causes the error of this approximation. In the cases of inhomogeneity, for example for strongly bonded electrons in molecules, the inaccuracy will be substantially greater than for almost ideal homogeneity occurring, e.g., weakly bonded electrons in metals [10]. On the other hand, the calculation is fast and can be performed on slower machines. For this reason, it is advisable to use this type primarily as indicative calculation, which is achieved in a short time. LSDA has stimulated ideas for constructing improved functionals such as Generalized–gradient approximation [8].

Examples of the LSDA functional are PWC [17] a VWN [18].

The Generalized–gradient approximation

The electron density in a molecule is typically far from spatial homogeneity. One way to improve the correlation functional is to make the functional dependent also on the density change, i.e., on the gradient. This approach is called the Generalized–gradient approximation [12]. Typically, the density varies more rapidly inside atoms than in the condensed matter that leads to more significant lowering of the exchange energy in atoms than in molecules and solids. GGA functionals provide results that are improving agreement with experiments compared to LDA functionals. However, GGA functionals still overstate exchange and correlation energies [8].

Functionals approximating the exchange and correlation parts are denoted separately. In practice, however, it is common to use established functional pairs, such as BLYP, where B (after Becke) stands for the exchange and LYP (Lee, Young, Parr) for the correlation energy. Nowadays, many GGA functionals exist. Commonly used ones are PW91 [17], PBE [19] and BLYP [20, 21]. In quantum chemistry calculations, the BLYP is the most widely used GGA functional [8].

Hybrid functionals

Hybrid functionals are a combination of the orbital–dependent Hartree–Fock approximation and the explicit density functional. Even though the Hartree–Fock approximation does not consider the electron correlation, in this approach the exchange can be calculated analytically. The final exchange and correlation energy can be

written in the simplest form as follows

$$E_{xc} = \frac{1}{2}(E_x^{HF} + E_{xc}^{DFA}), \tag{1.15}$$

where DFA stands for an LDA or GGA functional [8]. These functionals are the most accurate ones available. They are especially accurate for calculation of energies. For this reason, they are the most widely used in the quantum chemistry [8].

However, these functionals are the most demanding of computational time and hardware from those that are discussed here. This is caused by solving both the Kohn–Sham equations (1.11) and the Hartree–Fock problem for studied system [8]. In practice, this means that a calculation that takes a few minutes with a GGA functional will take several hours with a hybrid one.

An example of this type of functionals is B3LYP functional [22, 23] that is frequently used in the quantum chemistry [8].

1.2.4 Dispersion correction

The development of DFT approaches recently the accuracy required in order to model the physically and chemically very important London dispersion interactions [24, 25]. These interactions are necessary in theoretical simulations of weakly bonded systems, such as van der Waals interaction and hydrogen bonds. Furthermore, the inclusion also influences the accuracy of theoretical thermodynamics [25].

Computational codes provide several versions of the dispersion correction. Ones of the most used are from Grimme et al. [24–26]. Two–parameter Grimme dispersion correction (GD2) [26, 27] is implemented in DMol^3. Gaussian09 code and Orca software include also other versions of the Grimme dispersion correction: in addition to GD2, there are also three–parameter Grimme dispersion correction (GD3) [24] and three–parameter Grimme dispersion correction with Becke–Johnson damping (GD3BJ) [25].

The damping function modifies behaviour of the dispersion correction as the distance between two atoms approach zero, i.e., $R_{\mathrm{AB}} \to 0$. The dispersion energy should approach a constant (finite) value for $R_{\mathrm{AB}} \to 0$ [28]. However, the un–damped dispersion correction energy approaches $-\infty$ for $R_{\mathrm{AB}} \to 0$ [25, 28].

The inclusion of any dispersion correction leads to higher chemical accuracy. The choice of a version has a minor effect on the results [24]. Also, the influence of damping function is small [25]. In practice this also means that choosing a particular exchange-correlation functional is the accuracy–determining factor [24, 25].

1.2.5 Basis sets

The basis set is the set of mathematical functions from which the wavefunction is constructed. Each Molecular orbital (MO) is expressed as a linear combination of basis functions that in most cases are functions corresponding to atomic orbitals (AO). This theory is called Linear combination of atomic orbitals (LCAO) [12].

A MO is created as follows

$$\phi_k = \sum_{i=1}^{K} c_{ik}\psi_i, \tag{1.16}$$

where ϕ_k is the k–th molecular orbital, ψ_i is the i–th atomic orbital, c_{ik} are coefficients of the MO in AO basis set and K is number of AO functions in the basis set. The LCAO theory modifies Khon–Sham equations (1.11) into following form

$$\mathbb{HC} = \mathbb{SCE}, \tag{1.17}$$

where $\mathbb{H}$ is the Kohn–Sham matrix, $\mathbb{C}$ is the matrix of the coefficients c_{ik}, $\mathbb{S}$ is the overlap matrix that is responsible for the orthogonality of the basis functions and $\mathbb{E}$ is a diagonal matrix of the eigenvalues [10].

An obvious choice of the basis functions would be the Slater functions. Unfortunately, these functions are not convenient for an implementation due to the difficulty of evaluating the integrals [10]. Therefore, simpler basis functions are chosen, such as *Numerical functions* or *Gaussian functions*. Both type of the functions have the same properties that are further discussed in detail.

General properties of basis sets

The following features are generally supported by the basis sets used in MO calculations:

- *Polarization functions*: Functions corresponding to s and p orbitals do not have the sufficient mathematical flexibility to adequately describe the wavefunction of lower symmetry. The lower symmetry is necessary when orbitals are reordered in a molecular system, for example a water molecule. Better description is achieved by including basis functions corresponding to higher angular momentum l, i.e., $l + 1$, for each type of atom present [12].

- *Multiple zeta*: The minimal basis set contains only one function for each AO. This causes that the minimal basis set has several deficiencies (mentioned, for example, in [10]). These weaknesses of the minimal basis set can be solved by an addition of more basis functions with different diffusivity describing each AO. In the case of two basis functions for each orbital, the basis set would be *double zeta* and so on for higher numbers of functions (*triple zeta*, *quadruple zeta*, etc.). However, increasing the number of basis functions does not necessarily improve the model [10].

- *Split valence zeta*: In practical calculations, it turned out that for core orbitals, the addition of functions is redundant. In this case, there will be MOs that would be almost identical. The reason for this is that core orbitals are only weakly affected by chemical bonding, i.e., they are similar to corresponding AOs. For this reason, different numbers of basis functions describing the valence orbitals and the core ones are used [10, 12].

- *Diffuse functions*: The highest energy MOs of anions, highly excited electronic states, and loose super molecular complexes, tend to be much more spatially

diffuse. A serious problem can occur when a basis set does not allow a weakly bounded electron to localize far from the remaining density. This leads to significant errors in energies and other molecular properties. To reduce this effect, basis sets are often extended by the diffuse basis functions. Particularly for the calculation of acidities and electron affinities, diffuse functions are required [12].

Numerical Basis sets

The numerical basis sets are used in Material studio DMol^3 [29, 30] module. The basis functions are given numerically as values on an atomic-centred spherical-polar mesh. The function consists of the radial part and the angular part. The radial part $F(r)$ is obtained by numerically solving the atomic DFT equations and the angular part is the appropriate spherical harmonic function $Y_{lm}(\theta, \phi)$ for each basis function [31] that can be calculated from the following equation

$$Y_{lm}(\theta, \phi) = \sqrt{\frac{(2l+1)}{4\pi}\frac{(l-m)!}{(l+m)!}} \cdot \mathrm{e}^{im\phi} \cdot P_l^m(\cos\theta), \tag{1.18}$$

where P_l^m is an associated Legendre polynomial [8].

The numerical basis sets lead to a satisfying approximation of the real MOs and their shape can be considered almost realistic. Furthermore, basis set superposition effects [29], i.e., the interference of the basis functions of one molecule into the space of the other interacting molecule are minimized. This property of numerical functions is the result of manually setting the maximum possible distance when the orbital overlap is considered, so called orbital cut–off [29, 30].

Overview of numerical basis sets [31]:

- *MIN*: Minimal basis containing one basis function for each AO.
- *DN*: The double zeta basis set.
- *DNP*: The *DN* basis set with Polarization functions.
- *DNP+*: The *DNP* basis set with Diffuse functions.
- *TNP*: The triple zeta basis set with Polarization functions.

Gaussian basis sets

The general form of Gaussian functions is

$$f(\mathbf{r}) = x^a y^b z^c \exp(-\alpha \mathbf{r}^2), \tag{1.19}$$

where α determines the spatial extension of the function. Gaussian function with a large value of α does not spread very far, whereas a small value of α gives a large spread. The sum of a, b, c coefficients determines the order of Gaussian function [10].

Unfortunately, Gaussian functions do not correspond to the physical behaviour of orbitals and their shape. This leads to unacceptable errors.

A main advantage of Gaussian functions is that the product of two Gaussian functions is again a Gaussian function. This feature helps to overcome the problem with Gaussian functions mentioned above. Each AO is represented as a product of primitive Gaussian functions. The final Gaussian function is called as contracted Gaussian function. This approach leads to better description of the AOs [10, 12].

Overview of Gaussian basis sets [10]:

- *STO–nG*: The minimal basis set containing one basis function created from n primitive Gaussian functions for each AO.
- *3–21G*: The split valence double zeta basis set, i.e., 3 primitive Gaussian functions produce one basis function for core orbitals and there are two basis functions for valence orbitals (one contracted from two primitive Gaussian function and the other is primitive Gaussian function).
- *6–311G*: The single zeta for core orbitals and triple zeta for valence orbitals basis set.
- *6–311G***: The *6–311G* basis set with Polarization functions, the first * symbolizes the use of the Polarization functions for d orbitals of non–hydrogen atoms and the other * indicates the application of the Polarization functions for p orbitals of hydrogen atoms, equivalent to *6-311G(d,p)*
- *6–311G++*: The *6–311G* basis set with Diffuse functions, the first + symbolizes the use of the Diffuse functions for s and p orbitals of non–hydrogen atoms and the other + indicates the application of the Diffuse functions for s orbitals of hydrogen atoms.

Karlsruhe basis sets

Karlsure Def2 basis sets were proposed by Ahlrichs and al. [32–34]. Theses basis sets functions are Gaussian type, but, comparing to 6-311G, more functions are included. Karlsure basis sets are based on fully optimized contracted Gauss-type orbital basis sets [35, 36]. The Karlsruhe basis sets are commonly used in quantum chemistry and they are considered as the best compromise between the accuracy and the computational resources.

Overview of Karlsruhe basis sets [32–34]:

- *Def2SV*: Split valence Karlsruhe basis set.
- *Def2SVP*: The Def2SV basis set with Polarization functions.
- *Def2TZV*: Triple zeta valence Karlsruhe basis set.
- *Def2TZVP*: The Def2TZV basis set with Polarization functions.
- *Def2QZV*: Quadruple zeta valence Karlsruhe basis set.

1.3 Coupled cluster theory

Only the basics of Coupled cluster theory are mentioned in this thesis, for more details see [12, 37–44]. Coupled cluster (CC) [37, 38] theory is one of the best methods for estimating the electron correlation energy [12].

The main idea of CC theory is that the full-Configuration interaction wave function (i.e., the 'exact' one within the basis set approximation [12]) can be described as

$$\Psi = \exp^{\mathbf{T}} \Psi_{HF}, \tag{1.20}$$

where $\mathbf{T}$ is the cluster operator. This cluster operator [12] is defined as

$$\mathbf{T} = \mathbf{T}_1 + \mathbf{T}_2 + \mathbf{T}_3 + \cdots + \mathbf{T}_N, \tag{1.21}$$

where N is the total number of electrons and the various $\mathbf{T}_i$ operators generate all possible determinants having i excitations from the ground state [12]. For example,

$$\mathbf{T}_2 = \sum_{i<j}^{occ.} \sum_{a<b}^{vir.} t_{ij}^{ab} \Psi_{ij}^{ab}, \tag{1.22}$$

where the amplitudes t are determined by the constraint that equation 1.20 must be satisfied. The expansion of $\mathbf{T}$ ends at N because no more than N excitations is possible [12].

The accuracy and computational costs depends on the number of excitations that are taken into account. In practice, the cost of including single excitations (i.e., $\mathbf{T}_1$) in addition to double excitations ($\mathbf{T}_2$) is worth the increase in accuracy. This is the CCSD [38, 41, 43, 44] model. The scaling behaviour of CCSD is on the order of $O(N^6)$ [12]. Inclusion of connected triple excitations (i.e., those that can be calculated as products of $\mathbf{T}_1$ and $\mathbf{T}_2$) defines CCSD(T) [42]. In the case of the inclusion of exact $\mathbf{T}_3$, it is CCSDT method. However, CCSDT is very computationally expensive (scaling as $O(N^8)$), making it applicable for the smallest molecules only [12]. CCSD and CCSD(T) are available in Gaussian09 code and Orca software that also includes further approximations that leads to lowering computational costs.

1.4 Solvent Models

The calculation without any solvent model includes only atoms of a molecule in the vacuum. Such calculation can be considered as the gas phase calculation. This can be done due to the assumption that in certain approximations molecules can be treated as isolated, i.e., non-interacting species. Then our simulated system of molecules can be represented by a single molecule itself [12]. In reality, the studied molecules are often in a solution that is affecting, for example, the geometry of the molecules, and other properties.

Two possible ways to simulate this effect are mentioned here, one is to use an explicit model, i.e., to include solvent molecules in the calculation. However, this

greatly increases the number of atoms that are included in the calculation, which then leads to an increase of the computational cost. Such a situation is simply not practical with the present computational resources [45].

The other option is to use an implicit model. This approach is based on the replacement of a huge number of individual solvent molecules by a dielectric continuum with permittivity ϵ, which has properties similar to that set of solvent molecules [12]. A cavity is created around atoms of the studied molecule, where the continuum is neglected [46]. Example of such cavity is presented in figure 1.2. Materials Studio DMol^3 includes the *Conductor-like screening model* (COSMO) [46, 47], and Gaussian typically uses the *Polarizable continuum model* (PCM) [48, 49].

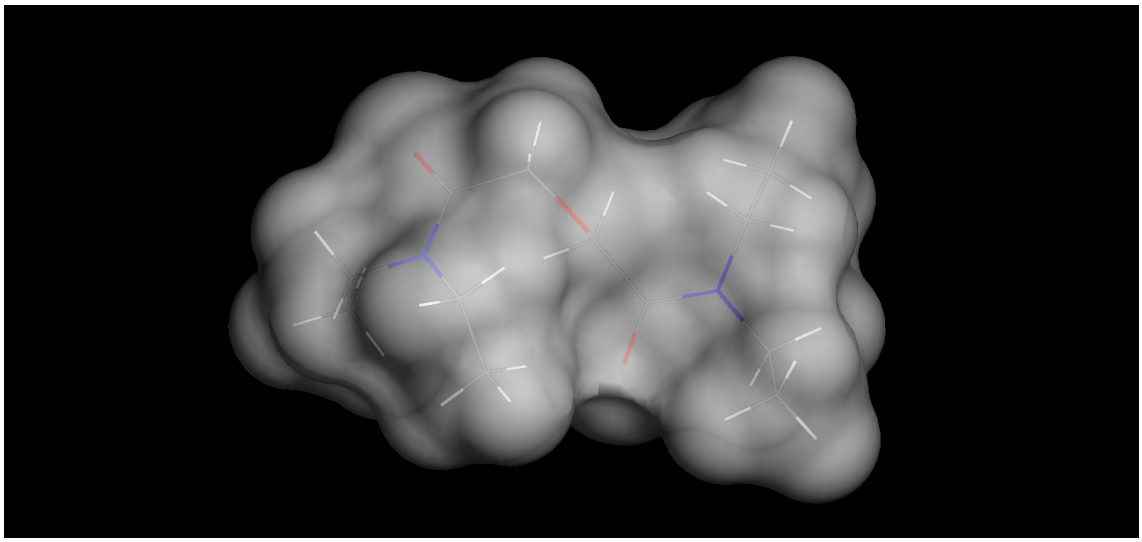

Figure 1.2 Cavity of the implicit solvent model COSMO for TEDGA; (settings: DMol^3, DNP, B3LYP, GD2, COSMO)

1.5 Potential Energy Surface

The consequence of the Born–Oppenheimer approximation (section 1.1.1) is that the ground state energy of a molecule can be assumed only as a function of the nuclei positions **R**. Any movement of some or all the nuclei causes the change of the energy. The new nuclear coordinates can be the result of a simple process, for example a single bond rotation, and the magnitude of the energy change depends on the type of the change that happened [10]. These energy changes can be considered as movement on a multidimensional surface. This surface is called the *Potential Energy Surface* (PES) and stationary points on the PES are important for searching the geometries with the minimal energy and the transition states. Minimum points on the PES are stable conformations of the system and saddle points correspond to transition states [50], i.e., such structures that correspond to the highest point on the pathway between two minima [10]. Calculations of these points are extremely difficult due to the fact that PES is multidimensional function of the coordinates.

1.5.1 Geometric optimization

The geometric optimization is a process that minimizes the energy of the studied system by changing the relative positions of atoms. The geometric optimization consists of a calculation of the SCF cycle, followed by the determination of forces acting on individual atoms at their current position. Changes in these values are compared to the convergence conditions, i.e., if the changes are smaller than the condition, it is assumed that the energy minimum is reached. If the convergence conditions are not fulfilled, the positions of the atoms are shifted and the SCF cycle is recalculated [31].

Molecules that consist of many simple bonds are very flexible and therefore have numerous possible conformations that have different energies depending on the PES's shape [10]. Consequently, the probability that a molecule has a given conformation varies in time. The properties of a particular molecule are determined by the most probable conformations whose energy is minimal. In order to reduce the possibility that the conformations of the molecules only converge to the local energy minimum, a conformational analysis with several initial coordinates must be performed before stability studies of the molecules are done [10].

It is not guaranteed that the minimum found by using known algorithms for searching extremes of functions is the global minimum [10]. This problem can also be influenced by the choice of the exchange and correlation functional. Practice shows that it is often better to first use a less accurate functional approximation and then apply a more accurate one.

1.5.2 Searching the transition state

Calculation of the transition states, i.e., such structures that correspond to the highest point on the pathway between two minima [10], is based on modified minimization algorithms. For example, Gaussian code includes the STQN method [51, 52] or the Berny algorithm using GEDIIS [53]. The latter method uses a quadratic synchronous transit approach to get closer to the quadratic region of the transition state and then uses a quasi-Newton or eigenvector-following algorithm to complete the optimization [54].

1.6 Chemical kinetics and reactivity

A reaction coordinate is defined [55] as a geometric parameter that changes during the conversion of one (or more) reactant molecular entities into one (or more) product molecular entities and whose value can be taken for a measure of the progress of an elementary reaction (for example, a bond length or bond angle or a combination of bond lengths and/or bond angles; it is sometimes approximated by a non-geometric parameter, such as the bond order of some specified bond) [55].

There are two definitions how a reaction along the reaction coordinate occurs. One definition is the minimum energy path (MEP), which defines a reaction coordinate in which the absolute minimum amount of energy is necessary to reach each point on

the coordinate [56]. A second definition is a dynamical description of how molecules undergo intramolecular vibrational redistribution until the vibrational motion occurs in a direction that leads to a reaction [56]. The MEP is a path on the PES between two minima corresponding to reactants and products with the minimal energy changes [57]. This definition allows a simple description of the reaction steps [56]. The dynamical definition more corresponds to the real behaviour of molecules [56].

The rate constant of a reaction k describes the chemical kinetics of the reaction. The simplest expression for the temperature dependence of k is described by the Arrhenius equation [56]:

$$k = A \exp^{-\frac{E_a}{RT}}, \tag{1.23}$$

where E_a is the activation energy per mol and A is the pre–exponential factor. E_a and A can be obtained from experimental data or *ab initio* calculations. However, their determination from *ab initio* calculations can be very difficult. The activation energy is influenced by the used level of theory. Consequently, the calculated rate constant differs from the experimentally determined one. The pre–exponential factor includes the influence of the vibrational frequencies of the transit state (especially, the imaginary one) [58, 59]. Several approaches have been introduced, but using the specific approach is problem dependent. For this reason and because of simplicity, only the activation and the reaction energy are discussed in this thesis.

1.6.1 Transition state theory

Simply using the activation energy E_a assumes that the only way a reaction occurs is along the MEP. The transition structure is the maximum along this path, which is used to obtain the activation energy (energy difference between the transition state and reactants) [56, 60].

These calculations require information about the shape of the PES around the transition structure, frequently using the reaction coordinate or an analytic function describing the entire PES. Most of the *ab initio* methods calculate the Hessian matrix in the first step and then use approximately updates of the Hessian matrix in each step. Another possibility is to calculate the Hessian matrix in each step, but this approach is extremely computationally and time consuming. The transition structure has one imaginary vibrational frequency [56, 60]. Their calculation is used as the validation of the transition state structure. For more information on how transition state calculations are performed, see section 1.5.2 and Refs. [10, 51, 56, 57, 60].

1.7 Properties and functions for stability description

The stability of molecules can be assessed based on various function or property of the electron density. For this reason, several properties that indicate stability must be calculated and interpreted together. Properties of the electron density that are used in this work are summarized in this section.

1.7.1 Population analysis

Population analysis methods allow the partition of the electron density $n(\mathbf{r})$ among the nuclei. The result is a number that corresponds to the number of electrons 'belonging' to each nucleus. The numbers are interpreted as partial charges on individual atoms, which makes it easier to study the distribution of charges in molecules [10].

Several methods are used and the most common ones are mentioned in this work. These are Mulliken population analysis [10, 61–63], Hirshfeld population analysis [63, 64] and Natural population analysis [56].

Mulliken population analysis

Mulliken population analysis [61] is based on the approach that electrons are distributed with respect to the occupancy of AOs. The main assumption is that the AO belongs to the atom on which it is centred. Electrons that occupy this AO belong to that atom. It is also implicitly assumed that AOs retain their shape in molecules [10, 62, 63].

The Mulliken analysis is a simple calculation performed after a SCF has been successfully done. For this reason, it is often used. However, errors can often occur. First, Mulliken analysis is closely linked to the LCAO theory (section 1.2.5). That means that the choice of the basis set type is important, especially when basis function that are centred on other locations then atoms are included. This method will fail when basis functions are centred on other locations than nuclei are included in the basis set, or when the basis functions have no centre, as in the case of plane waves. Secondly, if diffuse basis functions are included in the basis set, the Mulliken population analysis may become unstable. Diffuse functions decay slowly while extending away from the nucleus. Hence, the electron density is remote from this nucleus. The Mulliken population analysis is not able to reliably partition such type of electron density [63].

It is possible, based on this method, to determine the bond orders, i.e., how many electrons form each bond. In chemistry, bond orders are formally integers, but in fact electrons need not be present only in the bonding region over time. This means that bonds of the same chemical type can have different order values depending on their surroundings. Later, Mayer approach [65] modifies Mulliken theory to more relevant results. However, both methods depend on the basis set. For this reason, they should be used only as the first approximation of the studied electronic structure [10].

Hirshfeld population analysis

Hirshfeld population analysis [64] proposes to divide the electron density among the atoms in a molecule using the promolecular density. The promolecular density $n^0(\mathbf{r})$ is gained by summing the electron density of each atom A ($n^0_{\mathrm{A}}(\mathbf{r})$) in an isolated state. The final electron density $n_{\mathrm{A}}(\mathbf{r})$ is calculated for the atom A as follows

$$n_{\mathrm{A}}(\mathbf{r}) = \frac{n^0_{\mathrm{A}}(\mathbf{r})}{n^0(\mathbf{r})} n(\mathbf{r}). \tag{1.24}$$

Partial charges can be determined from it [63].

Hirshfeld method is still slightly dependent on the basis set as Mulliken analysis, but the influence on results is reduced. However, new problems are introduced. The main one is that the promolecular density is a non–physical concept, because it disturbs the Pauli principle. This implies that the promolecular density is not defined uniquely. Another problem is that the Hirshfeld atomic charges are virtually zero for covalently bonded systems [63].

Natural population analysis

Natural bond order analysis (NBO) is a whole set of analysis techniques. The natural population analysis (NPA) is also part of the NBO analysis. NPA is used for obtaining occupancies and partial charges on each atom. The NBO uses the natural orbitals instead of the molecular orbitals directly. Natural orbitals are the eigenfunctions of the first–order reduced density matrix. These orbitals are localized and orthogonalized. Thus, this method is able to simulate different chemical environments for the same element. Furthermore, an integration can be done to obtain charges on the atoms. NBO also provides a method for a calculation of bond orders [56].

Results gained by NBO are less dependent on the choice of the basis set than the Mulliken method. However, basis set effects are still slightly apparent. NBO is widely used technique and is available in many software packages [56].

1.7.2 Electrostatic potencials

The electrostatic potential (ESP) $\varphi(\mathbf{r})$ at a point $\mathbf{r}$ is defined as the work done to bring unit positive charge from infinity to the point $\mathbf{r}$. The ESP reflects contributions from the nuclei and from the electrons [10].

The nuclei contribution to the ESP from M nuclei is

$$\varphi_{\mathrm{nucl}}(\mathbf{r}) = \sum_{A=1}^{\mathrm{M}} \frac{Z_A}{|\mathbf{r} - \mathbf{R}_A|}. \tag{1.25}$$

The electronic contribution is obtained from the electron density as follows

$$\varphi_{\mathrm{el}}(\mathbf{r}) = -\int \frac{n(\mathbf{r})}{|\mathbf{r}' - \mathbf{r}|} d\mathbf{r}'. \tag{1.26}$$

The total ESP is the sum of those contributions

$$\varphi(\mathbf{r}) = \varphi_{\mathrm{nucl}}(\mathbf{r}) + \varphi_{\mathrm{el}}(\mathbf{r}). \tag{1.27}$$

The electrostatic energy between a point charge q at a location $\mathbf{r}$ and the molecule can be calculated as follows [10]

$$E_{\mathrm{ESP}}(\mathbf{r}) = q\varphi(\mathbf{r}). \tag{1.28}$$

The ESP is useful for studying interactions between molecules, because electrostatic forces are responsible for long–range interactions between them. Further, the ESP can be used for analysis of interactions with electrophiles. Regions of the ESP where the electrophilic attack might occur are the most negative parts of molecule [10].

Partial charges can be calculated from the ESP. This is done by fitting the charges to correspond to the ESP. Partial charges determined by fitting to the ESP can well represent the behaviour of the molecule. However, this happens only for some cases. Unfortunately, results are sensitive to changes caused by geometric modifications of molecules. This fact must be considered during an interpretation of such calculated partial charges [66].

In practise, it is convenient for an interpretation to map the ESP of a molecule to the electron density.

1.7.3 Chemical hardness

Chemical hardness η is a property that classifies acids and basis and its definition is [67, 68]

$$\eta = \left(\frac{\partial^2 E}{\partial N^2}\right)_{V_{\text{ext}}} = \left(\frac{\partial \mu}{\partial N}\right)_{V_{\text{ext}}}, \tag{1.29}$$

where E is energy of the electronic system, μ is its chemical potential and N is the number of electrons in the system.

Chemical hardness is related to both the HOMO–LUMO energy gap [69, 70] and Fukui functions [63]. These relations are discussed in following sections.

1.7.4 Orbitals

The problem with orbitals is that they are not measurable and therefore there is no unique definition of them. Different computational methods can provide a different orbital structure even if the electron densities are identical. It must be noted that the orbitals gained by the Kohn-Sham DFT correspond to the auxiliary non-interacting particle system, not to the real studied system. These systems are only connected by the electron density defined in equation (1.4). Therefore, the MOs obtained by the DFT calculation approximately correlate with real MOs of the many–body system. Despite all these approximations, the orbitals of the auxiliary system can be used to describe physical and chemical properties of molecules. However, any conclusion resulting from the orbitals must always be supported by other calculated properties [10].

The most interesting orbitals are the highest occupied molecular orbital (HOMO) and the lowest unoccupied molecular orbital (LUMO) [10].

The HOMO–LUMO gap is related to chemical hardness and kinetic stability of a molecule. A hard molecule has a large gap and a soft one has a small gap. Generally, the lower HOMO–LUMO gap implies lower excitation energies and conse-

quently molecules with a small gap are more reactive than the ones with a larger gap [69, 70]. Unfortunately, the information gained from the size of the HOMO-LUMO gap is general for a whole molecule without detailed information about the hypothetical reaction mechanism. Therefore, e.g., the initial locations of the reaction are unknown.

1.7.5 Fukui functions

Fukui functions [71] are a qualitative way of measuring and displaying the reactivity of regions of a molecule. These functions are based on the frontier orbital theory of Fukui [72]. The method connects the reactivity of a molecule with respect to electrophilic and nucleophilic attacks to the charge density [31]. Three types of the Fukui functions exist corresponding the type of attack, $f(\mathbf{r})$ for radical attack, $f(\mathbf{r})^+$ for nucleophilic attack and $f(\mathbf{r})^-$ for electrophilic attack. These functions express the change of the electron density caused by the addition or removal of an electron. Generally, it is demonstrated that the larger the value of the Fukui function, the greater the reactivity of the corresponding site [63].

The original definition of the Fukui function is [63]

$$f(\mathbf{r}) = \left(\frac{\partial n(\mathbf{r})}{\partial N}\right)_{V_{\text{ext}}} = \left(\frac{\delta\mu}{\delta V_{\text{ext}}(\mathbf{r})}\right)_N, \tag{1.30}$$

where the derivation is done according to the number of electrons N in the system, but there is a discontinuity problem. For this reason, one-sided derivatives are introduced as follows

$$f(\mathbf{r})^+ = \left(\frac{\partial n(\mathbf{r})}{\partial N}\right)^+_{V_{\text{ext}}}, \tag{1.31}$$

$$f(\mathbf{r})^- = \left(\frac{\partial n(\mathbf{r})}{\partial N}\right)^-_{V_{\text{ext}}}, \tag{1.32}$$

where equation (1.32) corresponds to the case in which the system donates the charge, because it is interacting with an electrophilic reagent (electrophilic Fukui function $f(\mathbf{r})^-$). Equation (1.31) corresponds to the case in which the system accepts the charge, because it is interacting with a nucleophilic reagent (nucleophilic Fukui function $f(\mathbf{r})^+$) [63].

Accordingly, to the original definition in equation (1.30), Fukui function also represents the response of the chemical potential of a system to a change in external potential. Also, the connection between the chemical hardness and the Fukui function can be seen from the definitions (equations (1.29) and (1.30)) [63].

The problem is that the number of electrons N is an integer, so making an infinitesimal change in the number of electrons makes no physical sense. Therefore, these functions can be redefined as follows

$$f(\mathbf{r})^+_N = n_{N+1}(\mathbf{r}) - n_N(\mathbf{r}), \tag{1.33}$$

$$f(\mathbf{r})^-_N = n_N(\mathbf{r}) - n_{N-1}(\mathbf{r}), \tag{1.34}$$

where $n_{N+1}(\mathbf{r})$ is the electron density of the system with $N+1$ electrons . Using one-electron orbital picture, Fukui functions can be than approximately defined using the HOMO and LUMO orbital densities [63].

The last type of the Fukui function is the radical one defined as follows

$$f(\mathbf{r})_N = \frac{1}{2}(f(\mathbf{r})_N^+ + f(\mathbf{r})_N^-). \tag{1.35}$$

This radical Fukui function corresponds to the radical attack and is simply the average of the electrophilic and nucleophilic Fukui functions [63].

The functions defined in equations (1.33), (1.34) and (1.35) are collectively referred to as Fukui functions and are one of the basic properties describing the reactivity of molecules in terms of electronic structure.

Fukui charges

More quantitative predictions can be obtained from the condensed Fukui functions for an atom, also named as Fukui charges. These charges can be easily calculated after partial charges are determined. Fukui charges are the values of volumetric Fukui functions related to individual atoms. Fukui charges provide easily interpretable information about the reactivity of the molecule. Their calculation for k–th atom is done as follows [31, 63]

$$f_k^- = q_k - q_k^{\text{cation}}, \tag{1.36}$$

$$f_k^+ = q_k^{\text{anion}} - q_k, \tag{1.37}$$

$$f_k = \frac{1}{2}(q_k^{\text{anion}} - q_k^{\text{cation}}) \tag{1.38}$$

where q_k, q_k^{cation} and q_k^{anion} is respectively the partial charge on the k–th atom in the case of a neutral, positively charged or negatively charged molecule determined by the used population analysis.

From the definitions in equations (1.37), (1.36) and (1.38), it is obvious that the calculation of Fukui charges needs less time compared to the calculation of Fukui functions. However, the information provided by Fukui charges is less detailed than that in the case of Fukui functions [63].

Chapter 2

Computational part

This chapter is focused on the application of the DFT and CC calculations for an assessment of the radiolytic stability of the selected molecules. These calculations are based on the theory described in chapter 1. The calculations are done using DMol^3 module of Materials studio [29, 30], Gaussian09 code [73] and Orca 4.0.1.2 Release [74, 75]. This Master's thesis follows up the Bachelor thesis [5] and the Ref. [6]. Simple models of the acid effect are proposed and investigated. Additionally, the degradation reaction mechanism based on a hydrogen abstraction is proposed and studied.

The following properties of the electron density are investigated: HOMO and LUMO orbitals, Fukui functions, Fukui charges, partial charges, bond orders and electrostatic potentials. Further, transition states for the hydrogen abstraction degradation reaction mechanism are determined.

2.1 Diglycolamides

The diglycolamide (DGA) family of ligands is one of the considered group of prospective organic extractants for the separation processes. The DGAs are especially suitable for the extraction of trivalent actinide and lanthanide ions from the active waste, for example americium, europium, and curium.

The general chemical formula of the DGA is in figure 2.1. R^1, R^2 and R^3 are

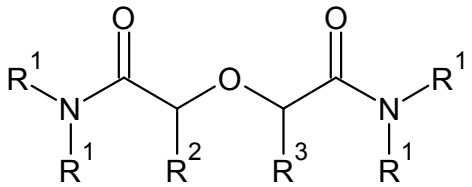

Figure 2.1 Chemical formula of the Diglycolamide

carbon chains, which may be of varying length and complexity. These chains are responsible for different properties of the individual representatives of the DGA

group. The chain length determines solubility in water or organic solvents. When chain R^1 is a methyl group or an ethyl group, then the agents are hydrophilic. Lipophilicity of a molecule increases with higher complexity of the chain R^1. For example, TMDGA (R^1=CH_3; Figure 2.2 (a)) and TEDGA (R^1=C_2H_5; Figure 2.2 (b)) are hydrophilic [76], but TODGA (R^1=C_8H_{17}; [2]) is lipophilic. In this work, R^2 and R^3 chains are hydrogen atoms or methyl groups depending on the selected ligand. A methyl group works usually as a donor of the electron density. The main purpose of this work is to investigate whether or not the addition of the methyl group on the ether carbon or the presence of longer alkyl side chains results in the higher hydrolytic or radiolytic stability of the studied ligands. A significant effort to answer this question was given also in the mentioned previous theoretical and experimental works. The molecules further contain three oxygen atoms (two represent carbonyl groups and one represents the ether group). Those groups that contain oxygen atoms are responsible for the complexation with the metal ions (actinide and lanthanide atoms).

The stability of the following molecules is investigated in this thesis.

- TMDGA (N,N,N',N'-tetramethyl-diglycolamide; 2,2'–oxybis(N,N-dimethylacetamide))
- TEDGA (N,N,N',N'-tetraethyl–diglycolamide; 2,2'-oxybis(N,N-diethylacetamide))
- Me–TEDGA (2-(2-(diethylamino)-2-oxoethoxy)-N,N-diethylpropanamide)
- Me_2–TEDGA (2,2'-oxybis(N,N-diethylpropanamide)).

Their chemical formulas are presented in figure 2.2. All of these molecules are hydrophilic, i.e., water-soluble [76].

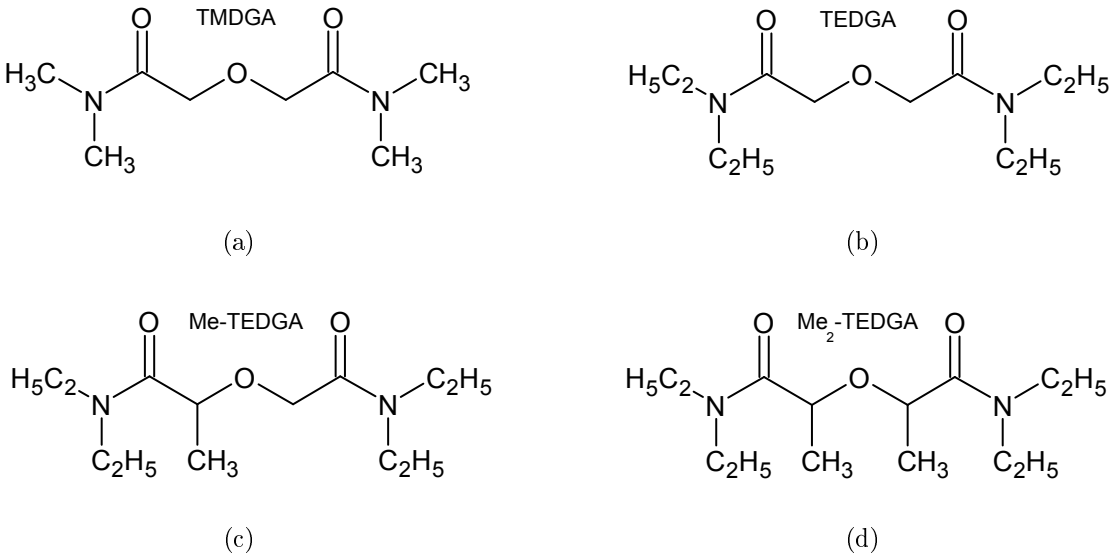

Figure 2.2 Chemical formula of (a) TMDGA, (b) TEDGA, (c) Me–TEDGAa (d) Me_2–TEDGA

TEDGA is used in the EXAm process (Extraction of Americium) [77] or the ALSEP precess (Actinide Lanthanide Separation) [78]. The role of TEDGA in these processes is as an aqueous stripping agent and a hold back agent, i.e., TEDGA makes preferably complexes with Curium (Cm) or other lanthanide ions (Ln) than with Americium (Am). Subsequently, the selectivity ratio Am/Cm and Am/Ln of the extractant in the organic phase is higher. For example, DMDOHEMA molecule [79] is used in the EXAM process as an extractant.

There have been multiple experimental works focused on investigating the radiolytic and hydrolytic stability of DGA-type ligands. This work is largely based on the study by Wilden et al. [3], which focuses on representatives of the DGA family of extractants mentioned above. Their hydrolysis and radiolysis were investigated separately, because the hydrolysis of TEDGA caused by nitric acid appears to occur by multiple mechanisms during the experiments. The rate of the hydrolysis was so remarkable that radiolysis needed to be investigated in pure water [3]. The DGA samples were irradiated to target the absorbed doses from 0 to 150 kGy at 23 ± 2 °C [3]. After the irradiation, the samples were analysed by the high performance liquid chromatography–electronspray ionization mass spectrometry/mass spectrometry. Kinetics measurements revealed high rate constants for DGA reactions with the hydroxyl radical OH•, suggesting its importance in the mechanism of their radiolytic degradation in water. A decrease in dose constants with increasing molecular weight of DGAs and the measured rate constants indicates that the most important degradation mechanisms of the radical reaction are an electron transfer and a hydrogen abstraction. Wilden et al. concludes that the radiolytic stability for studied molecules increases with following trend TMDGA < TEDGA < Me–TEDGA < Me_2–TEDGA [3].

Another study of these DGA derivatives in concentrated aqueous nitrate solution was done by Horne et al. [4] with similar experimental setup as Wilden et al.. Horne et al. demonstrated that: (i) the studied hydrophilic DGAs undergo first-order decay with an average dose constant of $(-3.18 \pm 0.23) \cdot 10^{-6}$ Gy^{-1}; (ii) their degradation product distributions are similar to those under pure water conditions, except for the appearance of NOx adducts; and (iii) radiolysis is driven by hydroxyl and nitrate radical oxidation chemistry moderated by secondary degradation product scavenging reactions [4]. Overall, the radiolysis of hydrophilic DGAs in concentrated, aqueous nitrate solutions is significantly slower and less structurally sensitive than under pure water conditions, similar to their lipophilic analogs. Acid hydrolysis, not radiolysis, is expected to limit their useful lifetime[4].

2.1.1 Degradation reaction mechanisms

This study presumes that indirect radiolysis is the dominant process due to low concentration of the ligand in solvent [3]. For this case, the degradation is initiated by radiolysis of the solvent molecules. Consequently, these products interact with ligands causing their degradation. Two possible reaction mechanisms are taken in account in this Master's thesis. The first one is based on a radical attack that is initiated by a hydrogen abstraction. The hydrogen abstraction was suggested as one of the dominant initiators of degradation related to lipophilic DGA ligands [3, 6].

The other one is initiated by the electron transfer from one of the amide groups [3].

The hydrogen abstraction is considered mainly on the ether carbons; this was confirmed in previous works [5, 6]. Despite of that authors of the experiment suggested that abstraction is more likely to occur on the side chains. The abstraction is performed by radicals created by the radiolysis of the solvent. The role of the radical can be played predominantly by the hydroxyl radical OH• in the case of aqueous solution [3] or by the hydrogen radical H• in the case of organic solvents [80]. Subsequently, the neighbouring ether bond (the single C-O bond) ruptures [7]. The specific reaction schemes are presented in section 2.3.7. For this reaction mechanism, transition states are calculated and energy diagrams are determined for the studied ligands.

The hypothetical degradation based on the electron transfer is initiated by the oxidation nature of the hydroxyl radical OH• [3]. This transfer probably happens on one of the amide groups. This leads to the formation of the radical cation $[DGA]^{\bullet+}$. Afterwards, the ether (C–O) or the amide (C–N) bond ruptures.

2.1.2 Acid influence

In the previous works [5, 6] the potential effect of nitric acid was neglected. Also, during the experiment [3], DGA molecules were dissolved in pure water, so no effect of acid was considered. Nevertheless, DGAs are commonly used in nitric acid solution concentrated enough to contain undissociated HNO_3 molecules in a significant concentration [3]. Possible formation of micellar complexes of TODGA and nitric acid molecules was reported based on molecular dynamics simulations [81]. The acid influence was already considered in other theoretical studies. In the work by Matveev et al. [82], a simple model of the acidic environment (based on addition of a single H_3O^+ cation) brought already significant results in the stability prediction by the DFT.

In work of Horne et al. [4], gamma radiolysis of selected hydrophilic DGA ligands study was performed in concentrated aqueous nitrite solution. The rate of radiolytic degradation was significantly reduced in concentrated aqueous nitrate solution relative to pure water conditions [4]. The reason for this reduction of the dose constant must be due to the reduction of some water radiolysis products (in particular, e_{aq^-} and the H•). In concentrated, aqueous nitrate solutions, there is negligible contribution from the e_{aq^-} and the H•, as both are rapidly scavenged by NO_3^- within the lifetime of the radiation chemical track [4]. This suggests that the acid does not influence directly on the extractant. On the contrary, the acid molecule preferably reacts with the radicals from the solvent radiolysis and thereby protects the extractant molecules. Horne et al. [4] concluded that the hydrophilic DGA degradation in the presence of concentrated, aqueous nitrate is driven by OH• and, to a lesser extent, $\bullet NO_3$ oxidation, as the reducing products of water radiolysis are inhibited by NO_3^- scavenging [4].

In this work, three possible ways of including the acid influence are tested. The first model is based on including one hydrogen cation H^+ in the complex together with the ligand molecule. The other two models are based on the incorporation of either H_3O^+ cation (this model was also applied in [82]) or a completely

undissociated HNO_3 molecule. As already mentioned above, in the industrial processes of separation, the acid concentration can be high enough to provide significant concentration of undissociated HNO_3 molecules besides oxonium cations. Therefore, the third model is also relevant for the studied cases.

2.2 Computational settings

The DFT simulations of the ligands mentioned in section 2.1 are done by DMol^3 and Gaussian09 programs and the CC calculations are performed by Orca code. First, the conformation analysis based on the lowest energy is performed. Subsequently, the electronic structures are calculated and their properties are studied. In particular, the following properties are investigated: HOMO and LUMO orbitals, Fukui functions, Fukui charges, partial atomic charges, bond orders and electrostatic potential. Transition states are determined and energy diagrams are calculated for the reaction mechanism based on the hydrogen abstraction (section 2.1.1).

2.2.1 Conformation analysis settings

The DFT simulations are done on the conformation of a molecule with the lowest energy. Such conformation is also the most probable in time. The molecular structures of the studied ligands are flexible and have numerous conformers due to many single bonds.

The energy barriers in rotation of single bonds in organic molecules are comparable to the thermal energy. That means that the studied ligands easily change torsion angles between local minimums of those angles at room temperature. Multiple bonds are not capable of the similar behaviour.

Conformation analysis of ligands with acid model

Initial conformations are used from previous works [5, 6] and presented models of the acid influence in section 2.1.2 are applied. The previous knowledge of the ligands is used to reduce the number of calculations. H^+ and H_3O^+ cations are placed in the vicinity of the atoms with a negative partial charge. This information was gained in the previous work [5]. The molecule of the undissociated nitric acid is placed in several surrounding positions of the ligands.

For each model of the acid effect, eight possible initial geometries are generated. The geometry optimization is then performed on those geometries in the Gaussian09 program [73] with following settings: 6–31G(d,p) basis set [83, 84], PCM solvent model [48, 49, 85] with water used as the solvent, GD3BJ dispersion correction [24, 25] (section 1.2.4) and B3LYP exchange and correlation functional [22].

Conformation analysis for reaction calculations

Conformation analysis for reaction calculations is done with CREST utility [86] of xTB Semiempirical Extended Tight–Binding Program Package [87–89]. This software generates the thermally accessible ensemble of minimum-energy structures generally consisting of conformers as well as rotamers using a combination of molecular dynamics and quantum mechanical tight binding approximation. [90].

Further optimization of the conformations with the lowest energy gained by CREST utility of xTB is done with the following settings: 6–311G++(2d,d,p) [91, 92] and Def2TZVP [33, 34] basis sets, PCM solvent model [48, 49, 85] with water as a solvent, GD3BJ dispersion correction [24, 25] (section 1.2.4) and B3LYP exchange and correlation functional [22].

2.2.2 Settings in Gaussian

Gaussian09 code [73] is used for the geometric optimization and HOMO/LUMO calculations. Wiberg bond indices and Natural population analysis are calculated with Gaussian09 in combination with NBO 6.0 software [93] with the following settings: 6–31G(d,p) basis set [83, 84], PCM solvent model [48, 49, 85] with water as the solvent, GD3BJ dispersion correction [24, 25] (section 1.2.4) and B3LYP exchange and correlation functional [22].

Gaussian09 code is also used for searching transition states of the degradation reaction mechanism initiated by the hydrogen abstraction (section 2.1.1) using QST2, QST3 [51, 52] and TS [53] algorithm selections. The following settings are used for searching the transition states: 6–311++G(2d,d,p) [91, 92] and Def2TZVP [33, 34] basis sets, PCM solvent model [48, 49, 85] with water as the solvent, GD3BJ dispersion correction [24, 25] (section 1.2.4) and B3LYP exchange and correlation functional [22]. Furthermore, energy of reactants, intermediates and products are determined by Gaussian09 code with the above mentioned settings using the thermochemistry routines implemented in Gaussian09 code [94].

2.2.3 Settings in Orca

CC calculations [38–44] (section 1.3) are done by Orca software [74, 75] for single–point calculations of energy of reactants, transition states, intermediates and products on geometries gained by DFT calculations using Gaussian09. Following settings is used: DLPNO–CCSD(T) level of theory, Def2TZVP [33, 34] basis set and RIJ-COSX approximation (RI–J for Coulomb integrals and COSX numerical integration for HF exchange) [95–97]. Thermochemistry corrections are added from the Gaussian09 DFT calculations.

2.2.4 Settings in DMol^3

Material studio DMol^3 [29, 30] module is used to determine the subsequent properties of the electronic structure relevant for the stability study. These attributes are

Fukui functions, Fukui charges, Mulliken population analysis, Hirshfeld population analysis, partial charges fitted from the electrostatic potential, bond orders based on Mulliken and Mayer theory and the electrostatic potential with the following settings: DNP basis set [29], COSMO solvent model [46, 47], GD2 dispersion correction [26, 27] (section 1.2.4) and B3LYP correlation functional [22].

2.2.5 Notation of atoms

Atom indices are shown in figure 2.3. Ligands TMDGA, TEDGA and Me_2–TEDGA are symmetrical, only R^2 and R^4 chains are different (one is a hydrogen atom and the other one is a methyl group) in Me–TEDGA. Because of that, properties of the electron density assigned to individual atoms, are averaged for the equivalent atoms. For Me–TEDGA, only the carbons $C^{(4)}$ and $C^{(5)}$) are considered as non-equivalent. For example, only one value of the partial charge is stated for amide carbons $C^{(2)}$ for easier interpretation.

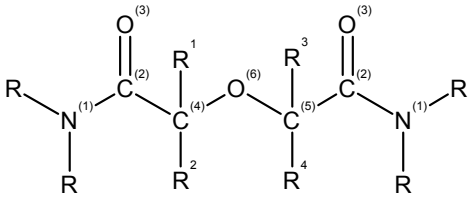

TMDGA: $R = CH_3$, $R_1 = H$, $R_2 = H$, $R_3 = H$, $R_4 = H$,
TEDGA: $R = C_2H_5$, $R_1 = H$, $R_2 = H$, $R_3 = H$, $R_4 = H$,
Me-TEDGA: $R = C_2H_5$, $R_1 = H$, $R_2 = CH_3$, $R_3 = H$, $R_4 = H$,
Me_2-TEDGA: $R = C_2H_5$, $R_1 = H$, $R_2 = CH_3$, $R_3 = H$, $R_4 = CH_3$,

Figure 2.3 General structure of the studied DGAs with atom indices

2.3 Results and discussion

2.3.1 Results of the conformation analysis

Conformation analysis of ligands with acid models

Initial geometries are generated from the ground state geometries of the ligands from previous works, together with the specific particle representing the nitric acid (mentioned in section 2.1.2). For each acid model and each ligand, eight input geometries were created .

In the case of the H_3O^+ model, the influence of higher symmetry occurs for TMDGA, TEDGA and Me–TEDGA. The geometric optimization converges to a state that is visually similar to the planar symmetry. This effect can be seen in figure 2.4 (a). This causes lowering of the total energy of those ligands. For Me_2–TEDGA, this

effect is not detected (figure 2.4 (b)), nor are similar effects observed for another models of the acid influence.

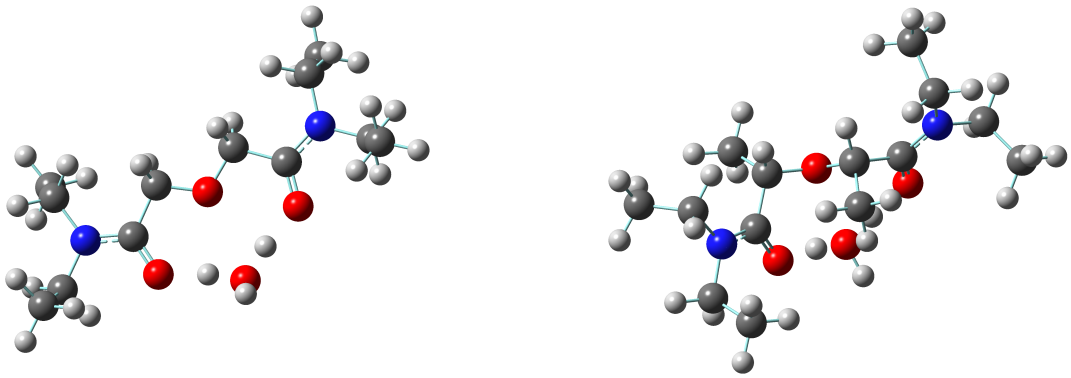

(a) TEDGA (b) Me_2–TEDGA

Figure 2.4 The lowest energy geometries with H_3O^+ model of the acid influence for: (a) TEDGA and (b) Me_2–TEDGA; (settings: Gaussian09, 6-31G(d,p), B3LYP, PCM, GD3BJ)

Hydrogen bonds are observed in the case of the H^+ acid model for all ligands. In the cases of TMDGA, TEDGA and Me_2–TEDGA the hydrogen bond is located between the H^+ cation bonded to one of the carbonyl oxygen and the ether oxygen, see figure 2.5 (a). For TEDGA, length of this hydrogen bond is 1.899 Å. For Me–TEDGA the H^+ cation is bonded to one of the amide nitrogen, consequently two hydrogen bonds are observed. The first one is between the H^+ and the ether oxygen (length 2.279 Å). The other one is between the H^+ and the carbonyl oxygen attached to the other amide group than the H^+ cation (length 1.589 Å), figure 2.5 (b).

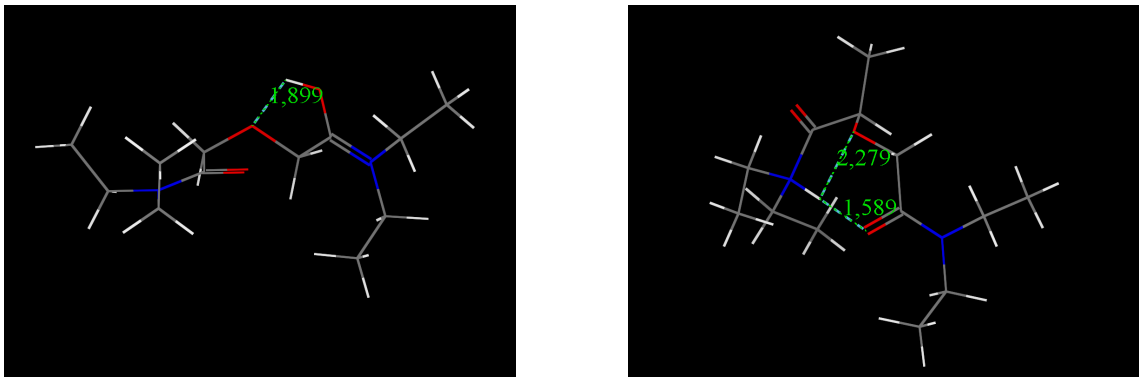

(a) (b)

Figure 2.5 The lowest energy geometries with hydrogen bonds in the case of the H^+ model of the acid influence for: (b) TEDGA and (d) Me_2–TEDGA

The HNO_3 molecule is bonded to the carbonyl oxygen using the hydrogen atom of the nitric acid molecule, see figure 2.6. Another binding locations of the nitric acid molecule are not observed.

Final geometries of the studied ligands and the acid influence models that have the lowest total energy are used in further calculations of the electron density properties.

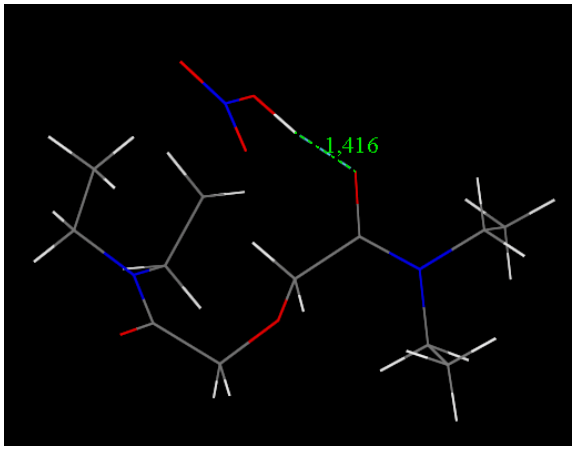

Figure 2.6 The lowest energy geometries with hydrogen bonds in the case of the HNO_3 model of the acid influence for TEDGA

Conformation analysis for reaction calculations

Results of the CREST calculations are in table 2.1 for reactants, in table 2.2 for intermediates and in table 2.3 for products. Only conformers that are easily thermally accessible (with the difference of total energy lower than 3 kcal from the minimal energy value) are considered. For simplicity, only conformers with the lowest energy are used in further calculations.

As expected, TMDGA has the lowest number of unique conformers (5 for a reactant and 2 for an intermediate). The lowest conformer has 95.21% population for the reactant and 98.56% for the intermediate.

Table 2.1 Results of the conformation analysis for reactants of selected ligands done with CREST utility of xTB software, NC – number of unique conformers with energy up to 3 kcal above the lowest energy geometry, PC – population of the lowest energy conformer in %, reaction scheme given in figure 2.12

molecule	NC	PC
TMDGA	5	95.21
TEDGA	80	24.87
Me–TEDGA reaction I	77	38.14
Me–TEDGA reaction II	equal to reaction I	equal to reaction I
Me_2–TEDGA	56	51.93

TEDGA has the highest number of conformers (80) for reactant. Many of these conformers are rotations on the alkyl side chains. This results in low population of the lowest conformer, only 24.87%. For the intermediate, the number of conformers is 25 and population of the lowest conformer is 14.37%. Similar numbers occurs for the Me–TEDGA and reaction I (figure 2.12 (b)) intermediate (24 conformers and 21.82% population of the lowest energy one). This suggests that the intermediate for Me–TEDGA I is similar to the one for TEDGA.

For Me_2–TEDGA, the number of conformers is 56 and population for the reactant is 51.93%. Number of conformers for the intermediate is 45 and population of the lowest energy one is 30.22%. The intermediate for Me–TEDGA reaction II (2.12 (c)) has similar numbers as the Me_2–TEDGA intermediate (48 conformers and 30.81% population of the lowest energy conformer).

For products of all ligands, the number of unique conformers rapidly dropped. This is caused by the planarity of carbonyl group that is presented in both products. Subsequently, populations of the lowest energy conformers are relatively high (table 2.3).

Table 2.2 Results of the conformation analysis for intermediates of selected ligands done with CREST utility of xTB software, NC – number of unique conformers with energy up to 3 kcal above the lowest energy geometry, PC – population of the lowest energy conformer in %, reaction scheme are in figure 2.12

molecule	NC	PC
TMDGA	2	98.56
TEDGA	25	14.37
Me–TEDGA reaction I	24	21.82
Me–TEDGA reaction II	48	30.81
Me_2–TEDGA	45	30.22

Table 2.3 Results of the conformation analysis for products of selected ligands done with CREST utility of xTB software, NC – number of unique conformers with energy up to 3 kcal above the lowest energy geometry, PC – population of the lowest energy conformer in %, reaction scheme are in figure 2.12

molecule	product	NC	PC
TMDGA	product 1	2	99.34
	product 2	2	96.83
TEDGA	product 1	3	50.77
	product 2	9	30.31
Me–TEDGA reaction I	product 1	2	63.20
	product 2	8	29.82
Me–TEDGA reaction II	product 1	4	59.28
	product 2	6	34.33
Me_2–TEDGA	product 1	2	63.33
	product 2	6	34.59

2.3.2 Orbitals

The HOMO–LUMO gap is related to chemical hardness and kinetic stability of a molecule. A hard molecule has a large gap and a soft one has a small gap. Generally, lower HOMO–LUMO gap implies lower excitation energies, molecules with a small gap are more reactive than the ones with a larger gap [69, 70] (more in section 1.7.4).

The previous stability study [5] estimated HOMO–LUMO gap of the DGAs and also the energy gap between the radical OH• LUMO and the HOMO of the DGAs (related to the case of electron transfer). The same procedure is here repeated for the models of the acid influence, with the indicated acid representations added to DGAs in place of structures the gap is calculated for.

In the previous work [5], the trend of increasing HOMO–LUMO gap value was observed for TEDGA and methylated ligands, but the value of the gap for TMDGA was inconsistent with this trend. The previous and the recent results are summarized in table 2.4.

Table 2.4 HOMO–LUMO gap for studied Diglycolamides in $kJ \cdot mol^{-1}$ (settings: Gaussian, B3LYP, 6-31G(d,p), GD3BJ, NBO, PCM)

acid model	TMDGA	TEDGA	Me–TEDGA	Me_2–TEDGA
no acid considered [5]	637	629	640	646
H^+	514	566	515	501
H_3O^+	680	672	670	670
HNO_3	483	483	481	420

Inclusion of the acid influence led to the disappearance of the above mentioned trend. Incorporation of H_3O^+ and HNO_3 acid models resulted in the trend of the decreasing size of the gap from TMDGA to Me_2–TEDGA. If we assume the hypothesis that a higher HOMO–LUMO gap is related to higher stability, this disagrees with the experimentally determined stability. The H^+ model causes the trend of the increasing size of the gap for TMDGA and TEDGA, but the values for methylated derivatives of TEDGA are lower than for TEDGA, indicating a decrease of the energy gap.

For an investigation of the degradation based on the electron transfer, $HOMO_{(DGA)}$–$LUMO_{(\bullet OH\ radical)}$ gap is calculated. In the previous work, the decrease of the energy gap was recognized suggesting the trend of the decreasing stability with increasing molecular weight. This decrease is in contradiction with the experimentally observed stability trend [5]. Results are shown in table 2.5.

In cases of H_3O^+ and HNO_3 models, similar trend is observed, with the exception of Me_2–TEDGA and the H_3O^+ acid model. Values of the energy gap for the H^+ acid model indicate the trend of the stability compatible with the experimental results for TMDGA, TEDGA and Me–TEDGA, but Me_2–TEDGA is breaking this trend.

These results can not be reliably interpreted due to the above mentioned inconsistencies and the disagreement with the experimentally observed stability trend (TMDGA < TEDGA < Me–TEDGA < Me_2–TEDGA).

Table 2.5 $HOMO_{(DGA)}$–$LUMO_{(\bullet OH\ radical)}$ gap for studied DGAs in $kJ \cdot mol^{-1}$ (settings: Gaussian, B3LYP, 6-31G(d,p), GD3BJ, NBO, PCM)

acid model	TMDGA	TEDGA	Me–TEDGA	Me_2–TEDGA
no acid considered	227	226	225	218
H^+	250	264	293	248
H_3O^+	298	296	295	306
HNO_3	231	230	228	220

2.3.3 Fukui functions and Fukui charges

In the case of the first degradation mechanism, which is based on the abstraction of the hydrogen atom on the ether group (see section 2.1.1 for detailed information), the radical Fukui function and the radical Fukui charges are calculated and examined. Values of the Fukui function are mapped on the isosurface of the electron density with a value 0,017 $e \cdot Å^{-3}$. Fukui charges are a way of assigning volume Fukui function values to individual atoms.

In addition, the electrophilic Fukui charges and the electrophilic Fukui function are determined to study the other possible degradation mechanism beginning with an electron transfer from the DGA to the free radical. As a result, either the C–O ether bond or the C–N amide bond breaks down, as discussed in section 2.1.1.

The condensed Fukui charges listed below are based on the Hirshfeld population analysis; Fukui charges based on Mulliken population analysis can be found in appendix A. This procedure is done, because the Hirshfeld population analysis is generally considered to be a more relevant method for a calculation of partial charges calculation than the Mulliken population analysis. Also, the Hirshfeld population analysis is less basis set sensitive comparing to the Mulliken method. Fukui charges are averaged and their labeling is based on atom indices summarized in figure 2.3 in section 2.2.5.

Radical Fukui function – hydrogen abstraction

The radical Fukui function describes possible locations, where a reaction of a radical and the molecule can be initiated. In the case of the lipophilic DGAs [7], the radical Fukui function has proven to be a good property for identifying sites susceptible to a reaction with radicals.

Maximum values of the volumetric radical Fukui function close to the hydrogen atoms bonded to the ether group (red circles in figure 2.8 for TEDGA) are identified for all acid representations and compared with the previous results. The observed trend in the previous work was consistent with the experimentally determined stability, the previous results are included in table 2.6 [5, 6]. In all cases, the trend of decreasing reactivity with increasing molecular weight is enhanced in comparison with the models where the acid influence was neglected (figure 2.7). This confirms the experimentally determined stability of studied ligands.

In all cases, the maximum of the radical Fukui function close to the amide group

is also evident (white circles in figure 2.8) in concert with the former results [5, 6]. Wilden et al. [3] suggests reaction with OH• radical at this site, but this possible reaction mechanism is not investigated in this thesis.

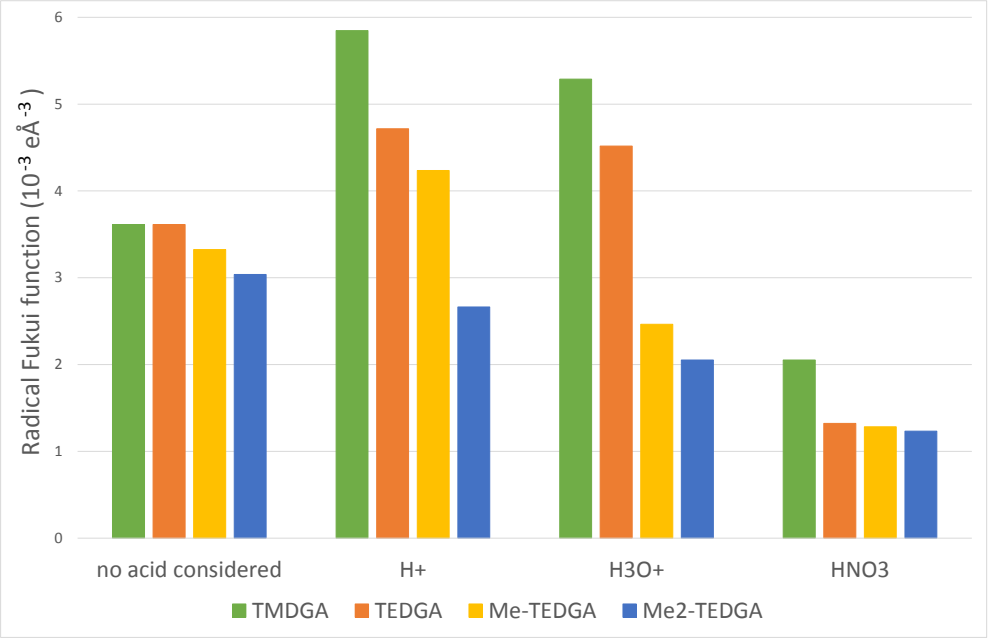

Figure 2.7 The radical Fukui function maximum (10^{-3} e·Å^{-3}) of the studied DGA derivatives and models from table 2.6; maximum marked by red circle in figure 2.8 (a) – (d); (settings: DMol^3, DNP, B3LYP, GD2, COSMO)

Table 2.6 Values of the radical Fukui function in 10^{-3} e·Å^{-3}, maximum mapped on the isosurface (0.017 e·Å^{-3}) close to the ether–neighbouring hydrogen atoms; (settings: DMol^3, DNP, B3LYP, GD2, COSMO)

acid model	TMDGA	TEDGA	Me–TEDGA	Me_2–TEDGA
no acid considered	3.613	3.613	3.325	3.038
H^+	5.847	4.716	4.235	2.663
H_3O^+	5.287	4.516	2.463	2.053
HNO_3	2.053	1.322	1.282	1.232

Radical Fukui charges – hydrogen abstraction

Fukui charges are the values of volumetric Fukui functions condensed on the individual atoms. They provide more easily interpretable information about the reactivity of the molecule than plain Fukui functions.

High values of the radical Fukui charges on $N^{(1)}$, $C^{(2)}$ and $O^{(3)}$ atoms correspond to the maximum of the radical Fukui function on the amide group (section

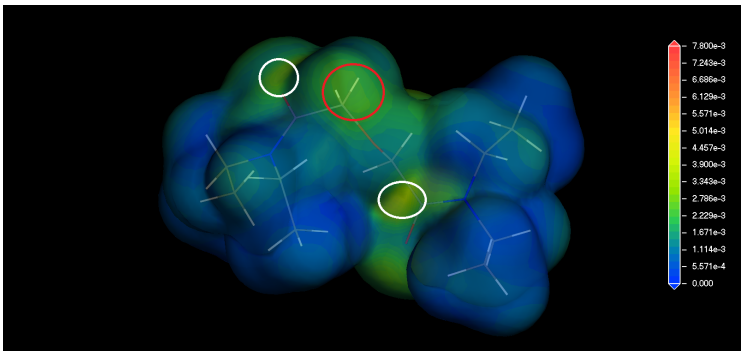

(a) without acid model

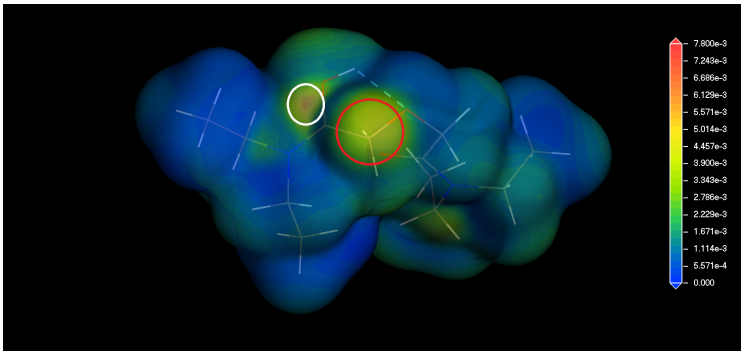

(b) H^+ model

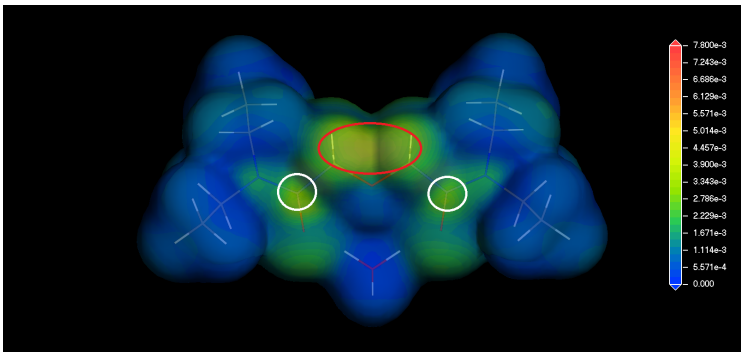

(c) H_3O^+ model

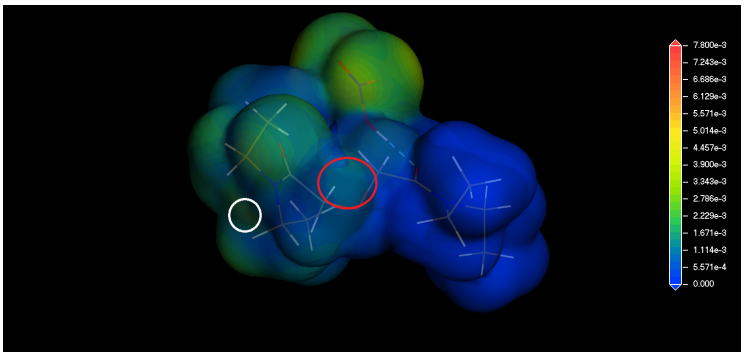

(d) HNO_3 model

Figure 2.8 Radical Fukui function mapped on the isosurface of the electron density with the value 0.017 e·Å^{-3} for TEDGA and all acid models; red circle indicates the main maximum in vicinity of the ether group, white circles indicate maxima on the amide groups;(settings: DMol^3, DNP, B3LYP, GD2, COSMO)

2.3.3). These Fukui charges did not modify significantly by the addition of any acid representations except for the HNO_3 acid model, which caused significant drop of the charges. The reaction mechanism initiated in this area is unknown. Degradation products of DGAs corresponding to the decay reaction in the amide group region were identified experimentally after the sample irradiation. However, they were also present in non–irradiated samples. For this reason, these products are probably residues after the synthesis of the molecules [3].

The most important area in the study of DGA radiolysis is the ether group. The radical Fukui charges on the oxygen $O^{(6)}$ did not indicate any trend in previous works [5, 6]. However, after the acid representation is included, Fukui charges are decreasing with increasing molecular weight. In previous works [5, 6], the noticeable decrease of radical Fukui charges on $C^{(4)}$ and on $C^{(5)}$ carbons indicated increasing stability with increasing molecular weight. This phenomenon remained unchanged after including any of acid representations.

The radical Fukui charges on hydrogen atoms (tables 2.7, 2.8, 2.9 and 2.10) at positions R^1 – R^4 (figure 2.3) adjacent to $C^{(4)}$ and $C^{(5)}$ atoms are averaged. Only when there is a methyl group at the given position, the Fukui charges are not indicated. Since the ether group is the predicted site of the initiation of the reaction with the radical, these hydrogen atoms are those that are abstracted by the incoming radical. Charge values display a downward trend that implies the correlation with the experimentally determined stability, i.e., they correspond to TMDGA > TEDGA > Me–TEDGA > Me_2–TEDGA reactivity trend.

Table 2.7 Radical Fukui charges based on Hirshfeld population analysis without an acid model; (settings: $DMol^3$, DNP, B3LYP, GD2, COSMO), atom labels given in figure 2.3

atom	atom label	TMDGA	TEDGA	Me–TEDGA	Me_2–TEDGA
N	(1)	0.062	0.057	0.057	0.054
C	(2)	0.067	0.063	0.064	0.064
O	(3)	0.114	0.111	0.113	0.111
C	(4)	0.030	0.030	0.021	0.022
C	(5)	eq. (4)	eq. (4)	0.029	eq. (4)
O	(6)	0.037	0.033	0.033	0.036
H	R^1	0.026	0.025	0.023	0.020
H	R^2	eq. R^1	eq. R^1	–	–
H	R^3	eq. R^1	eq. R^1	eq. R^1	eq. R^1
H	R^4	eq. R^1	eq. R^1	eq. R^1	–
H	average of all H	0.021	0.014	0.013	0.012

Considering the abstraction of the hydrogen adjacent to the ether group as the initiation of the degradation reaction, it must not be forgotten that in the case of methylated ligands the number of possible reaction centres (a hydrogen adjacent to the ether group at positions R^1 – R^4) is lower. TMDGA and TEDGA have four of these hydrogens, but only three hydrogen of this type are present in Me–TEDGA, and further only two hydrogens are in Me_2–TEDGA. This correspondingly reduces the probability of the abstraction of a hydrogen for methylated ligands in accordance with the experimentally observed trend of the stability.

Table 2.8 Radical Fukui charges based on Hirshfeld population analysis with the H^+ acid model; (settings: $DMol^3$, DNP, B3LYP, GD2, COSMO), atom labels given in figure 2.3

atom	atom label	TMDGA	TEDGA	Me–TEDGA	Me_2–TEDGA
N	(1)	0.096	0.072	0.049	0.070
C	(2)	0.071	0.068	0.076	0.065
O	(3)	0.097	0.074	0.108	0.088
C	(4)	0.020	0.019	0.013	0.009
C	(5)	eq. (4)	eq. (4)	0.018	eq. (4)
O	(6)	0.023	0.021	0.012	0.012
H	R^1	0.025	0.024	0.022	0.014
H	R^2	eq. R^1	eq. R^1	–	–
H	R^3	eq. R^1	eq. R^1	eq. R^1	eq. R^1
H	R^4	eq. R^1	eq. R^1	eq. R^1	–
H	average of all H	0.022	0.016	0.013	0.013

Table 2.9 Radical Fukui charges based on Hirshfeld population analysis with the H_3O^+ acid model; (settings: $DMol^3$, DNP, B3LYP, GD2, COSMO), atom labels given in figure 2.3

atom	atom label	TMDGA	TEDGA	Me–TEDGA	Me_2–TEDGA
N	(1)	0.065	0.061	0.062	0.060
C	(2)	0.072	0.070	0.068	0.064
O	(3)	0.079	0.078	0.078	0.083
C	(4)	0.025	0.025	0.018	0.015
C	(5)	eq. (4)	eq. (4)	0.020	eq. (4)
O	(6)	0.033	0.032	0.029	0.022
H	R^1	0.031	0.029	0.019	0.015
H	R^2	eq. R^1	eq. R^1	–	–
H	R^3	eq. R^1	eq. R^1	eq. R^1	eq. R^1
H	R^4	eq. R^1	eq. R^1	eq. R^1	–
H	average of all H	0.020	0.014	0.013	0.013

Table 2.10 Radical Fukui charges based on Hirshfeld population analysis with the HNO_3 acid model; (settings: $DMol^3$, DNP, B3LYP, GD2, COSMO), atom labels given in figure 2.3

atom	atom label	TMDGA	TEDGA	Me–TEDGA	Me_2–TEDGA
N	(1)	0.038	0.045	0.044	0.065
C	(2)	0.019	0.018	0.016	0.018
O	(3)	0.067	0.058	0.058	0.058
C	(4)	0.009	0.006	0.002	0.007
C	(5)	eq. (4)	eq. (4)	0.006	eq. (4)
O	(6)	0.022	0.007	0.004	0.007
H	R^1	0.011	0.008	0.006	0.011
H	R^2	eq. R^1	eq. R^1	–	–
H	R^3	eq. R^1	eq. R^1	eq. R^1	eq. R^1
H	R^4	eq. R^1	eq. R^1	eq. R^1	–
H	average of all H	0.012	0.009	0.008	0.008

For TMDGA (as an exception among the studied ligands), products that correspond to the rupture of the C–O ether bond were not observed during the experiment [3]. The authors suggested that the abstraction of the hydrogen atom does not occur at the positions R^1 – R^4, but at the R chain. For this reason, a way to verify this behaviour was proposed in the previous work [5]. It is based on the determination of the average value of the radical Fukui charges on all hydrogen atoms in the molecule. Without the acid representation, this value for TMDGA is 0.021, which is very close to the average value at R^1 – R^4. It follows that the probability of the hydrogen abstraction from the ether group is comparable to the abstraction from one of the CH_3 group. For other molecules and for the approach without any acid model (previous works [5, 6]), the values of the radical Fukui charges at positions R^1 – R^4 are significantly greater (0.025 for TEDGA) than is the average value of all hydrogen atoms (0.014 for TEDGA). From this we can conclude that the probability of the hydrogen abstraction from the ether group is significantly higher than from the side chains in case of TEDGA and its methylated derivatives.

A similar results are generated for TMDGA by the H^+ acid model, with the Fukui charges at positions R^1 – R^4 even closer to the average value of all hydrogen atoms. Also, the averaged charge for Me_2–TEDGA (0.013) is very close to the value of the hydrogen at positions R^1 – R^4 (0.014) for this acid representation. This suggests that Me_2–TEDGA could behave as TMDGA (the higher possibility of the hydrogen abstraction at the R chain), but Me_2–TEDGA is more stable than TMDGA due to lower values. However, this behaviour of Me_2–TEDGA was not observed during the experiment [3]. Therefore, it is most likely a deviation caused by the acid model. For the remaining ligands the difference between the average value and the value at positions R^1 – R^4 persists (table 2.8).

For the H_3O^+ acid representation, the small difference between the average value for all hydrogens and the value for hydrogens at positions R^1 – R^4 is not present for TMDGA, but it remains unchanged for Me_2–TEDGA (table 2.9). This suggests that Me_2–TEDGA could behave as TMDGA during the experiment [3] (the higher possibility of the hydrogen abstraction at the R chain). Similarly as for the H^+ acid

model, this is most likely a deviation caused by the acid model.

Finally, the HNO_3 acid model causes that the average values of all hydrogen atoms and the values for hydrogens at positions R^1 – R^4 are almost the same for all ligands (table 2.10).

In general, the inclusion of the acid influence leads to the reduction of the radical Fukui charges mainly on the ether group. Although some qualitative changes are observed, no trend different from those gained in the previous works [5, 6] is found to be conclusive. The H^+ acid model supports the experimentally determined trend of the stability and even increases the differences among the ligands. The H_3O^+ acid representation partially correlates with this trend. However, the HNO_3 acid model does not reliably support the trend.

Electrophilic Fukui function – electron transfer

Results of the electrophilic Fukui function are not discussed in this work due to two reasons. Firstly, the results of the electrophilic Fukui function do not seem to be reliable. No significant maxima or minima are observed in the vicinity of the amide groups. Furthermore, the ligands are polarized (figure 2.9 (b)). The magnitude of the polarization depends on the acid model. For the H^+ and the H_3O^+ acid models, the total charge of the system is $+1$ in contrary to the cases without any acid representation and the HNO_3 acid model, where the systems are neutral. Therefore, these different approaches should not be compared to each other.

The other reason is that electrophilic Fukui functions are not comparable for different acid representations. This is caused by differences in scales of maximal and minimal values mapped on the isosurface of the electron density for the ligands in the case of one acid representation. Example of the described behaviour is presented for TEDGA in figure 2.9, where it can be seen that only for the H^+ acid model, the extremes of the electrophilic Fukui function can be easily identified. For the purposes of analysis, the colours are scaled to the same values across the different acid models. This was also observed in the previous work [5].

Electrophilic Fukui charges – electron transfer

The second reaction mechanism mentioned in section 2.1.1 suggests the removal of an electron from the DGA by a radical, presumably in the vicinity of one of the amide groups [3]. The fact that this phenomenon is more likely to occur in the amide group was supported in the previous works [5, 6] by the electrophilic Fukui charges on the amide group. Their values on the $N^{(1)}$, $C^{(2)}$, and $O^{(3)}$ atoms were higher in comparison to the values on the ether group. Nevertheless, these values correlated with experimental degradation only partially. The Fukui charges on $N^{(1)}$ and $O^{(3)}$ atoms were lower for TMDGA than for TEDGA and its methylated derivatives.

Also in the previous work [5] the trend of decreasing electrophilic Fukui charges is observed for TEDGA, Me–TEDGA and Me_2–TEDGA. However, in the case of TMDGA, the values of the electrophilic Fukui charges of the amide group are lower

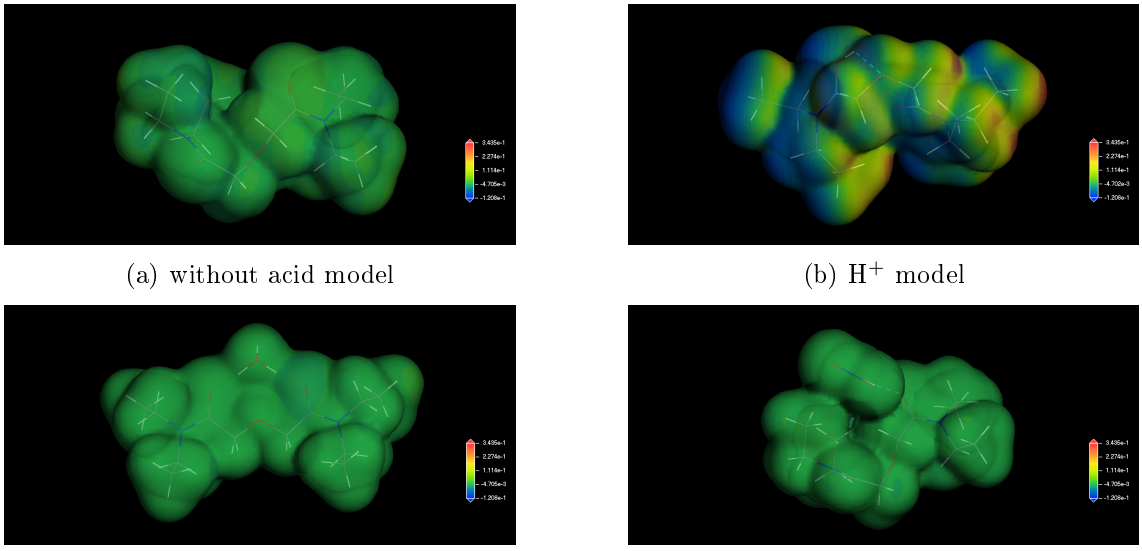

(a) without acid model

(b) H^+ model

(c) H_3O^+ model

(d) HNO_3 model

Figure 2.9 Electrophilic Fukui function mapped on an isosurface of the electron density with a value 0.017 e·Å^{-3} for TEDGA and all acid models; (settings: DMol^3, DNP, B3LYP, GD2, COSMO)

than for TEDGA. On the other hand, the values on the ether group are higher, where the charges for TEDGA, Me–TEDGA and Me_2–TEDGA do not differ significantly. This illustrates the reported different behaviour of TMDGA during the experiment [3].

The model of the acid influence has considerable impact on the Fukui charges of the amide group. Differences of the charges of the $N^{(1)}$ atom between TMDGA and remaining DGAs are reduced or disappear for H^+ and H_3O^+ acid models, but remain unchanged for the HNO_3 acid model. Higher values of the Fukui charges on the carbons $C^{(2)}$ for TMDGA compared to remaining DGAs diminish or vanish when including the acid influence.

The most remarkable influence of the acid model is seen on the Fukui charges of the ether group ($C^{(4)}$, $C^{(5)}$, $O^{(6)}$ atoms and H at R^1 – R^4 positions), where the Fukui charges do not differ significantly for the acid–free model. After the inclusion of the acid, a noticeable decrease is evident in Fukui charges of the $C^{(4)}$, $C^{(5)}$, $O^{(6)}$ atoms and H at R^1 – R^4 positions for all acid models, with only a few exceptions, such as the $O^{(6)}$ oxygen and the H_3O^+ acid model. The decreasing trends are in agreement with the experimentally observed trend of the stability for all acid models.

The average electrophilic Fukui charges on hydrogen atoms are comparable to values at R^1 – R^4 positions for all acid representations as in the previous work without a consideration of the acid influence. Thus, the difference in reactivity of molecules at these sites cannot be deduced from these results.

Table 2.11 Electrophilic Fukui charges based on Hirshfeld population analysis without an acid model; (settings: DMol^3, DNP, B3LYP, GD2, COSMO), atom labels given in figure 2.3

atom	atom label	TMDGA	TEDGA	Me–TEDGA	Me_2–TEDGA
N	(1)	0.062	0.079	0.075	0.069
C	(2)	0.067	0.035	0.035	0.033
O	(3)	0.114	0.121	0.122	0.119
C	(4)	0.030	0.014	0.012	0.014
C	(5)	eq. (4)	eq. (4)	0.011	eq. (4)
O	(6)	0.037	0.025	0.025	0.044
H	R^1	0.026	0.017	0.016	0.017
H	R^2	eq. R^1	eq. R^1	–	–
H	R^3	eq. R^1	eq. R^1	eq. R^1	eq. R^1
H	R^4	eq. R^1	eq. R^1	eq. R^1	–
H	average of all H	0.022	0.015	0.014	0.013

Table 2.12 Electrophilic Fukui charges based on Hirshfeld population analysis with the H^+ acid model; (settings: DMol^3, DNP, B3LYP, GD2, COSMO), atom labels given in figure 2.3

atom	atom label	TMDGA	TEDGA	Me–TEDGA	Me_2–TEDGA
N	(1)	0.086	0.089	0.085	0.086
C	(2)	0.041	0.031	0.035	0.031
O	(3)	0.117	0.090	0.087	0.111
C	(4)	0.016	0.012	0.002	0.004
C	(5)	eq. (4)	eq. (4)	0.017	eq. (4)
O	(6)	0.033	0.023	0.012	0.007
H	R^1	0.018	0.015	0.016	0.009
H	R^2	eq. R^1	eq. R^1	–	–
H	R^3	eq. R^1	eq. R^1	eq. R^1	eq. R^1
H	R^4	eq. R^1	eq. R^1	eq. R^1	–
H	average of all H	0.020	0.015	0.015	0.013

Table 2.13 Electrophilic Fukui charges based on Hirshfeld population analysis with the H_3O^+ acid model; (settings: DMol^3, DNP, B3LYP, GD2, COSMO), atom labels given in figure 2.3

atom	atom label	TMDGA	TEDGA	Me–TEDGA	Me_2–TEDGA
N	(1)	0.082	0.078	0.079	0.074
C	(2)	0.030	0.032	0.034	0.025
O	(3)	0.073	0.079	0.081	0.062
C	(4)	0.017	0.019	0.008	0.009
C	(5)	eq. (4)	eq. (4)	0.019	eq. (4)
O	(6)	0.065	0.052	0.033	0.026
H	R^1	0.023	0.024	0.018	0.015
H	R^2	eq. R^1	eq. R^1	–	–
H	R^3	eq. R^1	eq. R^1	eq. R^1	eq. R^1
H	R^4	eq. R^1	eq. R^1	eq. R^1	–
H	average of all H	0.021	0.015	0.013	0.014

Table 2.14 Electrophilic Fukui charges based on Hirshfeld population analysis with the HNO_3 acid model; (settings: DMol^3, DNP, B3LYP, GD2, COSMO), atom labels given in figure 2.3

atom	atom label	TMDGA	TEDGA	Me–TEDGA	Me_2–TEDGA
N	(1)	0.067	0.087	0.086	0.082
C	(2)	0.035	0.035	0.031	0.029
O	(3)	0.127	0.111	0.112	0.108
C	(4)	0.017	0.010	0.010	0.006
C	(5)	eq. (4)	eq. (4)	0.002	eq. (4)
O	(6)	0.044	0.013	0.006	0.021
H	R^1	0.020	0.013	0.010	0.015
H	R^2	eq. R^1	eq. R^1	–	–
H	R^3	eq. R^1	eq. R^1	eq. R^1	eq. R^1
H	R^4	eq. R^1	eq. R^1	eq. R^1	–
H	average of all H	0.020	0.015	0.014	0.013

2.3.4 Partial charges

Calculations of partial charges was done by the following methods: Mulliken population analysis, Hirshfeld population analysis, fitting to the electrostatic potential and Natural population analysis. Charges of the equivalent atoms are averaged and their labeling is based on atom indices in figure 2.3 in section 2.2.5. Natural population analysis is considered to be the most reliable method. For this reason, only this method is discussed here. Results of remaining methods are summarized in appendix B. Results of the Mulliken population analysis are in agreement with those obtained by the Natural population analysis, in contrast to the results of the Hirshfeld method. In the case of partial charges determined by the fitting to electrostatic potential, weaknesses of this method became apparent.

In general, changes in the evolution of charges on atoms can be attributed to the choice of the acid model. Especially, the site of attachment of the acid model molecule is important (section 2.3.1), but also the total charge of the system is crucial. The total charge is zero for the HNO_3 acid model and $+1$ for H^+ and H_3O^+ models. For example, this can be seen in the case of the H^+ acid model (table 2.16) on the $N^{(1)}$ or $C^{(2)}$ atom. For Me–TEDGA, where the H^+ cation is bonded to a different location of the ligand than in the case of the remaining ligands (section 2.3.1), the partial charge on the $N^{(1)}$ atom is -0.495 for Me–TEDGA, but it is -0.415 e for TEDGA or -0.410 e for Me_2–TEDGA. The H^+ model shows the greatest differences from the situation without the acid influence. The other two models are then in agreement with the acid–free situation.

The increase of the charge on the $O^{(6)}$ oxygen accompanying introduction of methyl groups on the $C^{(4)}$ and $C^{(5)}$ atoms was observed in the previous work [5]. The methyl group provides the electron density to the surrounding atoms. Therefore, bonding of the methyl group on $C^{(4)}$ and $C^{(5)}$ atoms (synthesis of Me–TEDGA and Me_2–TEDGA) should protect the ether $O^{(6)}$–$C^{(4)}$ and $O^{(6)}$–$C^{(5)}$ bonds, i.e., these bonds should have higher bond order (section 2.3.5). Surprisingly, this does not occur for the studied molecules, but the partial charge on the ether oxygen $O^{(6)}$ increases as a result of methylation (more in section 2.3.5). The same development was observed in the case of TODGA and its derivatives [7]. This phenomenon is not altered by considering the models of the acid influence. A small deviation occurs for TMDGA and the H^+ acid model, where the charge on the oxygen $O^{(6)}$ is -0.601 e, but in the case of TEDGA it is -0.583 e. The trend remains unchanged for TEDGA and its methylated derivatives.

In the previous work [5] the effect of methylation on the partial charges is also present on $C^{(4)}$ and $C^{(5)}$ atoms, where the charge value is shifted in the positive direction. This happens also for all acid models (see any of tables 2.15, 2.16, 2.17 or 2.18). As in the previous work [5], since the chemical nature of these carbon atoms changes, it is not possible to regard these charge differences as an indication of a change in reactivity or other chemical properties.

Table 2.15 Partial charges based on the Natural population analysis without an acid model; (settings: Gaussian, B3LYP, GD3BJ, 6-31G(d,p), NBO, PCM), atom labels given in figure 2.3

atom	atom label	TMDGA	TEDGA	Me–TEDGA	Me_2–TEDGA
N	(1)	−0.455	−0.465	−0.465	−0.464
C	(2)	0.666	0.668	0.672	0.681
O	(3)	−0.673	−0.676	−0.679	−0.682
C	(4)	−0.195	−0.192	0.011	0.016
C	(5)	eq. (4)	eq. (4)	−0.188	eq. (4)
O	(6)	−0.589	−0.588	−0.596	−0.607

Table 2.16 Partial charges based on the Natural population analysis with the H^+ acid model; (settings: Gaussian, B3LYP, GD3BJ, 6-31G(d,p), NBO, PCM), atom labels given in figure 2.3

atom	atom label	TMDGA	TEDGA	Me–TEDGA	Me_2–TEDGA
N	(1)	−0.457	−0.415	−0.495	−0.410
C	(2)	0.687	0.698	0.722	0.683
O	(3)	−0.654	−0.670	−0.601	−0.659
C	(4)	−0.194	−0.190	−0.011	0.009
C	(5)	eq. (4)	eq. (4)	−0.193	eq. (4)
O	(6)	−0.601	−0.583	−0.588	−0.599

Table 2.17 Partial charges based on the Natural population analysis with the H_3O^+ acid model; (settings: Gaussian, B3LYP, GD3BJ, 6-31G(d,p), NBO, PCM), atom labels given in figure 2.3

atom	atom label	TMDGA	TEDGA	Me–TEDGA	Me_2–TEDGA
N	(1)	−0.419	−0.429	−0.428	−0.423
C	(2)	0.711	0.712	0.716	0.707
O	(3)	−0.693	−0.693	−0.695	−0.698
C	(4)	−0.192	−0.188	0.022	0.020
C	(5)	eq. (4)	eq. (4)	−0.187	eq. (4)
O	(6)	−0.578	−0.577	−0.589	−0.593

Table 2.18 Partial charges based on the Natural population analysis with the HNO_3 acid model; (settings: Gaussian, B3LYP, GD3BJ, 6-31G(d,p), NBO, PCM), atom labels given in figure 2.3

atom	atom label	TMDGA	TEDGA	Me–TEDGA	Me_2–TEDGA
N	(1)	−0.435	−0.444	−0.444	−0.465
C	(2)	0.681	0.682	0.687	0.681
O	(3)	−0.683	−0.687	−0.690	−0.678
C	(4)	−0.194	−0.192	0.011	0.013
C	(5)	eq. (4)	eq. (4)	−0.188	eq. (4)
O	(6)	−0.587	−0.586	−0.595	−0.609

2.3.5 Bond orders

Bond orders are a useful tool for investigating of the stability of a molecule, especially how strongly atoms are bonded. The following methods of their calculation are used: Mulliken method, Mayer method and Wiberg bond indices, which are based on the NBO theory (section 1.7.1). This theory is considered to be the most accurate one, and it was also confirmed in the previous work [5]. For these reasons, only Wiberg bond indices are discussed here. Results of the remaining methods can be found in appendix C. Bond orders of equivalent bonds are averaged and the labeling is based on atom indices in figure 2.3 in section 2.2.5. The results without the acid influence model are shown in table 2.19, for the H^+ model in table 2.20, for the H_3O^+ model in table 2.21 and for the HNO_3 model in table 2.22.

Table 2.19 Wiberg bond indices without an acid model; (settings: Gaussian, B3LYP, GD3BJ, 6-31G(d,p), NBO, PCM), atom labels given in figure 2.3

bond	TMDGA	TEDGA	Me–TEDGA	Me_2–TEDGA
$N^{(1)}$–$C^{(2)}$	1.225	1.233	1.235	1.235
$C^{(2)}$–$O^{(3)}$	1.604	1.597	1.593	1.593
$C^{(2)}$–$C^{(4)}$	0.965	0.964	0.954	0.945
$C^{(4)}$–$O^{(6)}$	0.904	0.904	0.889	0.884
$C^{(5)}$–$O^{(6)}$	eq. $C^{(4)}$–$O^{(6)}$	eq. $C^{(4)}$–$O^{(6)}$	0.900	eq. $C^{(4)}$–$O^{(6)}$

Table 2.20 Wiberg bond indices with the H^+ acid model; (settings: Gaussian, B3LYP, GD3BJ, 6-31G(d,p), NBO, PCM), atom labels given in figure 2.3

bond	TMDGA	TEDGA	Me–TEDGA	Me_2–TEDGA
$N^{(1)}$–$C^{(2)}$	1.355	1.368	1.076	1.371
$C^{(2)}$–$O^{(3)}$	1.408	1.372	1.688	1.393
$C^{(2)}$–$C^{(4)}$	0.986	0.982	0.972	0.961
$C^{(4)}$–$O^{(6)}$	0.895	0.908	0.895	0.880
$C^{(5)}$–$O^{(6)}$	eq. $C^{(4)}$–$O^{(6)}$	eq. $C^{(4)}$–$O^{(6)}$	0.913	eq. $C^{(4)}$–$O^{(6)}$

Table 2.21 Wiberg bond indices with the H_3O^+ acid model; (settings: Gaussian, B3LYP, GD3BJ, 6-31G(d,p), NBO, PCM), atom labels given in figure 2.3

bond	TMDGA	TEDGA	Me–TEDGA	Me_2–TEDGA
$N^{(1)}$–$C^{(2)}$	1.322	1.328	1.332	1.339
$C^{(2)}$–$O^{(3)}$	1.446	1.442	1.439	1.427
$C^{(2)}$–$C^{(4)}$	0.982	0.982	0.971	0.958
$C^{(4)}$–$O^{(6)}$	0.913	0.914	0.892	0.895
$C^{(5)}$–$O^{(6)}$	eq. $C^{(4)}$–$O^{(6)}$	eq. $C^{(4)}$–$O^{(6)}$	0.914	eq. $C^{(4)}$–$O^{(6)}$

Bond order of the ether $C^{(4)}$–$O^{(6)}$ or $C^{(5)}$–$O^{(6)}$ bond is the lowest one among the rest of bonds for every acid model as well as without acid model (tables 2.19, 2.20,

Table 2.22 Wiberg bond indices with the HNO_3 acid model; (settings: Gaussian, B3LYP, GD3BJ, 6-31G(d,p), NBO, PCM), atom labels given in figure 2.3

bond	TMDGA	TEDGA	Me–TEDGA	Me_2–TEDGA
$N^{(1)}$–$C^{(2)}$	1.276	1.282	1.285	1.228
$C^{(2)}$–$O^{(3)}$	1.524	1.519	1.515	1.597
$C^{(2)}$–$C^{(4)}$	0.971	0.970	0.964	0.946
$C^{(4)}$–$O^{(6)}$	0.904	0.903	0.880	0.882
$C^{(5)}$–$O^{(6)}$	eq. $C^{(4)}$–$O^{(6)}$	eq. $C^{(4)}$–$O^{(6)}$	0.904	eq. $C^{(4)}$–$O^{(6)}$

2.21 and 2.22). This is also observed for the rest of methods as in the previous work [5] suggesting the ether bond to be the weakest one and to be the location, where the degradation mechanism is initiated. Furthermore, mainly the decreasing trend is observed with increasing molecular weight. This suggests that the ether $C^{(4)}$–$O^{(6)}$ and $C^{(5)}$–$O^{(6)}$ bonds are stronger for TMDGA than for Me_2–TEDGA. However, this is in disagreement with the experimentally observed trend of the stability. Additional electron density provided by methylation is located on the ether carbon $C^{(4)}$ or $C^{(5)}$, see section 2.3.4, but the bond order $C^{(4)}$–$O^{(6)}$ or $C^{(5)}$–$O^{(6)}$ (based on the orbital overlap) does not increase. This was reported also for TODGA and its methylated derivatives [7]. These results seem to be in contradiction with the experiment, but it was shown in [7] that the bond orders alone cannot be used as decisive stability indicators. Only a complete analysis of all computed properties and their collective understanding can be used for their reliable interpretation.

The partial trend of increasing bond orders are observed on the $N^{(1)}$–$C^{(2)}$ bond for all acid models (except the case of Me–TEDGA with the H^+ representation of the acid and Me_2–TEDGA with the HNO_3 acid model). In the case of Me–TEDGA with the H^+ representation of the acid, this is probably caused by different location of bonding H^+ mentioned in section 2.3.1. The $N^{(1)}$–$C^{(2)}$ bond is particularly important in the case of the degradation mechanism based on the electron transfer initiation, see section 2.1.1. The increasing trend indicates the rise in the stability of ligand in accordance with the experimental trend, i.e., the stability of TMDGA < TEDGA < Me–TEDGA < Me_2–TEDGA. However, this cannot be taken as sufficiently reliable information, since at least 2 exceptions that are mentioned above are found.

2.3.6 Electrostatic potential

The ESP is usually used to investigate intermolecular interactions and also to understand the interaction with an electrophilic species. Negative values imply that the corresponding location is more susceptible to a reaction with an electrophilic particle. The ESP is mapped on the isosurface of the electron density, for all cases the value of the density is 0.017 e·Å^{-3}.

Results of the ESP from the previous work [5] are used as additional information while creating the system with the acid. Because the particles representing the acid usually have a positive charge, places where negative ESP maxima usually occur are selected as prospective positions.

Results for each acid model are similar for all ligands without any trend explaining differences in their stability. This is illustrated in the case of the H^+ acid model in figure 2.10: no change of the minima or maxima is evident. The same results were obtained in the previous work without acid models [5]. Results for the remaining cases of the acid influence model are in appendix D. Large differences in values of the ESP can be detected, and they depend on the particular acid model. This is caused by the specific introduction of the acid model. The total charge of the system is not the same in all cases. It is zero for the HNO_3 acid model and it is $+1$ for H^+ and H_3O^+ models.

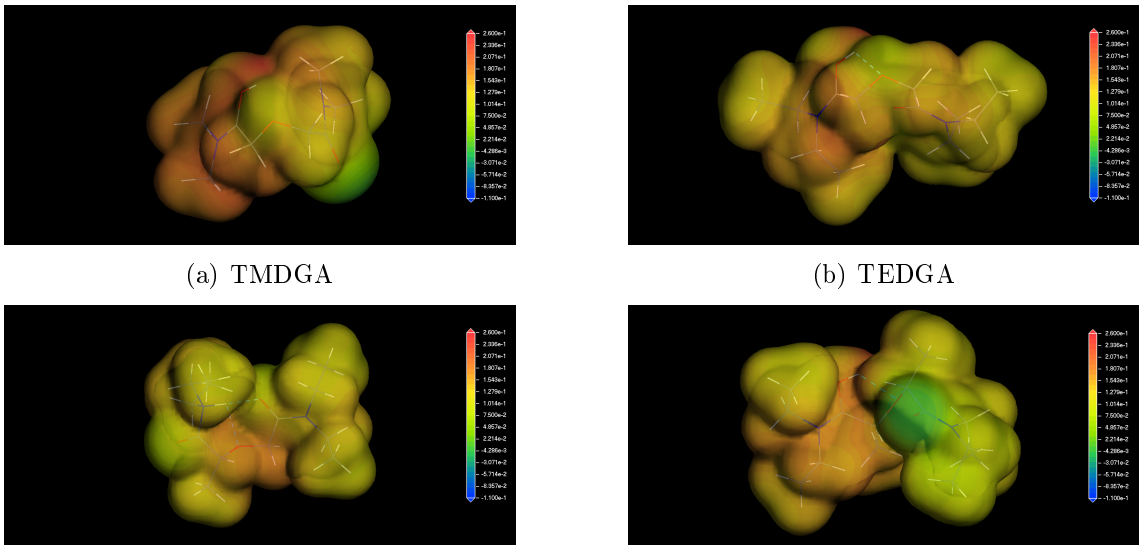

(a) TMDGA (b) TEDGA

(c) Me–TEDGA (d) Me_2–TEDGA

Figure 2.10 Electrostatic potencials mapped on an isosurface of the electron density with value 0.017 e·Å^{-3} for the H^+ acid model of (a) TMDGA, (b) TEDGA, (c) Me–TEDGAa (d) Me_2–TEDGA; (settings: DMol^3, DNP, B3LYP, GD2, COSMO)

In the previous work two locations with the negative ESP were observed. The first one was on the carbonyl oxygens and the other one was on the ether oxygen. The same situation is observed for all the acid models, illustrated for TEDGA in figure 2.11. The red circles mark minima on carbonyl oxygens and the white circle marks the minimum on the ether oxygen. These minima are in agreement with the partial charges on those oxygens, presented in section 2.3.4. Yet, in cases of the acid representation, other maxima appeared. The most significant of them is located on the nitric acid molecule for the HNO_3 acid model. But since these maxima usually appeared on an acid-representing molecule outside the ligand itself, we do not interpret it as an indicator of the stability of the ligand.

The analysis of ESP does not provide any trend that could confirm or disprove the experimentally determined stability of the ligands. This is the same result as has been obtained in the previous work [5].

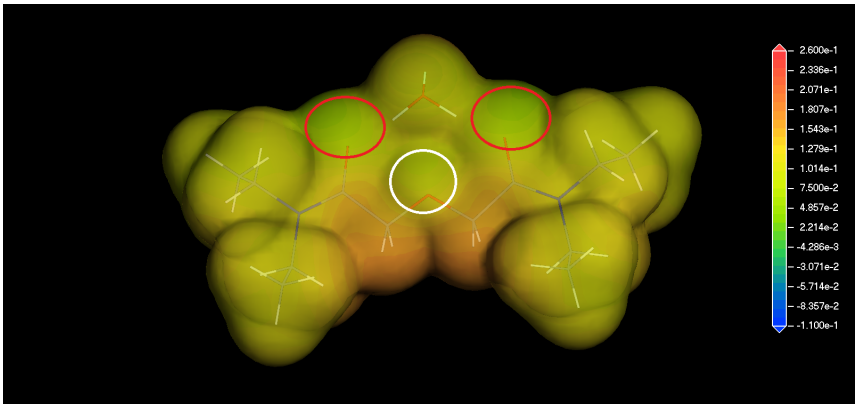

Figure 2.11 Electrostatic potential mapped on an isosurface of the electron density with value 0.017 e·Å^{-3} for the H_3O^+ acid model of TEDGA; red circles indicate minima on carbonyl oxygens, white circle indicates minimum on ether oxygen; (settings: DMol^3, DNP, B3LYP, GD2, COSMO)

2.3.7 Energy profiles of the reaction mechanism

The degradation reaction mechanism based on the hydrogen abstraction (section 2.1.1) is investigated for the studied ligands. No acid representation is considered during these calculations. QST2, QST3 [51, 52] and TS [53] algorithm options of Gaussian09 code [73] are used for searching transition states. Conformation analysis of reactants, intermediates and products is done by the CREST utility of xTB software (section 2.3.1).

Energy of each compound is calculated separately with the thermochemistry correction taken into account and final energies are normalized to the energy of the reactants. Three approaches of determination of energy are used in this Master's thesis. The first one is using Gaussian09 code with 6–311++G(2d,d,p) basis set (rest of the settings in section 2.2.2) including thermochemistry correction calculations. The second one is using Def2TZVP basis set and the rest of the settings is the same as in the first case. The last one consists of the CC single point calculations in Orca software (settings in section 2.2.3) on geometries obtained by the DFT calculations with Def2TZVP basis set. The thermochemistry corrections from the DFT calculations are added to total energy obtained by the CC calculations. The last approach is considered to be the best one available today and the only one discussed below. Results of the remaining calculations are summarized in appendix E.2.

The proposed degradation mechanism is initiated by a free radical, which causes the abstraction of the hydrogen bonded to one of the ether carbons. This radical can be represented by a hydroxyl radical OH• (water solution) or a hydrogen radical H• (organic solution). Consequently, the ether C–O bond ruptures. Methyl groups added in methylated derivates of TEDGA should protect the adjacent ether C–O bond. For this reason, two possible reaction pathways are taken into consideration for Me–TEDGA. Schemes are shown in figures 2.12 for the hydrogen radical H• and in appendix E.1 for the hydroxyl radical OH•.

Calculations of transition states performed for the first step of the hydrogen abstraction by a hydroxyl radical OH• (figure E.1) did not converge to saddle points. The reason for this behaviour is unknown, but generally, searching for transition

states is sometimes unsuccessful. Because of this, only calculations of the hydrogen abstraction by a hydrogen radical are done and discussed below. Additionally, the first step only differs in transition state and the replacement of a hydroxyl radical by a hydrogen radical is simplification of the calculations.

Considering the abstraction of the hydrogen adjacent to the ether group as the initiation of the degradation reaction, it must not be forgotten that in the case of methylated ligands the number of possible reaction centres (a hydrogen adjacent to the ether group at positions R^1 – R^4) is lower. TMDGA and TEDGA have four of these hydrogens, but only three hydrogen of this type are present in Me–TEDGA, and only two hydrogens are available in Me_2–TEDGA. This correspondingly reduces the probability of the abstraction of a hydrogen for methylated ligands in accordance with the experimentally observed trend of the stability.

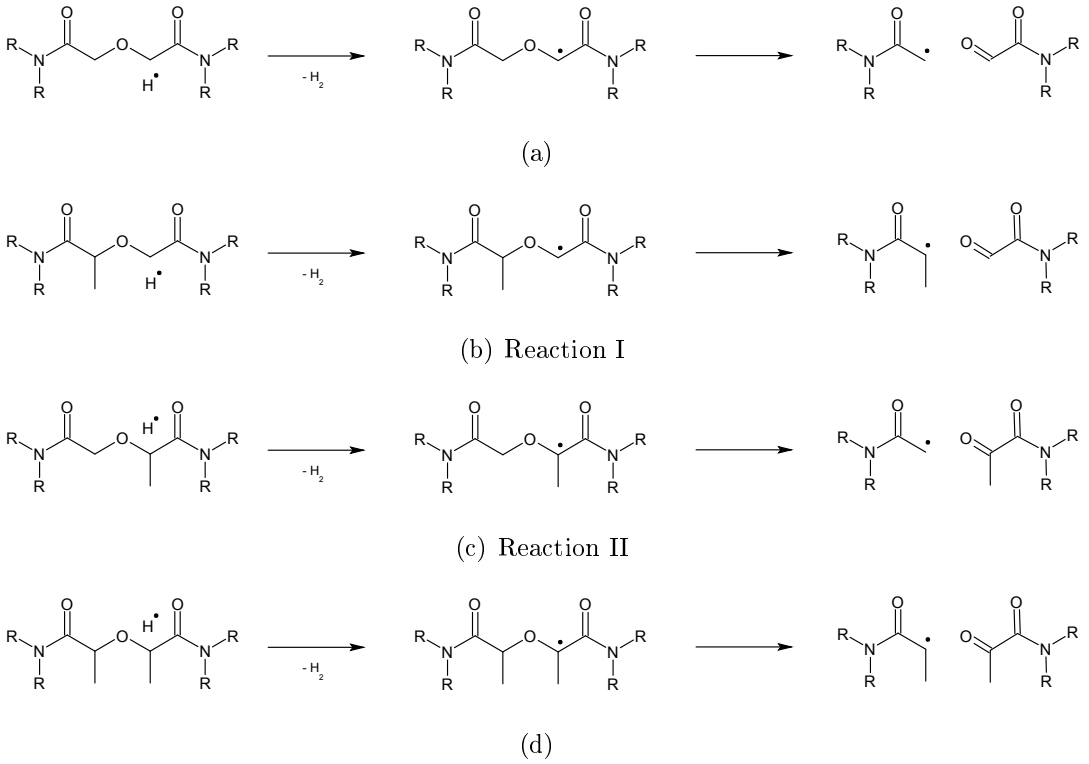

Figure 2.12 Reactions scheme considered for degradation mechanism based on hydrogen abstraction by hydroxyl radical H• (a) for TMDGA and TEDGA, (b) for Me–TEDGA leading to a rupture of the protected ether bond, (c) for Me–TEDGA causing a break of the unprotected ether bond and (d) for Me_2–TEDGA.

Hydrogen abstraction by hydrogen radical H•

Energy diagrams obtained for the first reaction step and for the whole reaction pathway are shown in figure 2.13 and 2.14 respectively. Corresponding values to figure 2.14 are in table 2.24. Activation and reaction energy is in table 2.23.

The activation energies E_a of the first reaction step are similar for all ligands except for Me–TEDGA reaction option I (figure 2.13). For Me–TEDGA reaction

option I, the highest energy barrier is observed 17.43 kcal mol^{-1} comparing to 13.20 kcal mol^{-1} for reaction option II. The same observation was for methylated derivative of TODGA (TWE 21) [7]. The activation energy for TMDGA (15.08 kcal mol^{-1}) is higher than for TEDGA (14.19 kcal mol^{-1}). This behaviour contradicts the experimentally observed stability [3, 4]. However, it is in agreement with experimentally measured rate coefficients for this reaction in [4] ($1.22 \pm 0.03 \cdot 10^8$ $M^{-1}s^{-1}$ for TMDGA and $1.60 \pm 0.09 \cdot 10^8$ $M^{-1}s^{-1}$ for TEDGA). The activation energy for Me_2–TEDGA is 14.92 kcal mol^{-1} that is higher than for TEDGA but lower than for TMDGA. This comparison with TMDGA is in disagreement with experimentally measured rate coefficient for Me_2–TEDGA ($0.36 \pm 0.07 \cdot 10^8$ $M^{-1}s^{-1}$ [4]). However, the energy difference between TMDGA and Me_2–TEDGA is small. In such case, caution is advised when interpreting such small energetic differences because significant influence of uncertainties and fluctuations in the geometries of the transient states can be significant [7].

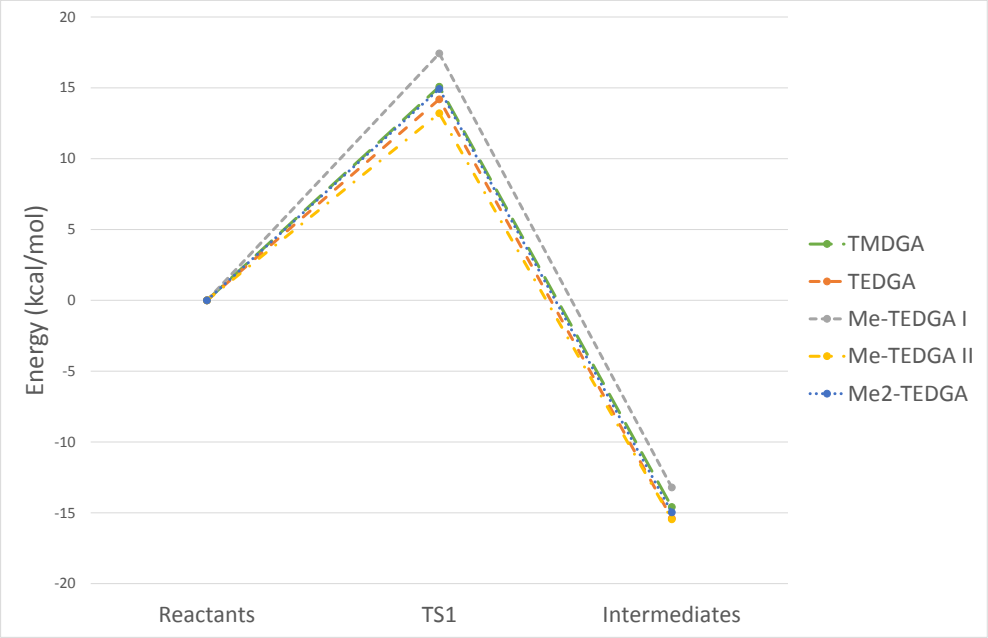

Figure 2.13 Energy diagram of the first step of the degradation mechanism calculated with CC theory

Differences among the activation energies of the second reaction step for studied ligands are so small that any interpretation is unclear. Generally, the activation energy of the second reaction step is higher than for the first reaction step for all ligands (for TEDGA $E_a = 21.76$ kcal mol^{-1} for the second reaction step and $E_a = 14.19$ kcal mol^{-1} for the first reaction step). This suggests that the second reaction step determines the overall reaction speed. Similar phenomenon was observed for TODGA and its methylated derivatives [7]. However, the energy barriers obtained for the fist reaction step in case of TODGA were significantly lower ($E_a = 5.74$

kcal mol^{-1} [7]) than for the studied hydrophilic DGAs in this thesis (for TEDGA $E_a = 14.19$ kcal mol^{-1}). This disagreement is caused by using DFT calculations in [7], but simulations in this thesis are based on CC theory (section 1.3) that is much more accurate that DFT.

Table 2.23 Activation (E_a) and reaction (E_r) energy (kcal mol^{-1}) for the proposed degradation mechanisms (figure 2.12) calculated with CC theory

	First step		Second step	
molecule	E_a(kcal mol^{-1})	E_r(kcal mol^{-1})	E_a(kcal mol^{-1})	E_r(kcal mol^{-1})
TMDGA	15.08	−14.59	19.23	−2.76
TEDGA	14.19	−15.40	21.76	−2.30
Me–TEDGA reaction I	17.43	−13.21	21.60	−6.73
Me–TEDGA reaction II	13.20	−15.46	21.27	−7.53
Me_2–TEDGA	14.92	−14.97	20.90	−8.39

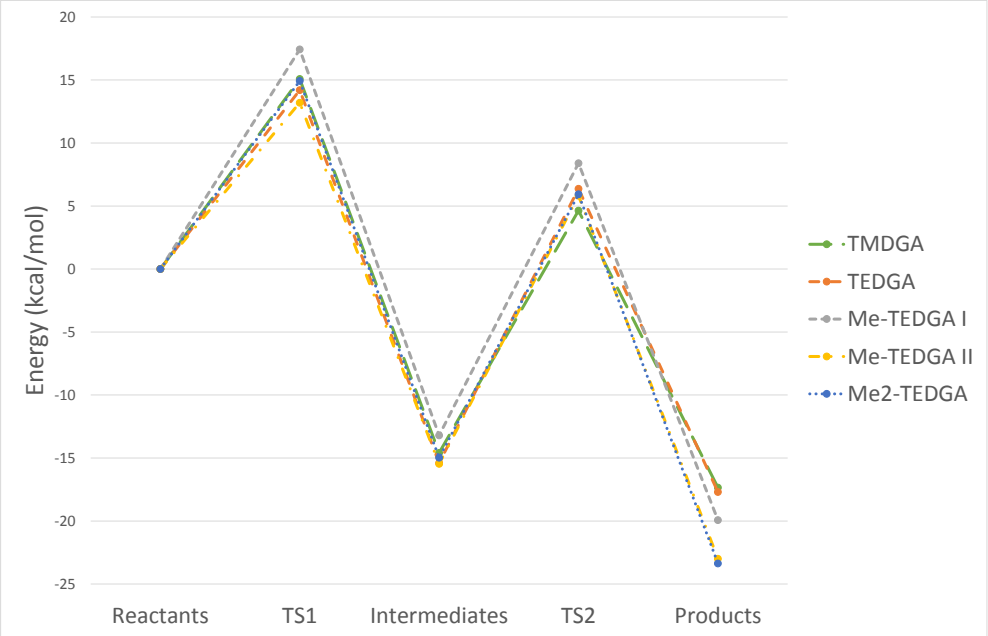

Figure 2.14 Energy diagram for the proposed degradation mechanisms calculated with CC theory

In study of TODGA and its methylated derivatives [7], thermodynamic control of the reaction was suggested to be dominant. In this case, the change in potential energy between the reactants and products would have a decisive impact on the composition of final products [7]. The explanation is that the generally small energetic

barrier was observed comparing to the high potential energy drop for the first reaction step [7]. However, this is not the case for studied ligands in this thesis (can be caused by higher level of theory that is used). For example, the activation energy of the first reaction step is 14.19 kcal mol^{-1} and the decrease in potential energy is 15.40 kcal mol^{-1} for TEDGA. The similar situation is observed for the remaining ligands in the case of the first reaction step (table 2.23). For the second reaction step, the reaction energy is much lower than the activation energy for all ligands. Furthermore, the total drops in potential energy are in disagreement with the experimentally observed stability of the ligands (TMDGA < TEDGA < Me–TEDGA < Me_2–TEDGA [3]).

For Me–TEDGA, an interesting difference is observed for the first reaction step between the two considered reaction possibilities. In the case of the reaction option I, the energetic barrier is higher and the decrease in potential energy is smaller than for the reaction option II. This suggests that the hydrogen abstraction is more likely to occur in the case of the reaction possibility II. The second reaction step is also interesting. The activation energy is almost the same for both possible reactions (21.60 kcal mol^{-1} for I and 21.27 kcal mol^{-1} for II), but the difference confirms the general consequence of the presence of a methyl group on adjacent bonds. The consequence is that the presence of a methyl group leads to increasing the stability of adjacent bonds. For the reaction option I, the methyl group is attached to C–O bond that ruptures. Nevertheless, caution must be taken when interpreting such small energetic differences. The decrease in potential energy (6.73 kcal mol^{-1} for option I and 7.53 kcal mol^{-1} for II one) is also in agreement with this consequence. However, the exact opposite was observed for TWE21 (methylated derivative of TODGA) [7].

Table 2.24 Reaction energy profile parameters (kcal mol^{-1}) for the proposed degradation mechanism (figure 2.12) calculated with CC theory, R stands for Reactants, TS1 for Transition state 1, I for intermediates, TS2 for Transition state 2 and P for Products

Reaction energy profile (kcal mol^{-1})					
molecule	R	TS 1	I	TS2	P
TMDGA	0	15.08	−14.59	4.64	−17.35
TEDGA	0	14.19	−15.40	6.37	−17.69
Me–TEDGA reaction I	0	17.43	−13.21	8.39	−19.93
Me–TEDGA reaction II	0	13.20	−15.46	5.81	−23.00
Me_2–TEDGA	0	14.92	−14.97	5.94	−23.36

The investigation of the reaction energy diagrams does not support the experimentally observed trend of the stability (TMDGA < TEDGA < Me–TEDGA < Me_2–TEDGA [3]). Futhermore, disagreements with similar study for TODGA and its methylated derivatives are found due to using more accurate level of theory. In the case of the hydrogen abstraction by a hydroxyl radical, only the activation energy of the first reaction step will differ. The rest of the proposed reaction is the same as for a hydrogen radical. The experimental studies [3, 4] suggest that a hydroxyl radical is dominant. However, corresponding transition states were not found.

Conclusion

This Master's thesis focuses primarily on the theoretical study of the radiolytic stability of selected representatives of the DGA family of extractants. Furthermore, the connection between the physico–chemical properties of the electron density and the experimentally determined stability [3, 4] is searched. The following DGA extractants are investigated:

- TMDGA
- TEDGA
- Me–TEDGA
- Me_2–TEDGA.

The experimentally determined trend of the stability increases with increasing molecular weight [3, 4], i.e., the trend can be written in the form: TMDGA < TEDGA < Me–TEDGA < Me_2–TEDGA. This work is intended to follow the conditions and settings present during the experimental studies [3, 4]. The following computational codes are used: $DMol^3$ module of Materials studio 8.0, CREST utility from xTB code, Orca 4.0.1.2 Release and Gaussian09.

Three possible models of the acid influence are proposed, compared to each other, and compared to the results without any acid influence gained in previous works [5, 6]. The first model is represented by the implementation of an H^+ cation to the studied system. The second one implements an H_3O^+ cation and the last one implements an undissociated nitric acid molecule.

Two proposed reaction mechanisms are considered as was suggested in the previous works [5, 6]. The first one is the hydrogen abstraction from the ether group and the other one is the electron transfer from the amide group.

The inclusion of the acid influence does not generally change trends observed in previous works [5, 6]. The trend of decreasing radical Fukui function extreme with increasing molecular weight remains unchanged and is enhanced for the cases involving the acid models (for example, no acid considered: TMDGA 3.613, TEDGA 3.613, Me–TEDGA 3.325 and Me_2–TEDGA 3.038; H^+ acid model: TMDGA 5.847, TEDGA 4.716, Me–TEDGA 4.235 and Me_2–TEDGA 2.663). The trend is in agreement with the experimentally determined stability [3, 4]. Furthermore, the unchanged trend confirms that the acid influence does not act directly on the extractant. On the contrary, the acid molecule preferably reacts with the radicals from the solvent radiolysis and thereby protects the extractant molecules [4].

Radical Fukui charges values are generally lower with the acid models included than without the acid influence. This supports the idea of the positive acid effect on the stability. Some differences are caused by the specific way of including the acid influence. This is the case of partial charges where the different location of bonding the acid representation molecule causes the trend violation. The rest of the calculated properties (bond orders, HOMO–LUMO gaps, ESP) do not show any difference in trends from the previous results without the acid models. This supports the experimentally observed behaviour of the nitric acid mentioned above [4].

The reaction degradation mechanisms are also proposed in this thesis and the corresponding reaction diagrams calculated. The considered reaction is based on the hydrogen abstraction in the vicinity of the ether group by the hydrogen radical. However, the investigation of the energy diagram does not support the experimentally observed trend of the stability (TMDGA < TEDGA < Me–TEDGA < Me_2–TEDGA [3, 4]). The obtained results disagree with the similar study that has been performed for TODGA and its derivatives, especially in the difference between two reaction pathways of Me–TEDGA observed in this study. Application of a more accurate level of theory is likely to be addressed in this regard.

Even though the experimental studies [3, 4] suggest that a hydroxyl radical is dominant in the reaction, only results obtained with a hydrogen radical could be obtained and analysed. The reason is in the lack of convergence of the transient state calculations dealing with the hydroxyl radical. Thus, the transient states have not been found for the case of the hydroxyl radical. This is probably caused by the flat shape of the PESs around these transition states. The numbers of conformers and their small energy differences (2.3.1) support the ideal of the flat shape of the PESs, Subsequently, the algorithms are unable to find them.

The obtained results contribute to theoretical understanding of the possible reaction mechanisms involved in the degradation of hydrophilic DGAs. Furthermore, the collected theoretical data can further foster the development of methods that provide the theoretical predictions of molecular stability and models of the acid influence. Last but not least, the presented work can contribute to the development of the real experimental separation methods.

Bibliography

[1] J. Veliscek-Carolan. Separation of actinides from spent nuclear fuel: A review. *Journal of hazardous materials*, 318:266–281, 2016.

[2] G. Modolo, H. Asp, C. Schreinemachers, and H. Vijgen. Development of a TODGA based process for partitioning of actinides from a PUREX raffinate Part I: Batch extraction optimization studies and stability tests. *Solvent Extraction and Ion Exchange*, 25(6):703–721, 2007.

[3] A. Wilden, B. J. Mincher, S. P. Mezyk, L. Twight, K. M. Rosciolo-Johnson, C. A. Zarzana, M. E. Case, M. Hupert, A. Stärk, and G. Modolo. Radiolytic and hydrolytic degradation of the hydrophilic diglycolamides. *Solvent Extraction and Ion Exchange*, 36(4):347–359, 2018.

[4] G. P. Horne, A. Wilden, S. P. Mezyk, L. Twight, M. Hupert, A. Stärk, W. Verboom, B. J. Mincher, and G. Modolo. Gamma radiolysis of hydrophilic diglycolamide ligands in concentrated aqueous nitrate solution. *Dalton Transactions*, 48(45):17005–17013, 2019.

[5] J. Luštinec. Využití kvantové chemie pro charakterizaci stability organických ligandů. B.S. thesis, České vysoké učení technické v Fakulta jaderná a fyzikálně inženýrská, Praha 2018.

[6] T. Koubský and J. Luštinec. Application of quantum mechanical simulations for studying the radiolytic stability of prospective extractants in the nuclear fuel cycle. *Journal of Radioanalytical and Nuclear Chemistry*, 318(3):2407–2413, 2018.

[7] T. Koubský, J. Fojtíková, and L. Kalvoda. Radical degradation stability of ether linkage in *N,N,N',N'*-tetraoctyldiglycolamide and related organic extractants: A density functional study. *Progress in Nuclear Energy*, 94:208 – 215, 2017.

[8] R. M. Martin. *Electronic structure: basic theory and practical methods*. Cambridge university press, New York, NY USA 2004.

[9] A. Szabo and N. S. Ostlund. *Modern quantum chemistry: introduction to advanced electronic structure theory*. Courier Corporation, Mineola, New York 2012.

[10] A. R. Leach. *Molecular modelling: principles and applications*. Pearson Prentice Hall, 2 edition, Harlow, UK 2009.

[11] J. Formánek. *Úvod do kvantové teorie.* Academia ISBN, Praha 1983.

[12] C. J. Cramer. *Essentials of computational chemistry: Theories and models.* John Wiley & Sons Chichester, 2004.

[13] J. D. Patterson and B. C. Bailey. *Solid-state physics: introduction to the theory.* Springer Science & Business Media, Cham 2007, ISBN 978-3-319-75322-5.

[14] P. Hohenberg and W. Kohn. Inhomogeneous electron gas. *Physical review*, 136(3B):B864, 1964.

[15] W. Kohn and L. J. Sham. Self-consistent equations including exchange and correlation effects. *Physical review*, 140(4A):A1133, 1965.

[16] A. I. Ciucivara. *Density functional studies of magnetic semiconductors and multiferroics.* PhD thesis, The University of Texas at Austin, 2007.

[17] J. P. Perdew and Y. Wang. Accurate and simple analytic representation of the electron-gas correlation energy. *Phys. Rev. B*, 45:13244–13249, Jun 1992.

[18] S. H. Vosko, L. Wilk, and M. Nusair. Accurate spin-dependent electron liquid correlation energies for local spin density calculations: a critical analysis. *Canadian Journal of physics*, 58(8):1200–1211, 1980.

[19] J. P. Perdew, K. Burke, and M. Ernzerhof. Generalized gradient approximation made simple. *Physical review letters*, 77(18):3865, 1996.

[20] A. D. Becke. Correlation energy of an inhomogeneous electron gas: A coordinate-space model. *The Journal of chemical physics*, 88(2):1053–1062, 1988.

[21] C. Lee, W. Yang, and R. G. Parr. Development of the Colle-Salvetti correlation-energy formula into a functional of the electron density. *Physical review B*, 37(2):785, 1988.

[22] A. D. Becke. Density-functional thermochemistry. III. The role of exact exchange. *The Journal of chemical physics*, 98(7):5648–5652, 1993.

[23] P. Stephens, F. Devlin, C. Chabalowski, and M. J. Frisch. Ab initio calculation of vibrational absorption and circular dichroism spectra using density functional force fields. *The Journal of Physical Chemistry*, 98(45):11623–11627, 1994.

[24] S. Grimme, J. Antony, S. Ehrlich, and H. Krieg. A consistent and accurate ab initio parametrization of density functional dispersion correction (DFT-D) for the 94 elements H-Pu. *The Journal of chemical physics*, 132(15):154104, 2010.

[25] S. Grimme, S. Ehrlich, and L. Goerigk. Effect of the damping function in dispersion corrected density functional theory. *Journal of computational chemistry*, 32(7):1456–1465, 2011.

[26] S. Grimme. Semiempirical GGA-type density functional constructed with a long-range dispersion correction. *Journal of computational chemistry*, 27(15):1787–1799, 2006.

[27] E. R. McNellis, J. Meyer, and K. Reuter. Azobenzene at coinage metal surfaces: role of dispersive van der Waals interactions. *Physical Review B*, 80(20):205414, 2009.

[28] Y. Liu and W. A. I. Goddard. A universal damping function for empirical dispersion correction on density functional theory. *Materials transactions*, 50(7):1664–1670, 2009.

[29] B. Delley. An all-electron numerical method for solving the local density functional for polyatomic molecules. *The Journal of chemical physics*, 92(1):508–517, 1990.

[30] B. Delley. From molecules to solids with the $DMol^3$ approach. *The Journal of chemical physics*, 113(18):7756–7764, 2000.

[31] D. S. BIOVIA. *Materials studio online help, Release 8.0*. Dassault Systemes, 2017.

[32] F. Weigend, F. Furche, and R. Ahlrichs. Gaussian basis sets of quadruple zeta valence quality for atoms H–Kr. *The Journal of chemical physics*, 119(24):12753–12762, 2003.

[33] F. Weigend and R. Ahlrichs. Balanced basis sets of split valence, triple zeta valence and quadruple zeta valence quality for H to Rn: Design and assessment of accuracy. *Physical Chemistry Chemical Physics*, 7(18):3297–3305, 2005.

[34] F. Weigend. Accurate Coulomb-fitting basis sets for H to Rn. *Physical chemistry chemical physics*, 8(9):1057–1065, 2006.

[35] A. Schäfer, H. Horn, and R. Ahlrichs. Fully optimized contracted Gaussian basis sets for atoms Li to Kr. *The Journal of Chemical Physics*, 97(4):2571–2577, 1992.

[36] A. Schäfer, C. Huber, and R. Ahlrichs. Fully optimized contracted Gaussian basis sets of triple zeta valence quality for atoms Li to Kr. *The Journal of Chemical Physics*, 100(8):5829–5835, 1994.

[37] J. Čížek. On the correlation problem in atomic and molecular systems. Calculation of wavefunction components in Ursell-type expansion using quantum-field theoretical methods. *The Journal of Chemical Physics*, 45(11):4256–4266, 1966.

[38] J. Čížek. On the use of the cluster expansion and the technique of diagrams in calculations of correlation effects in atoms and molecules. *Advances in chemical physics*, pages 35–89, 1969.

[39] R. J. Bartlett and G. D. Purvis. Many-body perturbation theory, coupled-pair many-electron theory, and the importance of quadruple excitations for the correlation problem. *International Journal of Quantum Chemistry*, 14(5):561–581, 1978.

[40] J. Pople, R. Krishnan, H. Schlegel, and J. Binkley. Electron correlation theories and their application to the study of simple reaction potential surfaces. *International Journal of Quantum Chemistry*, 14(5):545–560, 1978.

[41] G. D. Purvis III and R. J. Bartlett. A full coupled-cluster singles and doubles model: The inclusion of disconnected triples. *The Journal of Chemical Physics*, 76(4):1910–1918, 1982.

[42] J. A. Pople, M. Head-Gordon, and K. Raghavachari. Quadratic configuration interaction. A general technique for determining electron correlation energies. *The Journal of chemical physics*, 87(10):5968–5975, 1987.

[43] G. E. Scuseria, C. L. Janssen, and H. F. Schaefer Iii. An efficient reformulation of the closed-shell coupled cluster single and double excitation (CCSD) equations. *The Journal of Chemical Physics*, 89(12):7382–7387, 1988.

[44] G. E. Scuseria and H. F. Schaefer III. Is coupled cluster singles and doubles (CCSD) more computationally intensive than quadratic configuration interaction (QCISD)? *The Journal of Chemical Physics*, 90(7):3700–3703, 1989.

[45] J. Chen, B. Chan, Y. Shao, and J. Ho. How accurate are approximate quantum chemical methods at modelling solute–solvent interactions in solvated clusters? *Physical Chemistry Chemical Physics*, 22(7):3855–3866, 2020.

[46] J. Tomasi and M. Persico. Molecular interactions in solution: an overview of methods based on continuous distributions of the solvent. *Chemical Reviews*, 94(7):2027–2094, 1994.

[47] A. Klamt and G. Schüürmann. COSMO: a new approach to dielectric screening in solvents with explicit expressions for the screening energy and its gradient. *Journal of the Chemical Society, Perkin Transactions 2*, (5):799–805, 1993.

[48] S. Miertuš, E. Scrocco, and J. Tomasi. Electrostatic interaction of a solute with a continuum. A direct utilizaion of AB initio molecular potentials for the prevision of solvent effects. *Chemical Physics*, 55(1):117–129, 1981.

[49] J.-L. Pascual-ahuir, E. Silla, and I. Tunon. GEPOL: An improved description of molecular surfaces. III. A new algorithm for the computation of a solvent-excluding surface. *Journal of Computational Chemistry*, 15(10):1127–1138, 1994.

[50] E. G. Lewars. The concept of the potential energy surface. In *Computational Chemistry*, pages 9–49. Springer, 2016.

[51] C. Peng and H. Bernhard Schlegel. Combining synchronous transit and quasi-newton methods to find transition states. *Israel Journal of Chemistry*, 33(4):449–454, 1993.

[52] C. Peng, P. Y. Ayala, H. B. Schlegel, and M. J. Frisch. Using redundant internal coordinates to optimize equilibrium geometries and transition states. *Journal of Computational Chemistry*, 17(1):49–56, 1996.

[53] X. Li and M. J. Frisch. Energy-represented direct inversion in the iterative subspace within a hybrid geometry optimization method. *Journal of chemical theory and computation*, 2(3):835–839, 2006.

[54] Gaussian 16 Users Reference. `http://gaussian.com/man/`. Accessed: 2020-2-15.

[55] A. D. McNaught, A. Wilkinson, et al. *Compendium of chemical terminology*, volume 1669. Blackwell Science Oxford, 1997.

[56] D. Young. *Computational chemistry: a practical guide for applying techniques to real world problems*. John Wiley & Sons, 2004.

[57] E. Vanden-Eijnden et al. Transition-path theory and path-finding algorithms for the study of rare events. *Annual review of physical chemistry*, 61:391–420, 2010.

[58] A. Arnaldsson. *Calculation of quantum mechanical rate constants directly from ab initio atomic forces*. PhD thesis, University of Washington, 2007.

[59] R. Xiao, M. Noerpel, H. Ling Luk, Z. Wei, and R. Spinney. Thermodynamic and kinetic study of ibuprofen with hydroxyl radical: a density functional theory approach. *International Journal of Quantum Chemistry*, 114(1):74–83, 2014.

[60] A. Cornish-Bowden. *Fundamentals of enzyme kinetics*. John Wiley & Sons, 2013.

[61] R. S. Mulliken. Electronic population analysis on LCAO–MO molecular wave functions. II. Overlap populations, bond orders, and covalent bond energies. *The Journal of Chemical Physics*, 23(10):1833–1840, 1955.

[62] S. M. Bachrach. Population analysis and electron densities from quantum mechanics. *Reviews in Computational Chemistry, Volume 5*, pages 171–228, 2007.

[63] P. K. Chattaraj. *Chemical reactivity theory: a density functional view*. CRC press, 2009.

[64] F. L. Hirshfeld. Bonded-atom fragments for describing molecular charge densities. *Theoretica chimica acta*, 44(2):129–138, 1977.

[65] I. Mayer. Bond orders and valences from ab initio wave functions. *International Journal of Quantum Chemistry*, 29(3):477–483.

[66] U. C. Singh and P. A. Kollman. An approach to computing electrostatic charges for molecules. *Journal of Computational Chemistry*, 5(2):129–145, 1984.

[67] R. G. Parr and R. G. Pearson. Absolute hardness: companion parameter to absolute electronegativity. *Journal of the American Chemical Society*, 105(26):7512–7516, 1983.

[68] W. Yang and R. G. Parr. Hardness, softness, and the fukui function in the electronic theory of metals and catalysis. *Proceedings of the National Academy of Sciences*, 82(20):6723–6726, 1985.

[69] Z. Zhou and R. G. Parr. Activation hardness: new index for describing the orientation of electrophilic aromatic substitution. *Journal of the American Chemical Society*, 112(15):5720–5724, 1990.

[70] R. G. Pearson. Chemical hardness and density functional theory. *Journal of Chemical Sciences*, 117(5):369–377, 2005.

[71] R. G. Parr. Density functional theory of atoms and molecules. In F. K. and P. B., editors, *Horizons of quantum chemistry*. International Academy of Quantum Molecular Science, vol 3. Springer, Dordrecht, 1980.

[72] K. Fukui. Role of frontier orbitals in chemical reactions. *science*, 218(4574):747–754, 1982.

[73] M. J. Frisch, G. W. Trucks, H. B. Schlegel, G. E. Scuseria, M. A. Robb, J. R. Cheeseman, J. A. Montgomery, Jr., T. Vreven, K. N. Kudin, J. C. Burant, J. M. Millam, S. S. Iyengar, J. Tomasi, V. Barone, B. Mennucci, M. Cossi, G. Scalmani, N. Rega, G. A. Petersson, H. Nakatsuji, M. Hada, M. Ehara, K. Toyota, R. Fukuda, J. Hasegawa, M. Ishida, T. Nakajima, Y. Honda, O. Kitao, H. Nakai, M. Klene, X. Li, J. E. Knox, H. P. Hratchian, J. B. Cross, V. Bakken, C. Adamo, J. Jaramillo, R. Gomperts, R. E. Stratmann, O. Yazyev, A. J. Austin, R. Cammi, C. Pomelli, J. W. Ochterski, P. Y. Ayala, K. Morokuma, G. A. Voth, P. Salvador, J. J. Dannenberg, V. G. Zakrzewski, S. Dapprich, A. D. Daniels, M. C. Strain, O. Farkas, D. K. Malick, A. D. Rabuck, K. Raghavachari, J. B. Foresman, J. V. Ortiz, Q. Cui, A. G. Baboul, S. Clifford, J. Cioslowski, B. B. Stefanov, G. Liu, A. Liashenko, P. Piskorz, I. Komaromi, R. L. Martin, D. J. Fox, T. Keith, M. A. Al-Laham, C. Y. Peng, A. Nanayakkara, M. Challacombe, P. M. W. Gill, B. Johnson, W. Chen, M. W. Wong, C. Gonzalez, and J. A. Pople. Gaussian 09, Revision D.01. Gaussian, Inc., Wallingford, CT, 2004.

[74] F. Neese. The ORCA program system. *Wiley Interdisciplinary Reviews: Computational Molecular Science*, 2(1):73–78, 2012.

[75] F. Neese. Software update: the ORCA program system, version 4.0. *Wiley Interdisciplinary Reviews: Computational Molecular Science*, 8(1):e1327, 2018.

[76] Y. Sasaki, H. Suzuki, Y. Sugo, T. Kimura, and G. R. Choppin. New water-soluble organic ligands for actinide cations complexation. *Chemistry letters*, 35(3):256–257, 2006.

[77] C. Rostaing, C. Poinssot, D. Warin, P. Baron, and B. Lorraina. Development and validation of the EXAm separation process for single Am recycling. *Procedia Chemistry*, 7:367–373, 2012.

[78] G. J. Lumetta, A. V. Gelis, J. C. Carter, C. M. Niver, and M. R. Smoot. The actinide-lanthanide separation concept. *Solvent Extraction and Ion Exchange*, 32(4):333–347, 2014.

[79] K. Van Hecke and G. Modolo. Separation of actinides from low level liquid wastes (LLLW) by extraction chromatography using novel DMDOHEMA and

TODGA impregnated resins. *Journal of radioanalytical and nuclear chemistry*, 261(2):269–275, 2004.

[80] H. Ikeda and A. Suzuki. Radiolysis of *n*-dodecane and its physical property change based on the dose in one pass through a reference HA column. *Journal of nuclear science and technology*, 35(10):697–704, 1998.

[81] M. B. Singh, S. R. Patil, A. A. Lohi, and V. G. Gaikar. Insight into nitric acid extraction and aggregation of N, N, N', N'-Tetraoctyl diglycolamide (TODGA) in organic solutions by molecular dynamics simulation. *Separation Science and Technology*, 53(9):1361–1371, 2018.

[82] P. Matveev, A. Mitrofanov, V. Petrov, S. Zhokhov, A. Smirnova, Y. A. Ustynyuk, and S. Kalmykov. Testing a simple approach for theoretical evaluation of radiolysis products in extraction systems. A case of N, O-donor ligands for Am/Eu separation. *RSC Advances*, 7(87):55441–55449, 2017.

[83] a. Petersson, A. Bennett, T. G. Tensfeldt, M. A. Al-Laham, W. A. Shirley, and J. Mantzaris. A complete basis set model chemistry. I. The total energies of closed-shell atoms and hydrides of the first-row elements. *The Journal of chemical physics*, 89(4):2193–2218, 1988.

[84] G. Petersson and M. A. Al-Laham. A complete basis set model chemistry. II. Open-shell systems and the total energies of the first-row atoms. *The Journal of chemical physics*, 94(9):6081–6090, 1991.

[85] J. Tomasi, B. Mennucci, and R. Cammi. Quantum mechanical continuum solvation models. *Chemical reviews*, 105(8):2999–3094, 2005.

[86] P. Pracht, F. Bohle, and S. Grimme. Automated exploration of the low-energy chemical space with fast quantum chemical methods. *Physical Chemistry Chemical Physics*, 22(14):7169–7192, 2020, doi:10.1039/c9cp06869d.

[87] S. Grimme, C. Bannwarth, and P. Shushkov. A robust and accurate tight-binding quantum chemical method for structures, vibrational frequencies, and noncovalent interactions of large molecular systems parametrized for all spd-block elements (Z= 1–86). *Journal of chemical theory and computation*, 13(5):1989–2009, 2017.

[88] C. Bannwarth, S. Ehlert, and S. Grimme. GFN2-xTB—An accurate and broadly parametrized self-consistent tight-binding quantum chemical method with multipole electrostatics and density-dependent dispersion contributions. *Journal of chemical theory and computation*, 15(3):1652–1671, 2019.

[89] P. Pracht, E. Caldeweyher, S. Ehlert, and S. Grimme. A Robust Non-Self-Consistent Tight-Binding Quantum Chemistry Method for Large Molecules. ChemRxiv. Preprint. https://doi.org/10.26434/chemrxiv.8326202.v1, 2019.

[90] S. Grimme. xtb doc Release 6.2. 2019.

[91] A. McLean and G. Chandler. Contracted Gaussian basis sets for molecular calculations. I. Second row atoms, Z= 11–18. *The Journal of Chemical Physics*, 72(10):5639–5648, 1980.

[92] R. Krishnan, J. S. Binkley, R. Seeger, and J. A. Pople. Self-consistent molecular orbital methods. XX. A basis set for correlated wave functions. *The Journal of chemical physics*, 72(1):650–654, 1980.

[93] E. Glendening, J. Badenhoop, A. Reed, J. Carpenter, J. Bohmann, C. Morales, C. Landis, and F. Weinhold. Natural bond orbital analysis program: NBO 6.0. *Theoretical Chemistry Institute, University of Wisconsin, Madison, WI*, 2013.

[94] J. W. Ochterski. Thermochemistry in gaussian. *Gaussian Inc*, 1:19, 2000.

[95] F. Neese and F. Wennmohs. ORCA manual version 4.0.1. 2018.

[96] S. Kossmann and F. Neese. Comparison of two efficient approximate Hartee–Fock approaches. *Chemical Physics Letters*, 481(4-6):240–243, 2009.

[97] R. Izsák, A. Hansen, and F. Neese. The resolution of identity and chain of spheres approximations for the LPNO-CCSD singles Fock term. *Molecular Physics*, 110(19-20):2413–2417, 2012.

List of Abbreviations

3–21G	The split valence double zeta gaussina basis set
6–311G	The single zeta for core orbitals and triple zeta for valence orbitals gaussian basis set
6–311G**	The *6–311G* basis set with Polarization functions, equivalent to *6–311G(d,p)*
6–311G++	The *6–311G* basis set with Diffuse functions
AO	Atomic orbital
B3LYP	Hybrid functional using B (Becke (1988)) exchange and LYP (Lee, Yang, Parr) correlation functionals
BLYP	B (Becke (1988)) exchange and LYP (Lee, Yang, Parr) correlation functionals
CC	Coupled cluster
CCSD	Coupled cluster with single and double substitution operators
CCSD(T)	CCSD with perturbative estimate for connected triples
CCSDT	Coupled cluster with single, double, and triple substitution operators
COSMO	Conductor-like screening model
Def2QZV	Quadruple zeta valence Karlsruhe basis set
Def2SV	Split valence Karlsruhe basis set
Def2SVP	Split valence Karlsruhe basis set with Polarization functions
Def2TZV	Triple zeta valence Karlsruhe basis set
Def2TZVP	Triple zeta valence Karlsruhe basis set with Polarization functions
DFT	Density functional theory
DGA	Diglicolamide
DLPNO	Domain based local pair natural orbital
DMDOHEMA	Dimethyl-dioctyl-hexaethoxy-malonamide molecule
DN	The double zeta numerical basis set
DNP	The DN basis set with Polarization functions
DNP+	The DNP basis set with Diffuse functions

ESP	Electrostatic potential
EXAm	Extraction of Americium separation process
FF	Fukui function
GD2	Two–parameter Grimme dispersion correction
GD3	Three–parameter Grimme dispersion correction
GD3BJ	Three–parameter Grimme dispersion correction with Becke–Johnson damping
GGA	Generalized–gradient approximation
H.–F.	Hartree–Fock
H.–K.	Hohenberg–Kohn
HOMO	Highest occupied molecular orbital
HPA	Hirsfeld population analysis
K.–S.	Kohn–Sham
LCAO	Linear combination of atomic orbitals
LDA	Local density approximation
LSDA	Local spin density approximation
LUMO	Lowest unoccupied molecular orbital
Me_2–TEDGA	2,2'-oxybis(N,N-diethylpropanamide) molecule
Me–TEDGA	2-(2-(diethylamino)-2-oxoethoxy)-N,N-diethylpropanamide molecule
MEP	Minimum energy path
MIN	Minimal numerical basis set containing one basis function for each atomic orbital
MO	Molecular orbital
MPA	Mulliken population analysis
NBO	Natural bond–orbital theory
NPA	Natural population analysis
PBE	Perdew, Burke, and Enzerhof functional
PCM	Polarizable continuum model
PES	Potential Energy Surface
PW91	Perdew, Wang (1991) correlation functional
PWC	Perdew, Wang correlation functional
RIJCOSX	RI–J for Coulomb integrals approxmation and COSX numerical integration for HF exchange approximation
SCF	Self–consistent
STO–nG	The minimal gaussian basis set containing one basis function created from n primitive Gaussian functions for each atomic orbital
TEDGA	2,2'-oxybis(N,N-diethylacetamide) molecule
TMDGA	2,2'-oxybis(N,N-dimethylacetamide) molecule

TNP	The triple zeta numerical basis set with Polarization functions
TODGA	2,2'-oxybis(N,N-dioctylacetamide) molecule
VWN	Vosko, Wilk, Nusair correlation functional

List of Figures

List of Tables

Appendices

Appendix A

Fukui functions and Fukui charges

A.1 Radical Fukui charges

atom	atom label	TMDGA	TEDGA	Me–TEDGA	Me_2–TEDGA
N	(1)	0.047	0.047	0.048	0.045
C	(2)	0.078	0.074	0.077	0.078
O	(3)	0.117	0.116	0.119	0.117
C	(4)	0.004	0.005	−0.009	−0.007
C	(5)	eq. (4)	eq. (4)	0.002	eq. (4)
O	(6)	0.010	0.005	0.010	0.019
H	R^1	0.044	0.044	0.042	0.019
H	R^2	eq. R^1	eq. R^1	–	–
H	R^3	eq. R^1	eq. R^1	eq. R^1	eq. R^1
H	R^4	eq. R^1	eq. R^1	eq. R^1	–
H	average of all H	0.033	0.024	0.023	0.022

Table A.1 Radical Fukui charges based on Mulliken population analysis without an acid model; (settings: $DMol^3$, DNP, B3LYP, GD2, COSMO), atom labels given in figure 2.3

atom	atom label	TMDGA	TEDGA	Me–TEDGA	Me_2–TEDGA
N	(1)	0.094	0.066	0.034	0.066
C	(2)	0.080	0.076	0.097	0.078
O	(3)	0.100	0.075	0.112	0.094
C	(4)	−0.014	−0.009	−0.029	−0.027
C	(5)	eq. (4)	eq. (4)	−0.007	eq. (4)
O	(6)	0.019	0.015	0.012	0.017
H	R^1	0.042	0.040	0.039	0.027
H	R^2	eq. R^1	eq. R^1	–	–
H	R^3	eq. R^1	eq. R^1	eq. R^1	eq. R^1
H	R^4	eq. R^1	eq. R^1	eq. R^1	–
H	average of all H	0.035	0.026	0.023	0.020

Table A.2 Radical Fukui charges based on Mulliken population analysis with the H^+ acid model; (settings: $DMol^3$, DNP, B3LYP, GD2, COSMO), atom labels given in figure 2.3

atom	atom label	TMDGA	TEDGA	Me–TEDGA	Me_2–TEDGA
N	(1)	0.049	0.050	0.050	0.052
C	(2)	0.091	0.090	0.088	0.079
O	(3)	0.080	0.079	0.082	0.090
C	(4)	−0.016	−0.013	−0.004	0.009
C	(5)	eq. (4)	eq. (4)	−0.011	eq. (4)
O	(6)	0.028	0.024	0.019	0.014
H	R^1	0.051	0.050	0.034	0.029
H	R^2	eq. R^1	eq. R^1	–	–
H	R^3	eq. R^1	eq. R^1	eq. R^1	eq. R^1
H	R^4	eq. R^1	eq. R^1	eq. R^1	–
H	average of all H	0.031	0.023	0.021	0.020

Table A.3 Radical Fukui charges based on Mulliken population analysis with the H_3O^+ acid model; (settings: $DMol^3$, DNP, B3LYP, GD2, COSMO), atom labels given in figure 2.3

atom	atom label	TMDGA	TEDGA	Me–TEDGA	Me_2–TEDGA
N	(1)	0.032	0.044	0.044	0.041
C	(2)	0.018	0.014	0.012	0.012
O	(3)	0.071	0.063	0.063	0.065
C	(4)	−0.010	−0.002	−0.009	−0.011
C	(5)	eq. (4)	eq. (4)	0.000	eq. (4)
O	(6)	0.023	0.007	0.008	0.017
H	R^1	0.020	0.010	0.007	0.006
H	R^2	eq. R^1	eq. R^1	–	–
H	R^3	eq. R^1	eq. R^1	eq. R^1	eq. R^1
H	R^4	eq. R^1	eq. R^1	eq. R^1	–
H	average of all H	0.018	0.014	0.013	0.013

Table A.4 Radical Fukui charges based on Mulliken population analysis with the HNO_3 acid model; (settings: $DMol^3$, DNP, B3LYP, GD2, COSMO), atom labels given in figure 2.3

A.2 Electrophilic Fukui charges

atom	atom label	TMDGA	TEDGA	Me–TEDGA	Me_2–TEDGA
N	(1)	0.075	0.082	0.075	0.072
C	(2)	0.032	0.019	0.029	0.026
O	(3)	0.134	0.129	0.134	0.129
C	(4)	−0.002	−0.019	−0.017	−0.019
C	(5)	eq. (4)	eq. (4)	−0.017	eq. (4)
O	(6)	0.028	0.028	0.030	0.049
H	R^1	0.030	0.035	0.022	0.035
H	R^2	eq. R^1	eq. R^1	–	–
H	R^3	eq. R^1	eq. R^1	eq. R^1	eq. R^1
H	R^4	eq. R^1	eq. R^1	eq. R^1	–
H	average of all H	0.034	0.025	0.023	0.022

Table A.5 Electrophilic Fukui charges based on Mulliken population analysis without an acid model; (settings: $DMol^3$, DNP, B3LYP, GD2, COSMO), atom labels given in figure 2.3

atom	atom label	TMDGA	TEDGA	Me–TEDGA	Me_2–TEDGA
N	(1)	0.082	0.088	0.078	0.088
C	(2)	0.041	0.025	0.038	0.017
O	(3)	0.123	0.099	0.090	0.123
C	(4)	−0.008	−0.009	−0.010	−0.017
C	(5)	eq. (4)	eq. (4)	−0.001	eq. (4)
O	(6)	0.013	0.014	0.008	0.012
H	R^1	0.031	0.028	0.027	0.019
H	R^2	eq. R^1	eq. R^1	–	–
H	R^3	eq. R^1	eq. R^1	eq. R^1	eq. R^1
H	R^4	eq. R^1	eq. R^1	eq. R^1	–
H	average of all H	0.032	0.027	0.024	0.023

Table A.6 Electrophilic Fukui charges based on Mulliken population analysis with the H^+ acid model; (settings: $DMol^3$, DNP, B3LYP, GD2, COSMO), atom labels given in figure 2.3

atom	atom label	TMDGA	TEDGA	Me–TEDGA	Me_2–TEDGA
N	(1)	0.071	0.076	0.077	0.073
C	(2)	0.034	0.036	0.032	0.028
O	(3)	0.084	0.083	0.088	0.088
C	(4)	−0.014	−0.010	−0.012	−0.014
C	(5)	eq. (4)	eq. (4)	−0.010	eq. (4)
O	(6)	0.060	0.051	0.034	0.016
H	R^1	0.038	0.040	0.036	0.027
H	R^2	eq. R^1	eq. R^1	–	–
H	R^3	eq. R^1	eq. R^1	eq. R^1	eq. R^1
H	R^4	eq. R^1	eq. R^1	eq. R^1	–
H	average of all H	0.029	0.024	0.023	0.020

Table A.7 Electrophilic Fukui charges based on Mulliken population analysis with the H_3O^+ acid model; (settings: $DMol^3$, DNP, B3LYP, GD2, COSMO), atom labels given in figure 2.3

atom	atom label	TMDGA	TEDGA	Me–TEDGA	Me_2–TEDGA
N	(1)	0.044	0.088	0.090	0.084
C	(2)	0.033	0.026	0.020	0.019
O	(3)	0.096	0.121	0.120	0.119
C	(4)	−0.020	−0.006	−0.015	−0.022
C	(5)	eq. (4)	eq. (4)	−0.017	eq. (4)
O	(6)	0.047	0.007	0.019	0.024
H	R^1	0.036	0.021	0.016	0.033
H	R^2	eq. R^1	eq. R^1	–	–
H	R^3	eq. R^1	eq. R^1	eq. R^1	eq. R^1
H	R^4	eq. R^1	eq. R^1	eq. R^1	–
H	average of all H	0.031	0.025	0.023	0.023

Table A.8 Electrophilic Fukui charges based on Mulliken population analysis with the HNO_3 acid model; (settings: $DMol^3$, DNP, B3LYP, GD2, COSMO), atom labels given in figure 2.3

Appendix B

Partial charges

B.1 Mulliken partial charges

atom	atom label	TMDGA	TEDGA	Me–TEDGA	Me_2–TEDGA
N	(1)	−0.421	−0.424	−0.427	−0.425
C	(2)	0.458	0.466	0.473	0.500
O	(3)	−0.616	−0.615	−0.615	−0.618
C	(4)	0.052	0.050	0.048	0.054
C	(5)	eq. (4)	eq. (4)	0.068	eq. (4)
O	(6)	−0.569	−0.573	−0.567	−0.570

Table B.1 Partial charges based on the Mulliken population analysis without an acid model; (settings: $DMol^3$, DNP, B3LYP, GD2, COSMO), atom labels given in figure 2.3

atom	atom label	TMDGA	TEDGA	Me–TEDGA	Me_2–TEDGA
N	(1)	−0.392	−0.379	−0.479	−0.376
C	(2)	0.468	0.470	0.503	0.483
O	(3)	−0.518	−0.519	−0.522	−0.515
C	(4)	0.053	0.050	0.039	0.035
C	(5)	eq. (4)	eq. (4)	0.067	eq. (4)
O	(6)	0.030	−0.589	−0.574	−0.575

Table B.2 Partial charges based on the Mulliken population analysis with the H^+ acid model; (settings: $DMol^3$, DNP, B3LYP, GD2, COSMO), atom labels given in figure 2.3

atom	atom label	TMDGA	TEDGA	Me–TEDGA	Me_2–TEDGA
N	(1)	−0.399	−0.386	−0.385	−0.392
C	(2)	0.510	0.508	0.525	0.522
O	(3)	−0.668	−0.663	−0.663	−0.662
C	(4)	0.056	0.059	0.009	0.044
C	(5)	eq. (4)	eq. (4)	0.73	eq. (4)
O	(6)	−0.591	−0.594	−0.585	−0.570

Table B.3 Partial charges based on the Mulliken population analysis with the H_3O^+ acid model; (settings: $DMol^3$, DNP, B3LYP, GD2, COSMO), atom labels given in figure 2.3

atom	atom label	TMDGA	TEDGA	Me–TEDGA	Me_2–TEDGA
N	(1)	−0.415	−0.404	−0.406	−0.430
C	(2)	0.477	0.480	0.490	0.502
O	(3)	−0.624	−0.635	−0.638	−0.615
C	(4)	0.045	0.031	0.046	0.041
C	(5)	eq. (4)	eq. (4)	0.042	eq. (4)
O	(6)	−0.567	−0.566	−0.563	−0.565

Table B.4 Partial charges based on the Mulliken population analysis with the HNO_3 acid model; (settings: $DMol^3$, DNP, B3LYP, GD2, COSMO), atom labels given in figure 2.3

B.2 Hirshfeld partial charges

atom	atom label	TMDGA	TEDGA	Me–TEDGA	Me_2–TEDGA
N	(1)	−0.024	−0.029	−0.029	−0.031
C	(2)	0.161	0.164	0.161	0.163
O	(3)	−0.!383	−0..368	−0.374	−0.368
C	(4)	0.019	0.021	0.061	0.061
C	(5)	eq. (4)	eq. (4)	0.014	eq. (4)
O	(6)	−0.159	−0.150	−0.159	−0.158

Table B.5 Partial charges based on the Hirsfeld population analysis without an acid model; (settings: $DMol^3$, DNP, B3LYP, GD2, COSMO), atom labels given in figure 2.3

atom	atom label	TMDGA	TEDGA	Me–TEDGA	Me_2–TEDGA
N	(1)	0.005	−0.001	0.011	0.003
C	(2)	0.193	0.016	0.210	0.189
O	(3)	−0.196	−0.214	−0.230	−0.231
C	(4)	0.038	0.036	0.074	0.066
C	(5)	eq. (4)	eq. (4)	0.031	eq. (4)
O	(6)	0.031	−0.137	−0.137	−0.125

Table B.6 Partial charges based on the Hirsfeld population analysis with the H^+ acid model; (settings: $DMol^3$, DNP, B3LYP, GD2, COSMO), NBO, PCM), atom labels given in figure 2.3

atom	atom label	TMDGA	TEDGA	Me–TEDGA	Me_2–TEDGA
N	(1)	−0.003	−0.010	−0.008	−0.008
C	(2)	0.189	0.190	0.188	0.185
O	(3)	−0.252	−0.246	−0.246	−0.247
C	(4)	0.032	0.033	0.065	0.063
C	(5)	eq. (4)	eq. (4)	0.031	eq. (4)
O	(6)	−0.134	−0.133	−0.152	−0.146

Table B.7 Partial charges based on the Hirsfeld population analysis with the H_3O^+ acid model; (settings: DMol^3, DNP, B3LYP, GD2, COSMO), atom labels given in figure 2.3

atom	atom label	TMDGA	TEDGA	Me–TEDGA	Me_2–TEDGA
N	(1)	−0.010	−0.017	−0.018	−0.029
C	(2)	0.177	0.175	0.174	0.169
O	(3)	−0.307	−0.309	−0.305	−0.351
C	(4)	0.024	0.022	0.062	0.058
C	(5)	eq. (4)	eq. (4)	0.021	eq. (4)
O	(6)	−0.157	−0.143	−0.142	−0.142

Table B.8 Partial charges based on the Hirsfeld population analysis with the HNO_3 acid model; (settings: DMol^3, DNP, B3LYP, GD2, COSMO), atom labels given in figure 2.3

B.3 Partial charges fitted to electrostatic potencial

atom	atom label	TMDGA	TEDGA	Me–TEDGA	Me_2–TEDGA
N	(1)	0.157	−0.305	−0.308	−0.385
C	(2)	0.473	0.603	0.572	0.594
O	(3)	−0.654	−0.645	−0.659	−0.651
C	(4)	−0.161	−0.317	0.309	0.164
C	(5)	eq. (4)	eq. (4)	−0.333	eq. (4)
O	(6)	−0.348	−0.230	−0.330	−0.329

Table B.9 Partial charges based on the fitting to the Electrostatic potencial without an acid model; (settings: DMol^3, DNP, B3LYP, GD2, COSMO), atom labels given in figure 2.3

atom	atom label	TMDGA	TEDGA	Me–TEDGA	Me_2–TEDGA
N	(1)	0.112	−0.436	−0.319	−0.248
C	(2)	0.445	0.232	0.504	0.508
O	(3)	−0.265	−0.528	−0.477	−0.534
C	(4)	−0.085	−0.188	0.213	0.093
C	(5)	eq. (4)	eq. (4)	−0.175	eq. (4)
O	(6)	−0.212	−0.360	−0.373	−0.369

Table B.10 Partial charges based on the fitting to the Electrostatic potencial with the H^+ acid model; (settings: $DMol^3$, DNP, B3LYP, GD2, COSMO), atom labels given in figure 2.3

atom	atom label	TMDGA	TEDGA	Me–TEDGA	Me_2–TEDGA
N	(1)	0.061	−0.362	−0.334	−0.317
C	(2)	0.530	0.672	0.635	0.571
O	(3)	−0.586	−0.535	−0.593	−0.582
C	(4)	−0.232	−0.386	0.131	0.069
C	(5)	eq. (4)	eq. (4)	−0.127	eq. (4)
O	(6)	−0.192	−0.109	−0.433	−0.380

Table B.11 Partial charges based on the fitting to the Electrostatic potencial with the H_3O^+ acid model; (settings: $DMol^3$, DNP, B3LYP, GD2, COSMO), atom labels given in figure 2.3

atom	atom label	TMDGA	TEDGA	Me–TEDGA	Me_2–TEDGA
N	(1)	0.202	−0.333	−0.289	−0.300
C	(2)	0.468	0.601	0.537	0.539
O	(3)	−0.643	−0.621	−0.627	−0.628
C	(4)	−0.187	−0.270	0.343	0.274
C	(5)	eq. (4)	eq. (4)	−0.345	eq. (4)
O	(6)	−0.310	−0.264	−0.349	−0.263

Table B.12 Partial charges based on the fitting to the Electrostatic potencial with the HNO_3 acid model; (settings: $DMol^3$, DNP, B3LYP, GD2, COSMO), atom labels given in figure 2.3

Appendix C

Bond orders

C.1 Mulliken bond orders

bond	TMDGA	TEDGA	Me–TEDGA	Me_2–TEDGA
$N^{(1)}$–$C^{(2)}$	0.866	0.867	0.870	0.884
$C^{(2)}$–$O^{(3)}$	1.127	1.116	1.128	1.138
$C^{(2)}$–$C^{(4)}$	0.745	0.745	0.736	0.738
$C^{(4)}$–$O^{(6)}$	0.447	0.443	0.467	0.424
$C^{(5)}$–$O^{(6)}$	eq. $C^{(4)}$–$O^{(6)}$	eq. $C^{(4)}$–$O^{(6)}$	0.419	eq. $C^{(4)}$–$O^{(6)}$

Table C.1 Mulliken bond orders without an acid model; (settings: $DMol^3$, DNP, B3LYP, GD2, COSMO), atom labels given in figure 2.3

bond	TMDGA	TEDGA	Me–TEDGA	Me_2–TEDGA
$N^{(1)}$–$C^{(2)}$	0.917	0.934	0.709	0.944
$C^{(2)}$–$O^{(3)}$	0.959	0.942	1.122	0.948
$C^{(2)}$–$C^{(4)}$	0.729	0.729	0.729	0.726
$C^{(4)}$–$O^{(6)}$	0.411	0.450	0.455	0.418
$C^{(5)}$–$O^{(6)}$	eq. $C^{(4)}$–$O^{(6)}$	eq. $C^{(4)}$–$O^{(6)}$	0.427	eq. $C^{(4)}$–$O^{(6)}$

Table C.2 Mulliken bond orders with the H^+ acid model; (settings: $DMol^3$, DNP, B3LYP, GD2, COSMO), atom labels given in figure 2.3

bond	TMDGA	TEDGA	Me–TEDGA	Me_2–TEDGA
$N^{(1)}$–$C^{(2)}$	0.932	0.945	0.944	0.933
$C^{(2)}$–$O^{(3)}$	0.977	0.980	0.961	0.950
$C^{(2)}$–$C^{(4)}$	0.727	0.734	0.747	0.744
$C^{(4)}$–$O^{(6)}$	0.476	0.470	0.487	0.454
$C^{(5)}$–$O^{(6)}$	eq. $C^{(4)}$–$O^{(6)}$	eq. $C^{(4)}$–$O^{(6)}$	0.435	eq. $C^{(4)}$–$O^{(6)}$

Table C.3 Mulliken bond orders with the H_3O^+ acid model; (settings: $DMol^3$, DNP, B3LYP, GD2, COSMO), atom labels given in figure 2.3

bond	TMDGA	TEDGA	Me–TEDGA	Me_2–TEDGA
$N^{(1)}$–$C^{(2)}$	0.889	0.905	0.917	0.868
$C^{(2)}$–$O^{(3)}$	1.035	1.035	1.016	1.126
$C^{(2)}$–$C^{(4)}$	0.746	0.748	0.744	0.742
$C^{(4)}$–$O^{(6)}$	0.443	0.439	0.451	0.431
$C^{(5)}$–$O^{(6)}$	eq. $C^{(4)}$–$O^{(6)}$	eq. $C^{(4)}$–$O^{(6)}$	0.419	eq. $C^{(4)}$–$O^{(6)}$

Table C.4 Mulliken bond orders with the HNO_3 acid model; (settings: $DMol^3$, DNP, B3LYP, GD2, COSMO), atom labels given in figure 2.3

C.2 Mayer bond orders

bond	TMDGA	TEDGA	Me–TEDGA	Me_2–TEDGA
$N^{(1)}$–$C^{(2)}$	1.270	1.276	1.274	1.273
$C^{(2)}$–$O^{(3)}$	1.686	1.678	1.683	1.686
$C^{(2)}$–$C^{(4)}$	0.937	0.934	0.926	0.925
$C^{(4)}$–$O^{(6)}$	0.887	0.885	0.867	0.875
$C^{(5)}$–$O^{(6)}$	eq. $C^{(4)}$–$O^{(6)}$	eq. $C^{(4)}$–$O^{(6)}$	0.901	eq. $C^{(4)}$–$O^{(6)}$

Table C.5 Mayer bond orders without an acid model; (settings: $DMol^3$, DNP, B3LYP, GD2, COSMO), atom labels given in figure 2.3

bond	TMDGA	TEDGA	Me–TEDGA	Me_2–TEDGA
$N^{(1)}$–$C^{(2)}$	1.368	1.380	1.097	1.391
$C^{(2)}$–$O^{(3)}$	1.468	1.430	1.759	1.3446
$C^{(2)}$–$C^{(4)}$	0.944	0.943	0.932	0.933
$C^{(4)}$–$O^{(6)}$	0.864	0.885	0.865	0.873
$C^{(5)}$–$O^{(6)}$	eq. $C^{(4)}$–$O^{(6)}$	eq. $C^{(4)}$–$O^{(6)}$	0.904	eq. $C^{(4)}$–$O^{(6)}$

Table C.6 Mayer bond order with the H^+ acid model; (settings: $DMol^3$, DNP, B3LYP, GD2, COSMO), atom labels given in figure 2.3

bond	TMDGA	TEDGA	Me–TEDGA	Me_2–TEDGA
$N^{(1)}$–$C^{(2)}$	1.343	1.350	1.355	1.350
$C^{(2)}$–$O^{(3)}$	1.500	1.503	1.486	1.462
$C^{(2)}$–$C^{(4)}$	0.948	0.948	0.947	0.939
$C^{(4)}$–$O^{(6)}$	0.905	0.900	0.875	0.894
$C^{(5)}$–$O^{(6)}$	eq. $C^{(4)}$–$O^{(6)}$	eq. $C^{(4)}$–$O^{(6)}$	0.913	eq. $C^{(4)}$–$O^{(6)}$

Table C.7 Mayer bond order with the H_3O^+ acid model; (settings: $DMol^3$, DNP, B3LYP, GD2, COSMO), atom labels given in figure 2.3

bond	TMDGA	TEDGA	Me–TEDGA	Me_2–TEDGA
$N^{(1)}$–$C^{(2)}$	1.307	1.321	1.326	1.260
$C^{(2)}$–$O^{(3)}$	1.588	1.583	1.567	1.680
$C^{(2)}$–$C^{(4)}$	0.941	0.939	0.936	0.926
$C^{(4)}$–$O^{(6)}$	0.886	0.884	0.893	0.879
$C^{(5)}$–$O^{(6)}$	eq. $C^{(4)}$–$O^{(6)}$	eq. $C^{(4)}$–$O^{(6)}$	0.871	eq. $C^{(4)}$–$O^{(6)}$

Table C.8 Mayer bond order with the HNO_3 acid model; (settings: $DMol^3$, DNP, B3LYP, GD2, COSMO), atom labels given in figure 2.3

Appendix D

Electrostatic potencials

D.1 Without a acid model

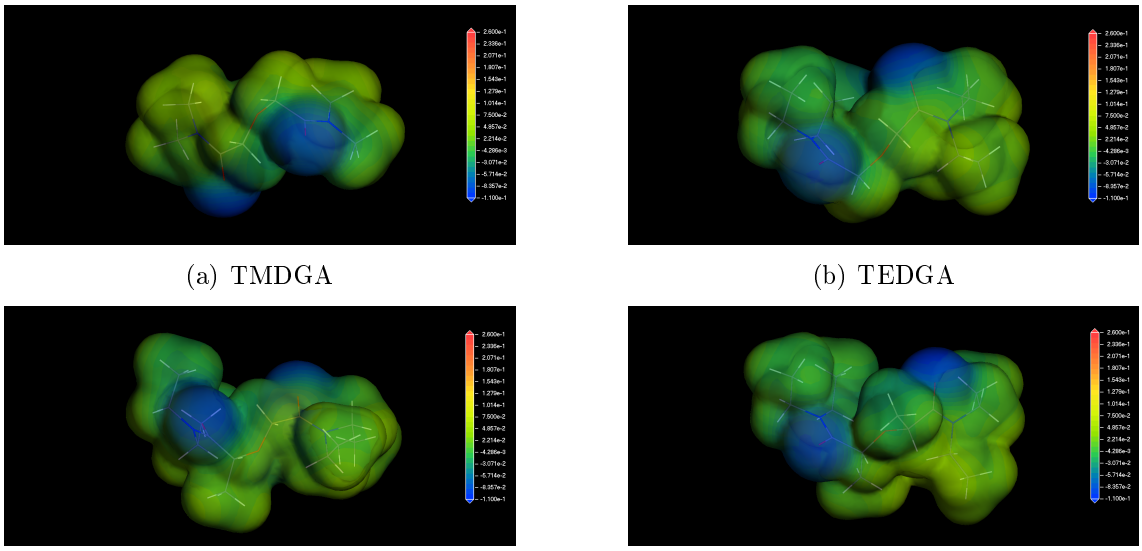

(a) TMDGA

(b) TEDGA

(c) Me–TEDGA

(d) Me_2–TEDGA

Figure D.1 Electrostatic potencials mapped on an isosurface of the electron density with value 0.017 e·Å^{-3} without acid model of (a) TMDGA, (b) TEDGA, (c) Me–TEDGAa (d) Me_2–TEDGA; (settings: DMol^3, DNP, B3LYP, GD2, COSMO)

D.2 The H_3O^+ acid model

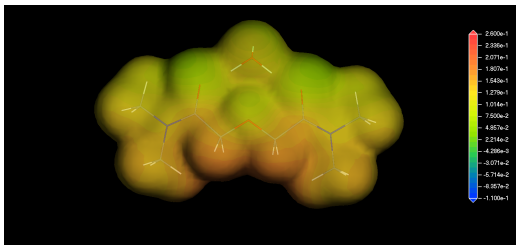

(a) TMDGA

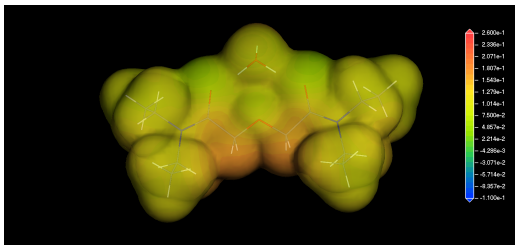

(b) TEDGA

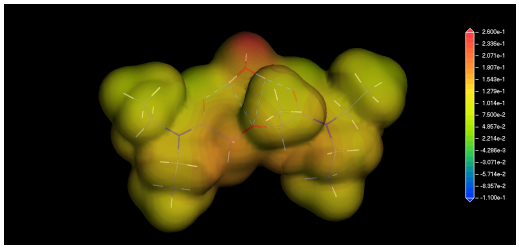

(c) Me–TEDGA

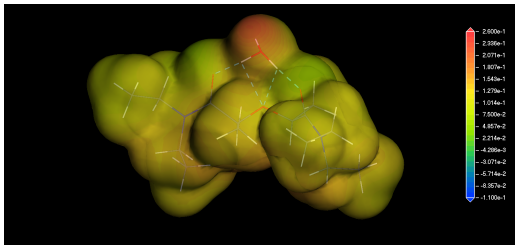

(d) Me_2–TEDGA

Figure D.2 Electrostatic potencials mapped on an isosurface of the electron density with value 0.017 e·Å^{-3} for H_3O^+ acid model of (a) TMDGA, (b) TEDGA, (c) Me–TEDGAa (d) Me_2–TEDGA; (settings: DMol^3, DNP, B3LYP, GD2, COSMO)

D.3 The HNO_3 acid model

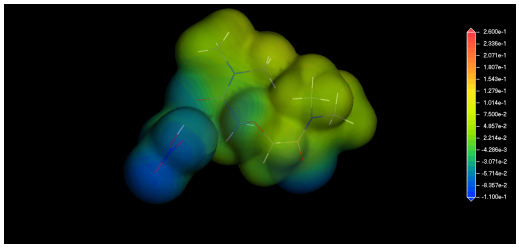

(a) TMDGA

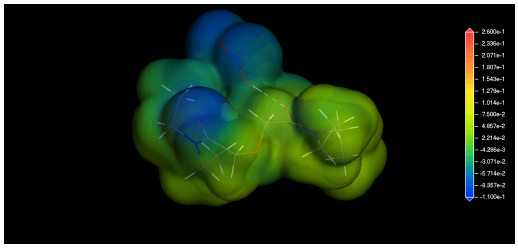

(b) TEDGA

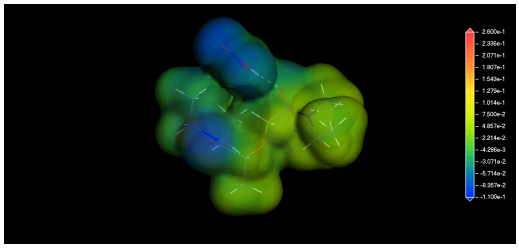

(c) Me–TEDGA

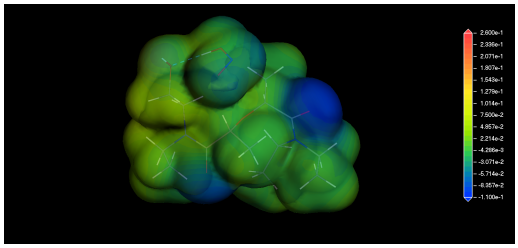

(d) Me_2–TEDGA

Figure D.3 Electrostatic potencials mapped on an isosurface of the electron density with value 0.017 e·Å^{-3} for H^+ acid model of (a) TMDGA, (b) TEDGA, (c) Me–TEDGAa (d) Me_2–TEDGA; (settings: DMol^3, DNP, B3LYP, GD2, COSMO)

Appendix E

Energy profiles of the reaction mechanism

E.1 Hydrogen abstraction by a hydroxyl radical

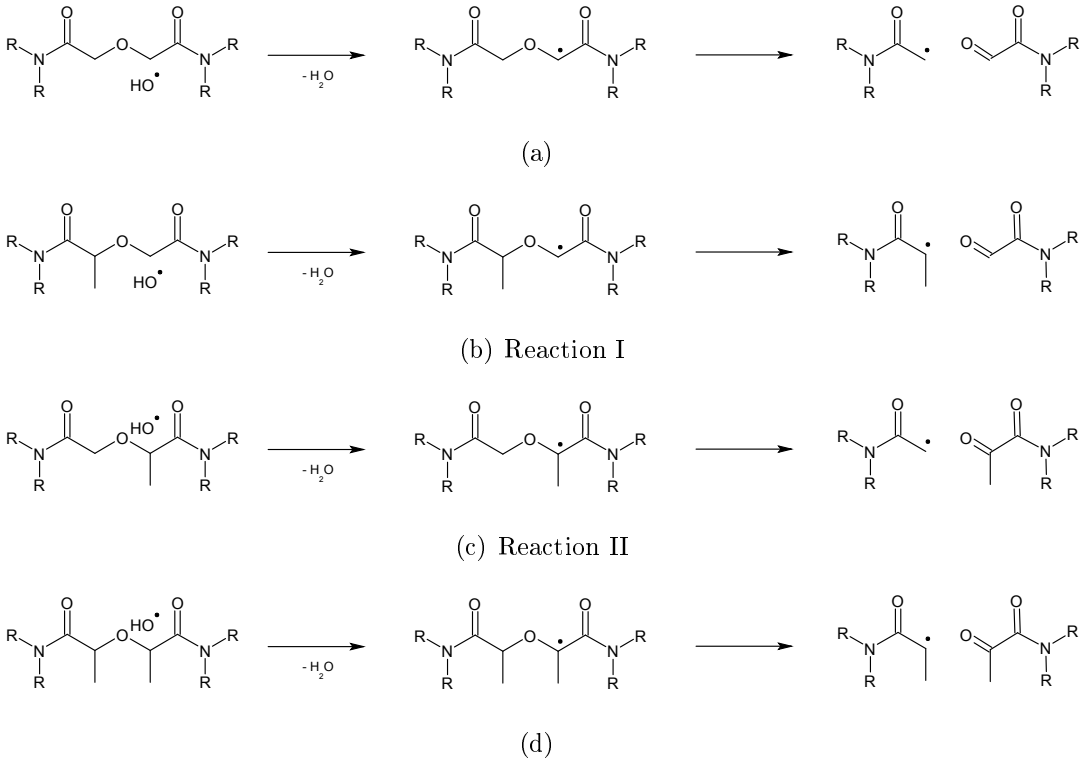

Figure E.1 Reactions scheme for considered degradation mechanism based on hydrogen abstraction by hydroxyl radical OH• (a) for TMDGA and TEDGA, (b) for Me–TEDGA leading to a rupture of the protected ether bond, (c) for Me–TEDGA causing a break of the unprotected ether bond and (d) for Me_2–TEDGA.

E.2 Hydrogen abstraction by a hydrogen radical using only DFT calculations

Reaction energy profile (kcal mol^{-1})					
molecule	R	TS 1	I	TS2	P
TMDGA	0	8.34	−21.86	−5.67	−27.11
TEDGA	0	5.10	−23.75	−4.78	−28.95
Me–TEDGA reaction I	0	8.21	−20.36	−7.17	−30.93
Me–TEDGA reaction II	0	6.28	−22.37	−5.55	−35.05
Me_2–TEDGA	0	7.18	−21.56	−6.40	−36.83

Table E.1 Reaction energy profile (kcal mol^{-1}) for the proposed degradation mechanism (figure 2.12) calculated with DFT and 6–311++G(2d,d,p) basis set, R stands for Reactants, TS1 for Transition state 1, I for intermediates, TS2 for Transition state 2 and P for Products

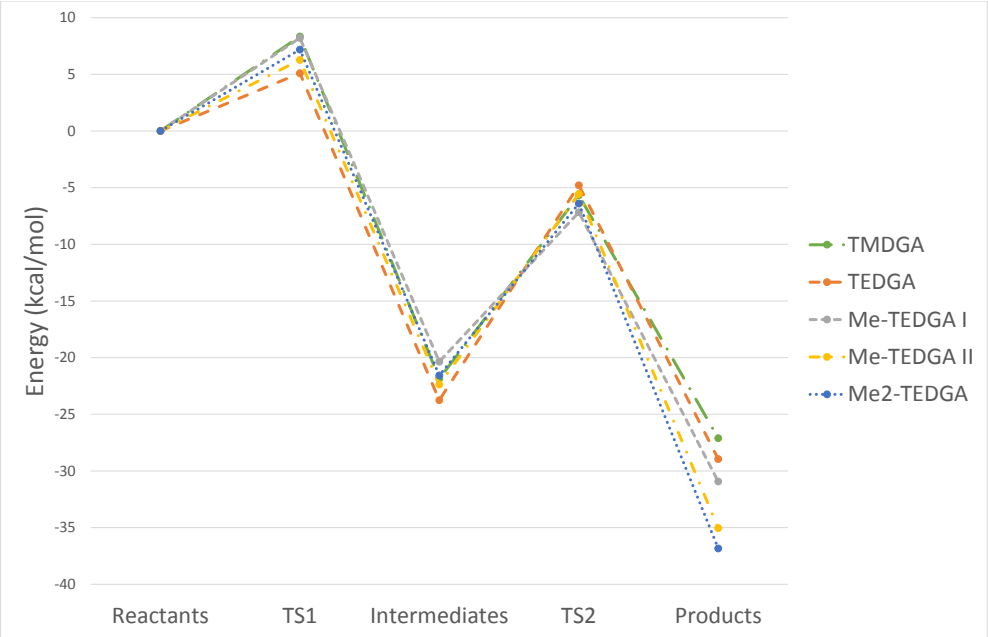

Figure E.2 Energy diagram for the proposed degradation mechanism calculated with DFT and 6–311++G(2d,d,p) basis set

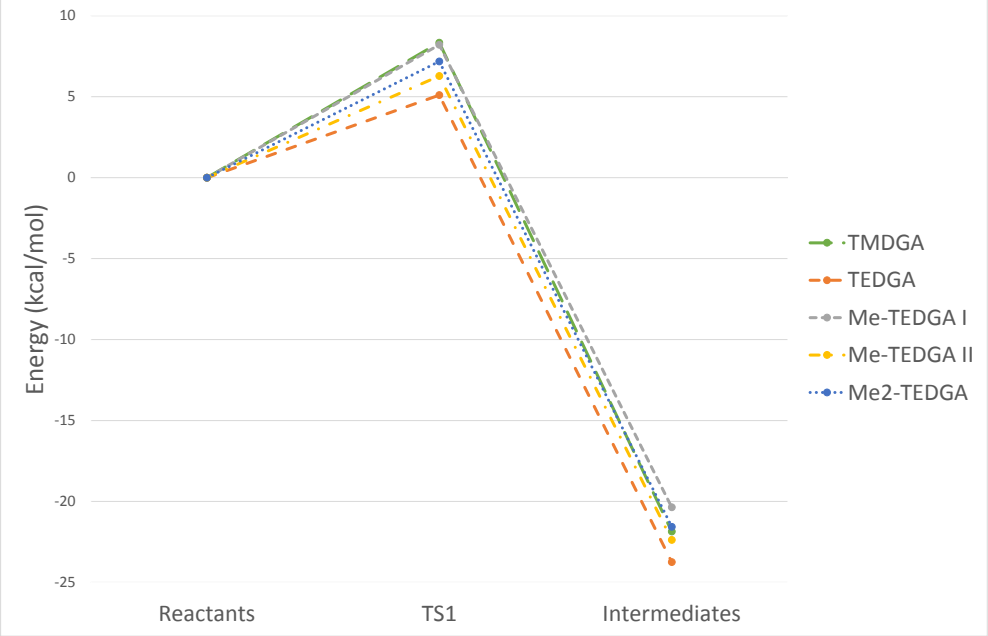

Figure E.3 Energy diagram of the first step of the degradation mechanism calculated with DFT and 6–311++G(2d,d,p) basis set

Reaction energy profile (kcal mol^{-1})					
molecule	R	TS 1	I	TS2	P
TMDGA	0	7.89	−22.51	−5.12	−27.37
TEDGA	0	6.68	−22.42	−4.61	−26.61
Me–TEDGA reaction I	0	6.08	−20.46	−6.94	−31.06
Me–TEDGA reaction II	0	5.63	−22.48	−5.52	−34.92
Me_2–TEDGA	0	7.51	−21.83	−6.21	−36.83

Table E.2 Reaction energy profile (kcal mol^{-1}) for the proposed degradation mechanism (figure 2.12) calculated with DFT and Def2TZVP basis set, R stands for Reactants, TS1 for Transition state 1, I for intermediates, TS2 for Transition state 2 and P for Products

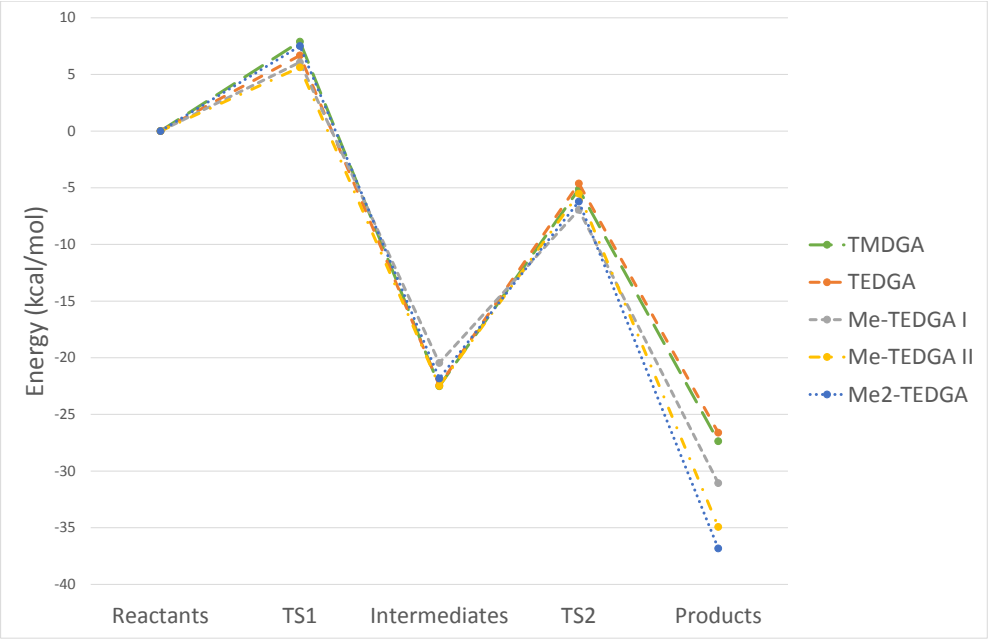

Figure E.4 Energy diagram for the proposed degradation mechanism calculated with DFT and Def2TZVP basis set

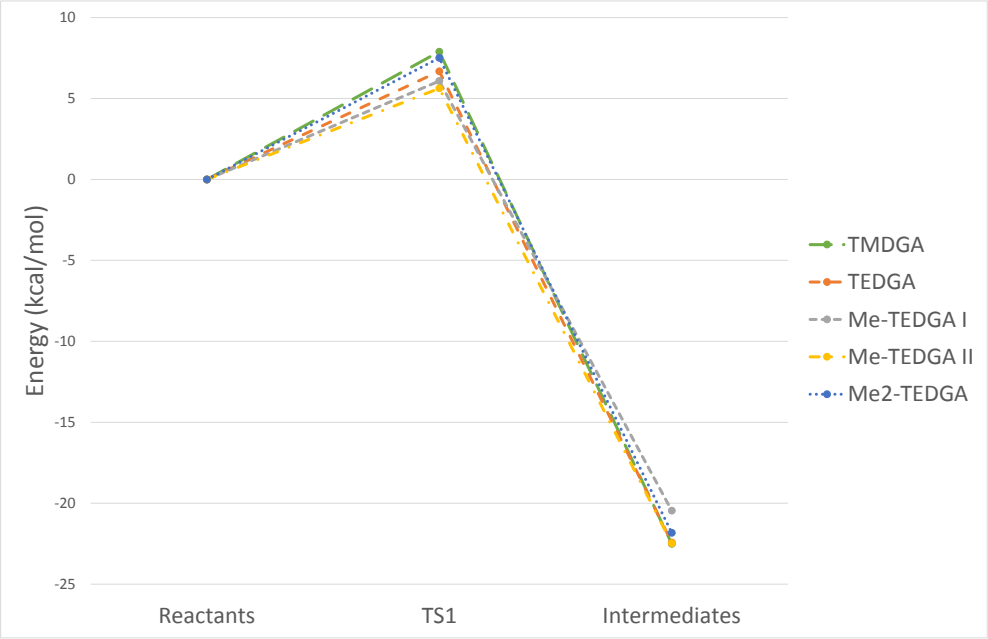

Figure E.5 Energy diagram of the first step of the degradation mechanism calculated with DFT and Def2TZVP basis set